

## ABSTRACT

Title of dissertation: OPTOELECTRONIC EXPERIMENTS ON  
RANDOM BIT GENERATORS AND  
COUPLED DYNAMICAL SYSTEMS

Caitlin Rose Sanford Williams  
Doctor of Philosophy, 2013

Dissertation directed by: Professor Rajarshi Roy  
Department of Physics

Optoelectronic systems have many important applications, and they have become ubiquitous in the contexts of communications and sensing. In recent years, optical and optoelectronic systems have been of interest for two newer purposes: generators of random bits and experimental dynamical systems used to understand chaos theory and synchronization.

Random bit generators are needed for secure communication, encryption, and Monte Carlo simulations. Algorithm-based pseudorandom number generators are susceptible to being hacked or producing incorrect numerical results in simulations, so physical noise-based sources of random numbers are needed. We have constructed a random bit generator based on amplified spontaneous emission (ASE), with generation rates of 12.5 Gbit/sec [1]. We develop an understanding of the mechanism behind generating random bits from ASE, and we demonstrate its suitability as a random number generator by standard statistical testing used to evaluate the random bits. This is the first use of ASE as a physical random number generator

(RNG).

Coupled dynamical systems are present in numerous contexts in the natural and man-made world. From neurons in the brain to coupled lasers to pedestrians on a bridge, it is important to understand how coupled dynamical systems or oscillators can synchronize in different ways. While many studies of coupled dynamical systems are conducted analytically and numerically, experimental studies are crucial for understanding how systems with real noise and features, which may not be accounted for in the models, actually synchronize. Experimental dynamical systems can display phenomena not previously studied or expected, guiding the development of more sophisticated models and the direction of analytical and numerical work, and experiments offer means for quickly exploring parameter space.

Sorrentino and Ott first proposed a theoretical formulation that described a counterintuitive phenomenon they referred to as *group synchrony* [2]. We show an experimental realization of group synchrony, in which the oscillators are grouped based on different parameters for each group [3]. Despite being coupled only to the oscillators in the dissimilar group, oscillators in the same group identically synchronize, through the mediation provided by the other group.

Unidirectional rings of oscillators have been studied in order to understand synchronization between coupled neurons, which can contribute to functions such as locomotion [4, 5]. We show an experimental realization of a uni-directional ring coupling configuration, with tunable coupling delays [6]. By changing the coupling delays, we show that it is possible to obtain different synchronization states. We compare experimental results to numerical simulations and calculations of the sta-

bility of the synchronous states.

We present an experiment of four delay-coupled optoelectronic oscillators as the first experimental observations of both of these novel synchronization phenomena in simple networks of coupled oscillators.

OPTOELECTRONIC EXPERIMENTS ON RANDOM BIT  
GENERATORS AND COUPLED DYNAMICAL SYSTEMS

by

Caitlin Rose Sanford Williams

Dissertation submitted to the Faculty of the Graduate School of the  
University of Maryland, College Park in partial fulfillment  
of the requirements for the degree of  
Doctor of Philosophy  
2013

Advisory Committee:  
Professor Rajarshi Roy, Chair/Advisor  
Professor Thomas E. Murphy, Co-Advisor  
Professor Michelle Girvan  
Dr. Louis M. Pecora  
Professor Brian R. Hunt

© Copyright by  
Caitlin Rose Sanford Williams  
2013

## Dedication

To my grandparents, Richard Sanford and Mary Williams, and to the memories of Rosalie Sanford and Maynard Williams. Their love of learning and commitment to education will shape generations after them.

## Acknowledgments

So many people have contributed substantially to my life and work over the past five years, and it is indeed a daunting and humbling task to thank everyone who has helped me reach this point in my career.

I am eternally grateful for two excellent advisors, Rajarshi Roy and Thomas Murphy. During my REU summer in their group as an undergraduate, continuing through many challenges and setbacks in graduate research and academics, and now at the final stages of my graduate work, they have consistently given me support, patience, and an abundance of wise guidance.

Lou Pecora has been a tremendous source of ideas and good feedback on my work, and I would like to thank him for serving on my dissertation committee. My thanks also go to Michelle Girvan and Brian Hunt for their interactions with me and for being part of my committee.

I cannot begin to describe my graduate career without giving credit to Adam Cohen and Bhargava Ravoori. Their many years of mentoring, friendship, and excellent scientific work have meant more to me than I can possibly put into words.

My research has been joined and enriched by many excellent collaborators and colleagues: Thomas Dahms, Ulrike Feudel, Xiaowen Li, Ed Ott, John Rodgers, Julia Salevan, Karl Schmitt, Eckehard Schöll, Ira Schwartz, Anurag Setty, Francesco Sorrentino, and Jordi Zamora-Munt. I am thankful to Hien Dao for four years of friendship and support during our time in research. Aaron Hagerstrom and Ryan Suess have also been excellent friends and companions in the lab. Alex Dragt was a

helpful mentor and supervisor during my first semester here at UMD. All of these people have contributed tremendously to my development as a scientist, and I deeply value the time I have spent with each of them.

The staff in IREAP and elsewhere at UMD has been invaluable to my time here. I am particularly grateful to Denise Abu-Laban, Nancy Boone, Dorothea Brosius, Ed Condon, Jane Hessing, Mohini Kaul, Don Martin, and Kathryn Tracey for their excellent assistance on many occasions.

The friendship and support of so many have been essential to my survival in grad school: Heather Bradshaw, Dan Campbell, Jessie Clough, Renee Campbell Gardner, Mark and Camille Herrera, Alexandra Kuvaeva, Kristy Gaff Johnson, John Platig, Cecilia Rorai, and Brock Russell. Kristen Burson and I have commiserated and rejoiced together countless times during our years as roommates, and her friendship has been a gift from God. The people of Church of the Resurrection have walked alongside me for many years and during many joys and struggles in grad school. The physics professors at Grove City College have never stopped investing in me, even after I finished my time there as a student. The UMD Women in Physics group has been a fun and helpful community during my time here. I could not have survived grad school without the support of all of these wonderful people!

The love and support of my parents and sister have sustained me through many difficult times. I simply cannot thank them enough for their faithfulness in my life and for their encouragement to follow the path I put myself on many years ago.

# Table of Contents

List of Figures	vii
List of Abbreviations	ix
1 Introduction	1
1.1 Nonlinear Dynamics and Chaos . . . . .	2
1.2 Synchronization . . . . .	3
1.3 Random Number Generation . . . . .	4
1.4 Outline of Thesis . . . . .	5
2 Random Bit Generator Based on Amplified Spontaneous Emission	7
2.1 Overview . . . . .	7
2.2 Theoretical Framework . . . . .	9
2.3 Experimental Set-up . . . . .	15
2.4 Noise Characterization . . . . .	16
2.5 Statistical Testing . . . . .	21
2.6 Improving Generation Rate with Analog-to-Digital Conversion . . . .	27
2.7 Conclusions . . . . .	28
3 Optoelectronic Feedback Loops	30
3.1 Overview . . . . .	30
3.2 Background . . . . .	31
3.3 A Single Feedback Loop . . . . .	34
3.3.1 Components . . . . .	34
3.3.2 DSP Implementation . . . . .	42
3.3.3 Equations of Motion . . . . .	44
3.3.3.1 Continuous Time . . . . .	44
3.3.3.2 Discrete Time . . . . .	46
3.3.4 Dynamics . . . . .	47
3.4 Coupled Feedback Loops . . . . .	47

4	Group and Cluster Synchrony in an Experiment of Four Delay-coupled Optoelectronic Feedback Loops	55
4.1	Overview . . . . .	55
4.2	Background . . . . .	56
4.3	Experimental Set-up . . . . .	57
4.4	Mathematical Model . . . . .	60
4.5	Stability of Group Synchrony . . . . .	62
4.6	Experimental Observations of Cluster Synchrony . . . . .	64
4.7	Experimental Observations of Group Synchrony . . . . .	68
4.8	Extension of Group Synchrony Results to Different Coupling Configurations . . . . .	75
4.9	Conclusions . . . . .	77
5	Varying Coupling Delay to Produce Different Synchronization States	79
5.1	Overview . . . . .	79
5.2	Introduction . . . . .	80
5.3	Experiment . . . . .	82
5.4	Stability Predictions . . . . .	86
5.5	Results and Discussion . . . . .	86
5.6	Conclusion . . . . .	91
6	Conclusions and Future Work	92
	Bibliography	96

## List of Figures

2.1	Simplified block diagram of a spectrally-filtered ASE noise source. . . . .	9
2.2	System used to generate random bits at 12.5 Gb/s. . . . .	13
2.3	Optical spectra of amplified spontaneous emission and filter. . . . .	14
2.4	Spectra of electrical noise. . . . .	17
2.5	Representative time traces and statistical histograms. . . . .	19
2.6	Normalized binary correlation as a function of lag. . . . .	21
2.7	Summary of test results obtained from the NIST statistical test suite. . . . .	24
2.8	Summary of test results obtained from the Diehard test suite. . . . .	25
3.1	Experimental set-up of a feedback loop. . . . .	35
3.2	Schematic and typical transmission curve of the MZM. . . . .	38
3.3	Circuit diagram of amplifier and bias circuit used to bias MZM. . . . .	39
3.4	Circuit diagram of photoreceiver circuit. . . . .	40
3.5	Printed circuit board containing bias and voltage amplifier circuits, along with photoreceiver circuits. . . . .	41
3.6	Block diagram of a single feedback loop. . . . .	45
3.7	Time traces for different dynamics. . . . .	48
3.8	Bifurcation diagram of a single feedback loop. . . . .	49
3.9	All-to-all network structure. . . . .	50
3.10	Block diagram for coupled feedback loops. . . . .	52
4.1	Experimental schematic for group synchrony. . . . .	58
4.2	Calculated stability of group synchrony. . . . .	63
4.3	Time traces for $\beta^{(A)} = \beta^{(B)} = 3.3$ , displaying identical synchrony. . . . .	66
4.4	Time traces for $\beta^{(A)} = \beta^{(B)} = 7.6$ , displaying cluster synchrony. . . . .	67
4.5	Time traces of group synchrony, comparing simulation with experiment . . . . .	70
4.6	Attractors and correlations for experimental data. . . . .	71
4.7	Time traces of group synchrony for different coupling configurations. . . . .	73
4.8	Simulation of a seven node network displaying group synchrony. . . . .	74
4.9	Cross- and auto-correlation functions of experimental data. . . . .	76
5.1	Schematic of four nodes connected in a unidirectional ring and exper- imental setup for a single node. . . . .	83

5.2	Representative time traces of different synchronization states. . . . .	85
5.3	Master Stability Function of different synchronization states as a function of coupling delay. . . . .	87
5.4	The phase relationships present as a function of coupling delay. . . . .	88
5.5	Multistability between synchronization states for long coupling delays.	89

## List of Abbreviations

ADC	Analog to Digital Converter
ASE	Amplified Spontaneous Emission
CW	Continuous Wave
DAC	Digital to Analog Converter
DFB	Distributed Feedback
DSP	Digital Signal Processing
IREAP	Institute for Research in Electronics and Applied Physics
MSF	Master Stability Function
MZM	Mach-Zehnder Modulator
NA	Network Analyzer
PC	Polarization Controller
PCB	Printed Circuit Board
PM	Polarization Maintaining
RNG	Random Number Generator
SM	Single Mode

## Chapter 1: Introduction

In recent decades, fiber optics have become extremely prevalent in industrial and research settings. Particularly notable is their use in communications, where optical fiber's lower loss and immunity to electromagnetic interference are significant advantages over electrical cabling for long-distance communication transmission. Additionally, optical systems have potential for significantly higher speeds than electronic systems, which is a tremendous advantage as technologies push for increasingly higher speeds of data transfer. In the laboratory, using fiber optics in the place of free-space optics removes much of the tedious work of aligning and re-aligning laser beams and lenses. In many cases, fiber-optic-based components and equipment can be purchased "off the shelf" and assembled quickly. Although some care must be taken not to bend fibers in a way that would attenuate the optical signal, it is generally simple to move individual components or an entire system without affecting the integrity of the experiment.

The experiments presented in this dissertation take advantage of the flexibility and ease of use of fiber optic based systems and optoelectronic systems that are partly constructed of optical components and partly of electronic components. The uses of these components and systems presented here are of two different va-

rieties. The first is for random number generation and the second is for study of synchronization in a small network of oscillators.

## 1.1 Nonlinear Dynamics and Chaos

In the 1960s, Edward Lorenz had developed a mathematical model for atmospheric air flow with what are simple equations. Despite the simplicity of the model, he discovered that running numerical simulations from slightly different values of initial conditions could lead to drastically different results [7]. This observation of the phenomenon that later became known as *chaos* beautifully illustrated an important feature of a chaotic system, that of sensitivity to initial conditions. In a chaotic system, the dynamics as time evolves are completely determined by a set of equations of motion, making it a deterministic system. Thus, if the equations and initial conditions are precisely known, the evolution of the system can be exactly predicted. However, in real systems, the initial conditions are subject to uncertainty. As the system evolves in time, what began as a slight difference in initial conditions in phase space will become a difference in the position in phase space that increases exponentially in time, until there is no correlation between the two points.

Chaos has been observed or studied in many natural and man-made systems, including economics [8], population dynamics [9], biology [10], fluid dynamics [11], lasers [12], chemical reactions [13]. Some applications of chaos include secure communication [14, 15], radar [16], and random number generation [17–21].

## 1.2 Synchronization

The phenomenon of synchronization between two coupled oscillators was observed by Christiaan Huygens in 1665, when he observed “an odd kind of sympathy” between two pendulum clocks hung on a common beam [22]. Huygens observed that the two pendulums oscillated with the same frequency, but in opposite directions from each other. These observations have been repeated experimentally and analyzed by Bennett, et al. in 2002, and they have presented a simple model of synchronization, which requires certain restrictions on the coupling between the oscillators, provided by the beam [23].

Even more interesting than synchronization between two periodic oscillators is synchronization between two chaotic oscillators, first studied in the 1980s [24–27]. Synchronization between two chaotic oscillators is not as intuitive as that between periodic oscillators because of the sensitivity to initial conditions that characterizes chaos, as described in sec. 1.1. However, despite this sensitivity to initial conditions, two or more chaotic oscillators can, in many cases, become synchronized so that their dynamics evolve exactly along the same trajectory in phase space.

There are many types of synchronization patterns that are possible. In *identical* or *amplitude synchrony*, the oscillators follow the exact same trajectory in phase space. If the oscillators always have exactly the same states at exactly the same time, then they display identical, *isochronal synchrony*. If two oscillators are *phase synchronized*, then their amplitudes are not identical, but their phases are correlated, which can be observed, for example, if the zero-crossings of a time series signal oc-

cur simultaneously. Two systems can also display *lag* or *time-delayed synchrony* if their dynamics are the same (either in amplitude or phase) but one is delayed with respect to the other. For example, time-delayed synchrony can arise when one oscillator is driven via unidirectional coupling by another, nominally identical oscillator, but there is some communication delay in the coupling between the oscillators [28].

In this dissertation, we examine synchronization patterns between multiple coupled oscillators. These oscillators can have chaotic or periodic dynamics, and display different synchronization patterns depending on the system parameters and coupling configuration. We study this synchronization using optoelectronic experimental systems that enable observations of these synchronization patterns in our laboratory.

### 1.3 Random Number Generation

Random numbers are needed for many applications, including encryption and Monte Carlo simulations. Pseudo-random number generators based on algorithms are sufficient for certain applications, but the need for cryptographically secure random numbers to be generated at high speeds has led to interest in physical means of generating random numbers [17–21, 29–32].

One interesting proposed application of chaotic dynamics is for high-speed random number generation. The broadband signals often generated from chaotic systems and the unpredictability of chaotic systems make them ideal candidates for random number generation. Several groups have reported experiments based on

chaotic optical systems that can generate bits at rates above Gb/sec [17–21]. In this dissertation, however, we will consider a method for generating random numbers based on optical noise from amplified spontaneous emission, rather than from a chaotic source.

## 1.4 Outline of Thesis

In Chap. 2, we will present a scheme for physically generating random bits based on amplified spontaneous emission. We will describe the theoretical framework and experimental set-up. We will report the statistical properties of the measured bits and show that this is a suitable method for generating random bits at high bit rates of 12.5 Gb/s.

In Chap. 3, we will describe the experimental configuration of an optoelectronic loop with time-delayed feedback. This system can generate a wide variety of dynamics. This system can also be well-modeled using time-delay differential equations or iterated maps, and we will derive the equations used to model this system.

In Chap. 4, a system of four coupled optoelectronic feedback loops, individually described in Chap. 3 and operated in the chaotic regime, is used to produce and study group synchrony. Two groups are formed, with each group consisting of two oscillators for the experiment. Each group may have different parameters, but in group synchrony, all of the oscillators in one group have identical equations of motion and parameters. In this case, there are no connections between members of

the same group, yet those oscillators will identically synchronize, without identically synchronizing with the other group. Cluster synchrony, a special case where all of the oscillators are identical, yet they still synchronize in two distinct groups, is also observed in the experiment. We show theoretical calculations predicting the stability of group synchrony and compare experimental results with theoretical calculations and numerical simulations.

In Chap. 5, we report an experiment of four optoelectronic oscillators delay-coupled unidirectionally in a ring. By varying the coupling delays, we observe different synchronization states, including isochronal synchrony, cluster synchrony, and splay-phase synchrony. By asymmetrizing the coupling delays, we can generate a variety of synchronization states.

Chapter 6 provides the conclusion to the thesis and suggestions for future work.

## Chapter 2: Random Bit Generator Based on Amplified Spontaneous Emission

*This chapter is based on work from the following publication: Fast Physical Random Number Generator Using Amplified Spontaneous Emission, C. R. S. Williams, J. C. Salevan, X. Li, R. Roy, and T. E. Murphy, Optics Express 18, 23584 (2010), ©2010 by OSA.*

### 2.1 Overview

Random number generators are important for a variety of applications, including encryption, secure key generation, gaming and Monte-Carlo calculations. Most of these applications employ pseudo-random number generators (PRNGs) – deterministic algorithms implemented on a computer or dedicated hardware that generate a seemingly unpredictable sequence of bits that are statistically indistinguishable from a truly random sequence. Although PRNGs are cost-effective and, in most cases, efficient, they suffer from the vulnerability that the future (and in some cases past) sequence can be deterministically computed if one discovers the seed or internal state of the algorithm. In weak PRNG algorithms, the internal state can be inferred by observing a sufficiently long history of the bit sequence. Even

in Monte-Carlo simulations, where security is unimportant, pseudorandom number generators can yield erroneous results [33].

For these reasons, there is growing interest in physical random number generators that produce random bits from inherently random or chaotic physical processes. Examples of physical processes used for random number generation include radioactive decay [34, 35], electrical thermal noise [29, 30], timing jitter in electrical oscillators [36–38], chaotic electrical circuits [39–41], and atmospheric RF noise [42]. In general, these systems are slow in comparison to pseudorandom number algorithms. Increasingly, optical or optoelectronic systems are being explored for random number generation. Shot noise has been exploited to produce random bits at rates up to 4 Mb/s, using photon-counting detectors with weak lasers or LEDs [31, 32]. Optical homodyne detection of vacuum fluctuations has been used to produce random bits at a 6.5 Mb/s [43]. Dark noise collected from CCDs has been used as a seed for pseudorandom number generators [44]. Phase noise produced in a distributed feedback laser has been used to generate random bits at rates up to 500 Mb/s [45, 46]. Recently, chaotic semiconductor lasers have been used to generate random bits at 1.7 Gb/s [17], or much faster when coupled with high-speed analog-to-digital conversion and digital post processing [18–21].

We report here a simple, scalable method of generating random bits using filtered amplified spontaneous emission (ASE) produced in a fiber amplifier. Spectrally-sliced ASE produces a fast, fluctuating signal that is much stronger than the background electronic noise, and can produce random bits at rates limited only by the bandwidths of the optical filter and electrical photoreceiver. Using only threshold

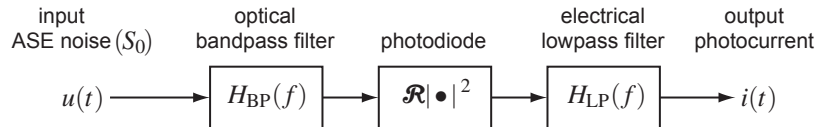


Figure 2.1: Simplified block diagram of a spectrally-filtered ASE noise source. The input optical signal  $u(t)$  is assumed to be white optical noise with spectral density  $S_0$ , which passes through a bandpass filter ( $H_{BP}$ ), square-law photodetector with responsivity  $\mathcal{R}$ , and lowpass filter ( $H_{LP}$ ) to produce an output photocurrent  $i(t)$ .

detection and XOR decorrelation techniques, we achieve 12.5 Gb/s random number generation, and confirm the quality of the resulting random bit sequence using accepted statistical tests developed for cryptographic security. The system uses only standard fiber optic components found in conventional digital telecommunication systems, and could be easily multiplexed into parallel wavelength channels by using WDM filter technology to spectrally slice the ASE spectrum.

## 2.2 Theoretical Framework

Amplified spontaneous emission is one of the most significant and ubiquitous noise sources in modern fiber optic telecommunication systems, and its statistical properties are well understood. In the present system, filtered amplified spontaneous emission noise is detected in a square-law photodetector, generating a noisy base-band electrical current that is referred to as “ASE-ASE beat noise.” We summarize here the key relations that govern the power spectrum, signal-to-noise ratio, and probability distribution of ASE-ASE beat noise, as these terms ultimately govern the speed and performance of our random bit generator.

Fig. 2.1 is a block diagram that defines the key elements used to produce the noise signal from which we generate random numbers. The input optical noise signal  $u(t)$  is taken to be white noise generated by amplified spontaneous emission with a power spectral density of  $S_0$ . We assume that the noise is polarized, both to simplify the analysis and also because that is how our experimental system is constructed. The noise passes through an optical bandpass filter that has a (dimensionless) complex transfer function  $H_{\text{BP}}(f)$ , so that the power spectral density of the emerging optical signal is  $S_0|H_{\text{BP}}(f)|^2$ . The photodiode produces an electrical current proportional to the squared magnitude of the optical field, and the resulting photocurrent is passed through a low-pass filter with transfer function  $H_{\text{LP}}(f)$ .

The photocurrent statistics depend on the characteristics of the bandpass and lowpass filters used. Therefore, in the equations that follow we provide both the general equation and also specific expressions for the case when both the bandpass and lowpass filters are Gaussian, i.e.,

$$|H_{\text{BP}}(f)|^2 = \exp\left[-(4 \ln 2) \frac{(f - f_0)^2}{B_{\text{BP}}^2}\right], \quad |H_{\text{LP}}(f)|^2 = \exp\left[-(\ln 2) \frac{f^2}{B_{\text{LP}}^2}\right] \quad (2.1)$$

where  $B_{\text{BP}}$  and  $B_{\text{LP}}$  represent the 3 dB bandwidths of the bandpass and lowpass filters, respectively.

The mean photocurrent generated by amplified spontaneous emission is proportional to the total integrated optical noise power,

$$\langle i \rangle = \mathcal{R} S_0 H_{\text{LP}}(0) \int |H_{\text{BP}}(f)|^2 df \quad (2.2a)$$

$$= \mathcal{R} S_0 B_{\text{BP}} \sqrt{\frac{\pi}{4 \ln 2}} \quad (\text{Gaussian}) \quad (2.2b)$$

where  $\mathcal{R}$  denotes the responsivity of the photodiode,  $H_{\text{LP}}(0)$  is the DC gain of lowpass filter<sup>1</sup>, and Eq. (2.2b) gives the specific result for the case of Gaussian filters.

The power spectral density of the photocurrent noise is given by [47, 48]

$$S_i(f) = \mathcal{R}^2 S_0^2 |H_{\text{LP}}(f)|^2 \int |H_{\text{BP}}(f') H_{\text{BP}}(f + f')|^2 df' \quad (2.3a)$$

$$= \mathcal{R}^2 S_0^2 B_{\text{BP}} \sqrt{\frac{\pi}{8 \ln 2}} \exp \left[ -(\ln 2) \left( \frac{1}{B_{\text{LP}}^2} + \frac{2}{B_{\text{BP}}^2} \right) f^2 \right] \quad (\text{Gaussian}) \quad (2.3b)$$

where, as before, Eq. (2.3a) gives the general expression and Eq. (2.3b) reflects the specific case when Gaussian filters are used. Note for the Gaussian filter case, the photocurrent noise spectrum will also be Gaussian, with a noise bandwidth of

$$B_{\text{noise}} = \left( \frac{1}{B_{\text{LP}}^2} + \frac{2}{B_{\text{BP}}^2} \right)^{-1/2} \quad (\text{Gaussian}) \quad (2.4)$$

The photocurrent variance can be directly calculated by integrating the noise spectrum<sup>2</sup>,

$$\sigma_i^2 = \int S_i(f) df = \mathcal{R}^2 S_0^2 \iint |H_{\text{LP}}(f) H_{\text{BP}}(f') H_{\text{BP}}(f + f')|^2 df df' \quad (2.5a)$$

$$= \mathcal{R}^2 S_0^2 B_{\text{BP}}^2 \left( \frac{\pi}{4 \ln 2} \right) \left( 1 + \frac{B_{\text{BP}}^2}{2B_{\text{LP}}^2} \right)^{-1/2} \quad (\text{Gaussian}) \quad (2.5b)$$

where again, the second equation reflects the specific case of Gaussian bandpass and lowpass filters.

---

<sup>1</sup>Because the responsivity  $\mathcal{R}$  is typically measured at DC frequencies, one typically takes  $H_{\text{LP}}(0) = 1$  with the assumption that any DC filter attenuation has been factored into  $\mathcal{R}$ .

<sup>2</sup>Note that for simplicity, we have omitted the DC photocurrent contribution to  $S_i(f)$ , which would appear as a term proportional to  $\langle i \rangle^2 \delta(f)$ . Thus, Eq. (2.3a) represents the power spectral density of the zero-mean process  $i(t) - \langle i \rangle$ .

The probability distribution of the photocurrent depends on the bandpass and lowpass filters used, and in general must be evaluated numerically [49]. However, in most practical cases of interest, the photocurrent probability distribution is well-approximated by a gamma distribution [50–52],

$$p_i(x) = x^{a-1} \frac{\exp(-x/b)}{b^a \Gamma(a)}, \quad x > 0 \quad (2.6)$$

where the dimensionless shape parameter  $a$  describes the signal to noise ratio [53],

$$a = \frac{\langle i \rangle^2}{\sigma_i^2} = \frac{H_{\text{LP}}^2(0) \left( \int |H_{\text{BP}}(f)|^2 df \right)^2}{\iint |H_{\text{LP}}(f) H_{\text{BP}}(f') H_{\text{BP}}(f + f')|^2 df df'} \quad (2.7a)$$

$$= \left( 1 + \frac{B_{\text{BP}}^2}{2B_{\text{LP}}^2} \right)^{1/2} \quad (\text{Gaussian}) \quad (2.7b)$$

One interesting property of ASE-ASE beat noise, apparent from Eq. (2.7b), is that the signal-to-noise ratio ( $a$ ) depends only on the bandwidths of the optical and electrical filters employed.

In a practical system, the mean photocurrent  $\langle i \rangle$  cannot be too large, or else the photoreceiver will saturate, producing only a DC output with no noise. This saturation will occur even if the output signal is AC-coupled. Therefore, in order to produce a strong electrical noise signal at the output without saturating the photoreceiver, one seeks to minimize the signal-to-noise ratio. From Eq. (2.7b), this can only be achieved by choosing bandpass and lowpass filters that have comparable bandwidths.

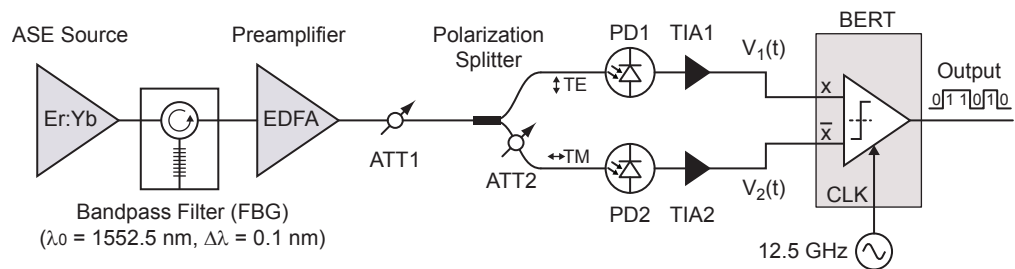


Figure 2.2: System used to generate random bits at 12.5 Gb/s. Amplified spontaneous emission (ASE) is generated in an Er/Yb-doped fiber that is continuously pumped by a 1 W, fiber-coupled 915 nm semiconductor laser diode. The resulting broadband ASE spectrum is bandpass-filtered using a 14.5 GHz (0.1 nm) fiber Bragg grating and optical circulator. The filtered noise is amplified in a conventional Er-doped fiber amplifier (EDFA). A fiber polarization splitter is used to produce two independent, identically distributed optical noise signals that are separately detected in a pair of matched 11 GHz photoreceivers, each comprised of a photodiode (PD) and transimpedance amplifier (TIA). A 12.5 Gb/s bit error rate tester (BERT) is used to perform a clocked comparison of the two received signals, producing a random string of bits. Two variable attenuators (ATT1, ATT2) are used to control the power of the noise signal, and compensate for loss mismatch between the two arms.

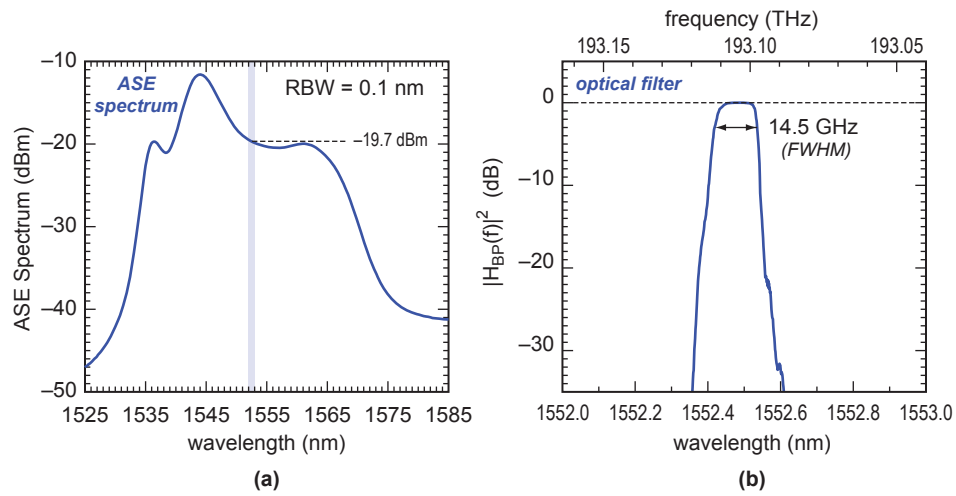


Figure 2.3: (a) Optical spectrum of the amplified spontaneous emission produced by the Er/Yb fiber amplifier, measured with a resolution bandwidth (RBW) of 0.1 nm. The shaded band indicates the approximate region where the subsequent optical bandpass filter is located. (b) Reflection spectrum of the fiber-Bragg grating filter, measured using a tunable laser, circulator and power meter. The full-width at half-max (FWHM) bandwidth of the filter was measured to be 14.5 GHz (approximately 0.1 nm.)

## 2.3 Experimental Set-up

Fig. 2.2 depicts the experimental system used to generate random bits. As the source of noise, we use a fiber amplifier (Optical Air Data Systems) consisting of a 1 W, 915 nm semiconductor pump laser and an erbium/ytterbium co-doped fiber. When there is no input, the amplifier generates broadband, incoherent, unpolarized optical noise through amplified spontaneous emission (ASE). The optical spectrum of the output of the amplifier was measured with an optical spectrum analyzer and is shown in Fig. 2.3a. The optical bandwidth of the ASE is much larger than the electrical bandwidth of even a fast detector. If the ASE were directly detected, Eq. (2.7b) dictates that in order to produce a sufficient noise variance one would require an impractically large DC photocurrent. To overcome this limitation, the broadband optical noise from the amplifier is filtered by an optical bandpass filter, comprised of a fiber Bragg grating (FBG) (TeraXion) and optical circulator. Fig. 2.3b plots the spectrum of the bandpass filter assembly, measured using a tunable laser and power meter. The filter has an optical bandwidth of 14.5 GHz (0.1 nm) and center wavelength of  $\lambda_0 = 1552.5$  nm. The resulting filtered noise signal is then amplified in a low-noise erbium-doped fiber amplifier (MPB EFA-R35W). A fiber polarization splitter divides the noise into two independent, identically distributed, orthogonally polarized noise signals that are separately detected in a pair of matched photoreceivers (Discovery DSC-R402). Each photoreceiver consists of a photodiode with responsivity of  $\mathcal{R} = 0.8$  A/W followed by a transimpedance amplifier with a gain of 500 V/A. The photoreceivers have an electrical bandwidth of 11

GHz, and the transimpedance amplifiers are AC coupled with a cut-on frequency of 30 kHz. Variable optical attenuators were used to adjust the total noise power, and also to balance the noise power in the two orthogonal polarization arms. Because amplified spontaneous emission is generated in both polarization states with equal intensity, we do not require precise polarization control or tracking in order to maintain an acceptable balance between the two arms of the system. The DC photocurrent in each photodiode was adjusted to be 0.77 mA.

To generate random bits, the two independent noise signals  $v_1(t)$  and  $v_2(t)$  were connected to the differential logic inputs ( $X$  and  $\bar{X}$ ) of a bit error rate tester (BERT). In this configuration, the BERT may be thought of as performing a clocked comparison of the two input signals, producing a logical one when  $v_1(t) > v_2(t)$  and a logical zero otherwise. An external 12.5 GHz clock signal supplied to the BERT determines the sampling frequency and bit generation rate. A DC bias voltage may be optionally added to either of the input signals, to control the comparison threshold.

## 2.4 Noise Characterization

Fig. 2.4 compares the computed and measured electrical spectra for one channel of the system. In Fig. 2.4a, we show the power spectrum of the ASE-ASE beat noise, obtained by numerically computing a self-correlation of the measured optical bandpass filter shape shown in Fig. 2.3b, i.e.,  $|H_{\text{BP}}(f)|^2 * |H_{\text{BP}}(-f)|^2$  [48]. Fig. 2.4b shows the measured spectral response of the photoreceiver, which acts as the lowpass

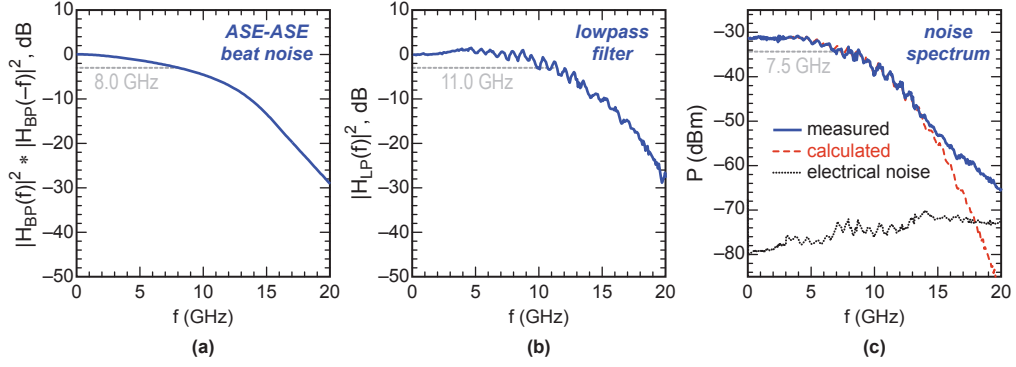


Figure 2.4: (a) Electrical spectrum of the ASE-ASE beat noise after square-law detection, estimated by performing a self-convolution of the optical bandpass filter spectrum shown in Fig. 2.3(b). The spectrum is normalized relative to its DC value. (b) Measured electrical speed of the photoreceiver and transimpedance amplifier, which form an equivalent lowpass filter. (c) Electrical spectrum obtained from one polarization channel, measured directly from one photoreceiver using a resolution bandwidth (RBW) of 3 MHz. The signal exhibits a broad, flat noise spectrum with a (single-sided) bandwidth of 7.5 GHz. The dashed red line shows the spectral shape obtained by multiplying and scaling the curves from (a) and (b). The dotted black line indicates the electrical noise obtained by extinguishing the optical signal. Over the frequency range of interest, the electrical noise remains negligible in comparison to the optical noise arising from ASE.

filter in our system,  $|H_{LP}(f)|^2$ . The photoreceiver spectral response was measured by exciting the detector with a 200 fs pulses from an 80 MHz mode-locked laser system, and measuring 80 MHz comb of spectral lines on an RF spectrum analyzer. The spectra shown in Figs. 2.4a-b are both normalized to a DC value of 0 dB. Finally, in Fig. 2.4c, we show the electrical spectrum of the ASE noise from one detector, measured with a resolution bandwidth of 3 MHz. For comparison, we also show the computed noise spectrum obtained by multiplying the two traces from (a) and (b), as described in Eq. (2.2a), which closely matches the measured spectrum. The computed spectrum was scaled in order to match the DC value observed in the measurement. The final noise spectrum has a bandwidth of 7.5 GHz, which agrees with the result calculated from Eq. (2.4) using  $B_{BP} = 14.5$  GHz and  $B_{LP} = 11$  GHz. The dotted black line in Fig. 2.4c shows the background electrical noise spectrum obtained by completely extinguishing the optical signal. Over the frequency range of interest, the electrical noise is more than 40 dB smaller than the optical noise produced by ASE.

Fig. 2.5 shows characteristic time traces from the two polarization channels in the system, acquired simultaneously on a 20 GHz bandwidth oscilloscope (Tektronix DPO72004B). Although the two signals have nearly identical amplitude distributions, there is no apparent correlation between them. We note that the cable and fiber lengths of the two channels were equalized to within 5 mm (or 25 ps.) The solid curve superposed on the measured voltage histogram shows the best-fit gamma distribution. When performing the fit, the gamma distribution was shifted to have a mean of zero, to account for the fact that the photoreceivers are AC-coupled.

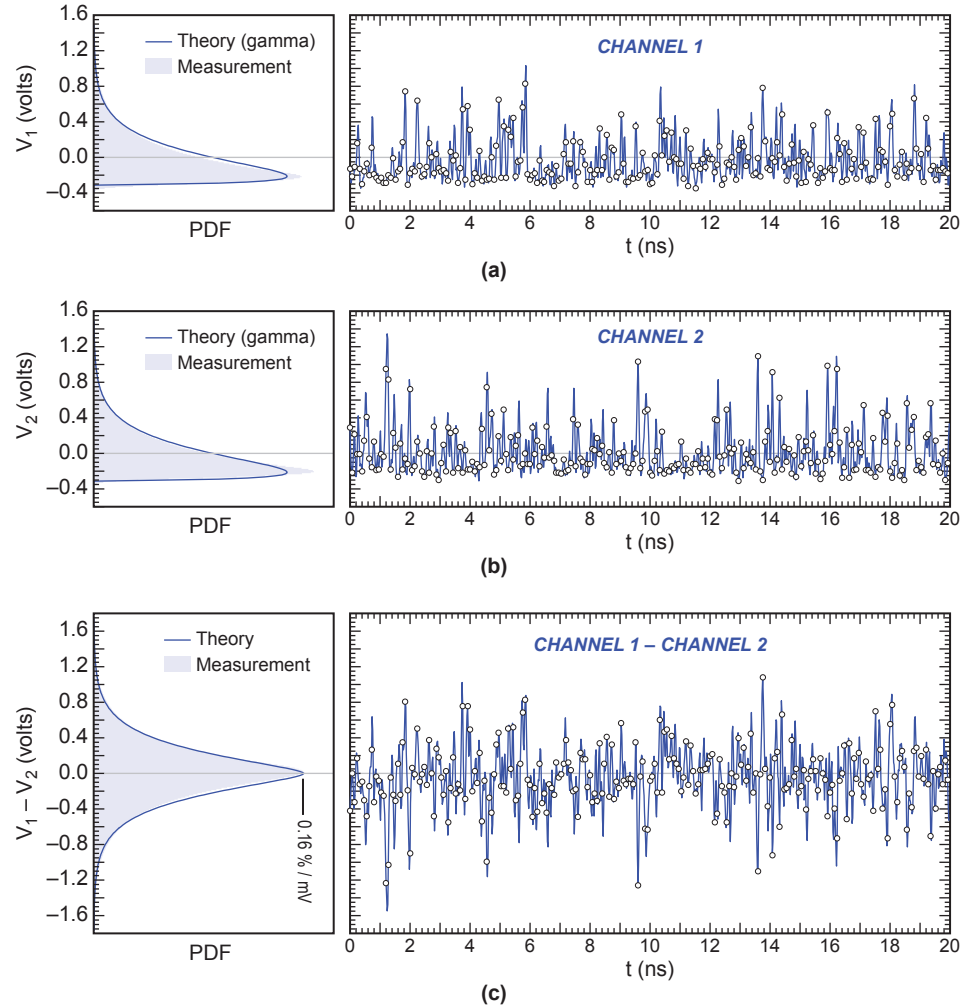


Figure 2.5: Representative time traces and statistical histograms measured on a 20 GHz, 50 GS/s digital oscilloscope. The symbols on the time traces indicate the times at which the waveform would be sampled to produce random bits. (a) Single-polarization channel (b) orthogonal polarization channel and (c) differential signal obtained by subtracting two. The theoretical noise distribution shown by the solid curves in (a) and (b) is a best-fit gamma distribution with shape parameter  $a = 1.44$  and scale parameter  $b = 0.21$  V. The theoretical distribution shown in (c) was calculated by assuming that the two subtracted signals are independent and have identical gamma distributions as obtained in (a) and (b).

The best-fit gamma distribution was obtained with  $a = 1.44$ , which is in reasonable agreement with the result of 1.37 predicted from Eq. (2.5b).

The two independent noise signals  $v_1(t)$  and  $v_2(t)$  are detected differentially by the bit error rate tester, which assigns a one or zero based on the difference signal  $v_1(t) - v_2(t)$ . Fig. 2.5c shows the calculated difference between the two channels and the corresponding statistical distribution of voltages. Unlike the single channels shown in Fig. 2.5a-b, the differential voltage has a symmetric distribution, with a mean and median of 0. The theoretical distribution was numerically calculated by performing a self-correlation of the gamma distribution shown in Figs. 2.5a-b. The balanced detection scheme is insensitive to common-mode interference and drift – even if the source power changes, the decision threshold does not need to be adjusted in order to produce an unbiased bit sequence. Although the fluctuations produced here are macroscopic and unpredictable, we note that for cryptographic applications the security of the resulting bit sequence assumes that a would-be adversary does not have access to the physical system or intermediate optical or electrical signals.

In addition to acquiring a binary sequence, the BERT reports a running average of the proportion of ones. Prior to acquiring the binary sequence, the variable attenuator (ATT2) was adjusted to set the mark ratio to  $0.5000 \pm 0.0001$ . The instrument is limited to a maximum acquisition length of 128 Mbit, which is not long enough to perform all of the statistical tests required for testing randomness. We therefore concatenated data from eight 128 Mbit records to produce a single  $10^9$  bit sequence used in subsequent statistical testing.

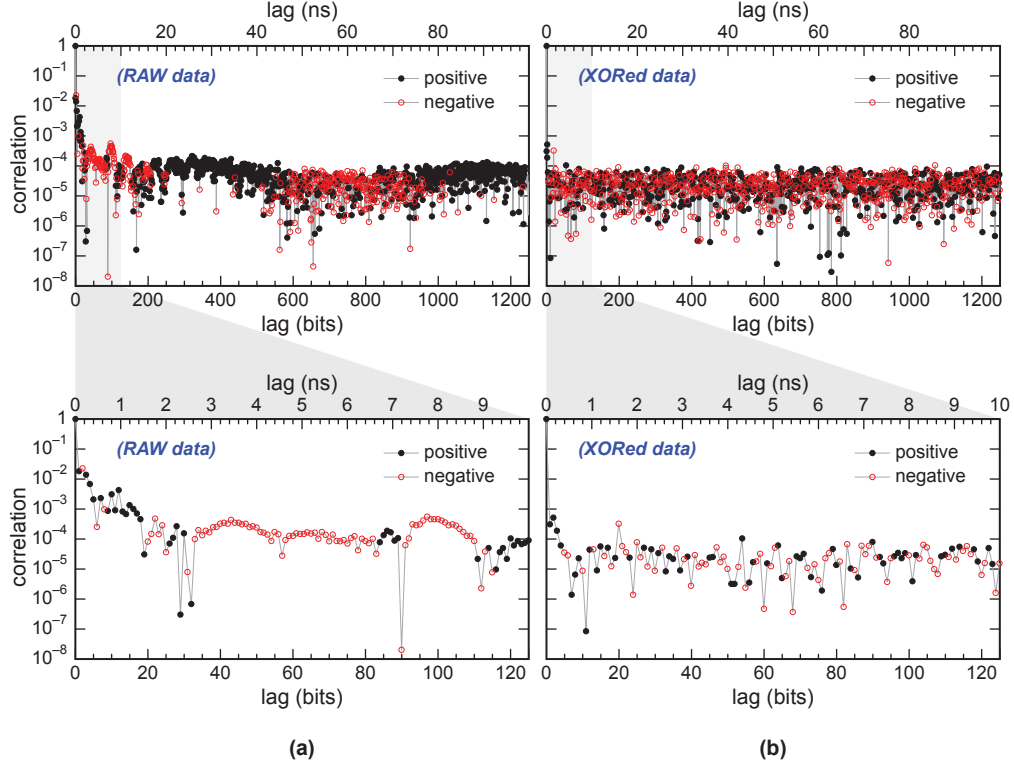


Figure 2.6: Normalized binary correlation as a function of lag (a) for the raw bit sequence produced by the experiment and (b) after computing the XOR with a 20-bit delayed copy of the signal. Positive correlation values are indicated with a filled symbol while negative correlations are indicated with open symbols. The correlation was calculated using a  $10^9$  bit record. For a truly random unbiased  $10^9$  bit record, one expects to obtain an average normalized correlation of 0 and a standard deviation of the correlation of  $3.16 \times 10^{-5}$  [54].

## 2.5 Statistical Testing

One of the simplest statistical measures of randomness is the degree of correlation between adjacent (or delayed) bits in the sequence. Fig. 2.6a plots the normalized correlation as a function of the bit delay  $k$  (or time delay  $\tau$ ) for a  $10^9$ -bit random sequence produced by our system. The normalized correlation at lag  $k$  was

calculated in the following way

$$\rho_k = \frac{\langle b[n]b[n+k] \rangle - \langle b[n] \rangle^2}{\langle b^2[n] \rangle - \langle b[n] \rangle^2} \quad (2.8)$$

where  $\langle \bullet \rangle$  denotes a statistical average<sup>3</sup> over the  $N$  bits of the binary sequence  $b[n]$ . The correlation  $\rho_k$  defined in Eq. (2.8) is a symmetric function of the lag  $k$ , with  $\rho_0 = 1$ . For a finite length sequence of  $N$  ideal, independent, unbiased bits, the correlation calculated by Eq. (2.8) has an expected value that decreases as  $(-1/N)$  and a standard deviation that decreases as  $1/\sqrt{N}$  [54]. For  $N = 10^9$ , we therefore expect the correlation for  $k \neq 0$  to be statistically centered about 0 with a standard deviation of  $3.16 \times 10^{-5}$ .

As shown in Fig. 2.6a, the raw data produced by our system exhibits a small, but statistically significant correlation, especially for small lags. There is also a small but clearly discernible ringing pattern in the correlation, which slowly alternates between positive and negative as a function of  $k$ , even for large lags. Without the XOR processing, the small but statistically significant correlation seen in Fig. 6a would cause the raw bit sequence to fail several of the statistical tests.

One simple and common way to decrease the correlations of a random bit-stream is to form a new sequence by taking the exclusive or (XOR) between independently acquired sequences [17, 30, 36, 45]. For two identically distributed sequences with a mark-ratio of  $p$  and correlation of  $\rho_k$ , the binary sequence obtained

---

<sup>3</sup>When computing the average  $\langle b[n]b[n+k] \rangle$ , the  $N$ -bit sequence  $b[n]$  is assumed to repeat with a period of  $N$ , e.g.,  $b[N+k] = b[k]$ .

by computing the XOR will have a mark ratio and correlation of

$$p' = 2p(1 - p), \quad \rho'_k = \rho_k(1 - p')(1 - 2p' + \rho_k p') \quad (2.9)$$

If the original sequences are unbiased, then the XOR process will produce an unbiased sequence with new correlation  $\rho'_k = \rho_k^2/4$ . In practice, we have found that the statistical properties can be improved by taking the XOR between the original sequence and a delayed copy of itself. Delays as small as 20 bits were found to be sufficient to produce a sequence that passes all of the statistical tests for randomness. Fig. 2.6b plots the normalized binary correlation for the XORed data sequence  $b[n] \oplus b[n - 20]$ . The resulting sequence exhibits a correlation near the statistical noise level, with no discernible pattern or trend. Although we computed the XOR using off-line postprocessing, it could easily be implemented in real-time using simple high-speed logic operations. The lagged XOR process does not require more than 20 bits of delay, and does not reduce the generation rate.

We also evaluated the statistical properties of the random process using the NIST statistical test suite for cryptographic random number generators [55]. The NIST test suite contains 15 types of statistical tests, some of which contain multiple sub-tests. Each test is applied to a 1 Mbit sequence and returns a “ $p$ -value” that, for a truly random bit sequence, would be uniformly distributed between 0 and 1. The NIST test suite applies each test to 1000 sequences (a total of  $10^9$  bits) and then computes a single composite  $p$ -value to assess whether the constituent  $p$ -values are uniformly distributed. For a truly random sequence, the composite  $p$ -value should also be uniformly distributed between 0 and 1. The composite  $p$ -values must all

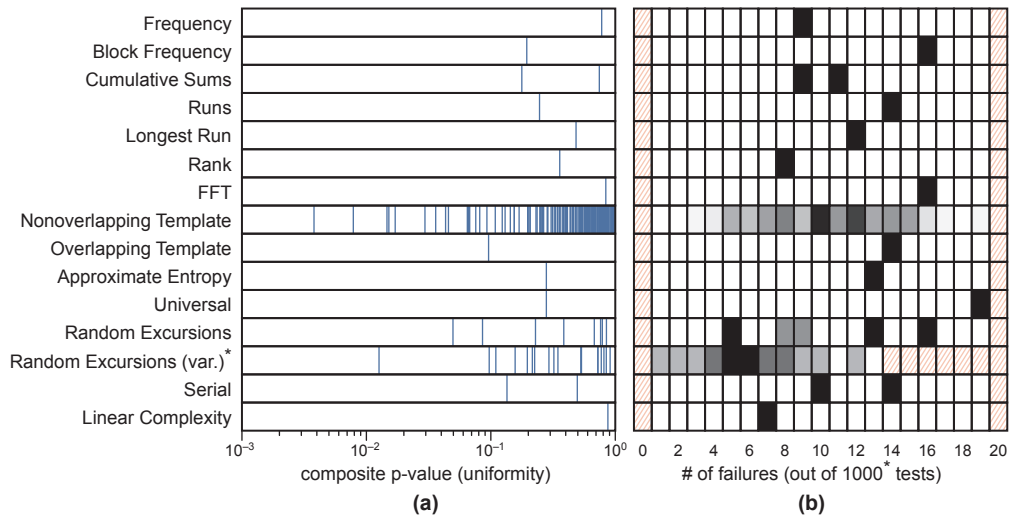


Figure 2.7: Summary of test results obtained from the NIST statistical test suite (STS-2.1) [55] applied to a  $10^9$  bit record obtained from the XORed data set. The NIST test suite comprises 15 types of tests, some of which return multiple results. (a) The composite  $p$ -values for each of the statistical tests and (b) the number of “failures” out of 1000 trials. For a truly random bit sequence, the  $p$ -values should be uniformly distributed on the interval  $[0,1]$ , and the number of failures should follow binomial distribution with  $N = 1000$  and  $\alpha = 0.01$ . For tests that return multiple results, all composite  $p$ -values are plotted in (a), and (b) shows a gray-scale histogram reflecting the number of failures out of 1000\*. The passing criteria are that all of the computed  $p$ -values must exceed 0.0001 and each test must yield between 1 and 19 failures out of 1000 trials. \*The random excursions variant test is applied to only 561 records, and may have no more than 13 failures.

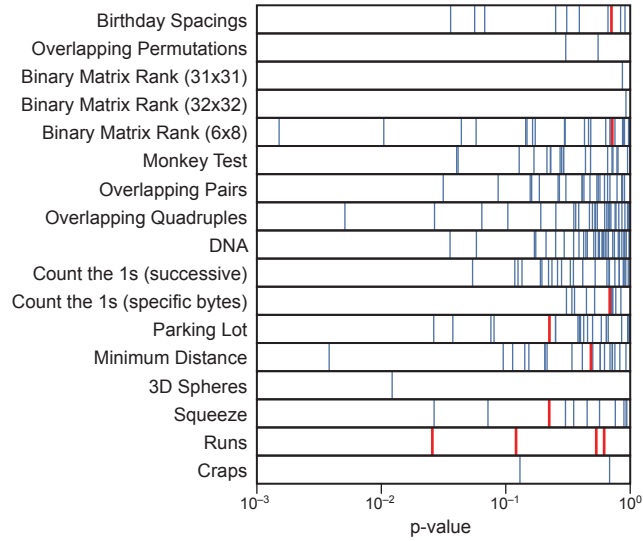


Figure 2.8: Summary of test results obtained from the Diehard test suite applied to a  $74 \times 10^6$  bit record obtained from the XORed data set. For tests that return multiple  $p$ -values, all are shown. For tests that compute a composite  $p$ -value by applying the Kolmogorov-Smirnov (K-S) test, the resulting  $p$ -value is indicated in red. In order to pass the tests, all  $p$ -values (or, where appropriate, the composite K-S  $p$ -value) must exceed 0.0001.

exceed  $10^{-4}$  in order to pass the NIST test. Furthermore, of the 1000 individual  $p$ -values obtained for each test, no fewer than 1 nor more than 19 may fall below the threshold of  $\alpha = 0.01$ . Fig. 2.7 plots the results of the NIST tests applied to the  $10^9$  bit XORed data sequence. For tests that produce multiple composite  $p$ -values, all are shown in Fig. 2.7a. The number of tests (out of 1000) with  $p < 0.01$  is plotted in Fig. 2.7b. For tests that produce multiple results, the numbers are shown as a grayscale histogram. The XORed data set passes all of the NIST statistical tests.

We also confirmed that the XORed data set passes all the tests in the Diehard statistical suite [56]. The Diehard suite comprises 17 different statistical tests, some of which require up to 74 Mbits of data. As with the NIST tests, each of the

tests returns a  $p$ -value that, for a random sequence, would be uniformly distributed between 0 and 1. For some tests, the Diehard suite computes a composite  $p$ -value using the Kolmogorov-Smirnov (K-S) test to assess the degree of uniformity. In Fig. 2.8 we plot the results of the Diehard tests.  $p$ -values obtained from the K-S test are indicated by thick red lines. Where available, the individual  $p$ -values from which the composite was calculated are shown by the thin blue lines. In order to pass each test, the computed  $p$ -values (or, where available, the K-S  $p$ -value) must all exceed  $10^{-4}$ .

It must be emphasized that while statistical testing has a role in evaluating random number generators, it should not be the sole qualifying criterion for all applications. The speed, simplicity, cost, long-term stability, and security are all features that cannot be assessed using standard statistical tests. Moreover existing statistical tests cannot distinguish between different physical sources of randomness. Depending on the specific needs of the application, new tests may be needed to judge the suitability of a given method of random number generation. At a fundamental level, Pironio et al. recently described an experimental approach to certifying the randomness of a measurement by testing Bell's inequality [57]. Apart from this, the goal of quantifying randomness using non-statistical, experimental measurements remains difficult.

## 2.6 Improving Generation Rate with Analog-to-Digital Conversion

A few groups have recently demonstrated extremely fast random bit generation using chaotic lasers and high-speed analog-to-digital converters (ADCs) [19–21]. Instead of applying a simple threshold comparison (as was done here), these systems utilize the output of an ADC in order to produce multiple bits per sample. In order to generate sequences that pass all of the requisite statistical tests, these methods all employ some form of digital processing that include discarding the most significant bits. The ultimate speed that can be achieved using such methods is not known, but will depend primarily on the cost and complexity of postprocessing that is deemed acceptable. As noted by others [21], it is unclear to what extent the high-speed chaotic optical signal contributes to the performance, in comparison to the intrinsic noise of the ADC converter, which can often dominate the least significant bits [58].

For the purpose of comparison, we investigated using a high-speed ADC with the spectrally-sliced ASE noise source reported here. The time traces shown in Fig. 2.5a-b were collected on a 20 GHz, 50 GS/s, 8-bit oscilloscope. Using the 8-bit signed integers  $x[n]$  (in two’s-complement format) taken from these records, we computed a 9-th order discrete derivative (using 32-bit, two’s-complement arithmetic), and retained only the 8 least significant bits of the resulting sequence [20]:

$$\begin{aligned}
 y[n] = & (x[n] - 9x[n - 1] + 36x[n - 2] - 84x[n - 3] + 126x[n - 4] - 126x[n - 5] \\
 & + 84x[n - 6] - 36x[n - 7] + 9x[n - 8] - x[n - 9]) \ \& \ 0x000000FF
 \end{aligned}
 \tag{2.10}$$

In this way, we produce a new sequence of unsigned 8-bit integers,  $y[n]$  at a rate

of 50 GHz, for a cumulative random generation rate of 400 Gb/s (or 800 Gb/s if one considers both orthogonal polarization channels.) The resulting sequence was confirmed to pass all of the standard NIST and Diehard tests for randomness. Next, we completely extinguished the optical signal and performed the same process using only the background electrical noise present in our system. The resulting sequence *also* passed all of the NIST and Diehard statistical tests.

This experiment suggests that a chaotic laser or other optical noise source is not an essential ingredient for such methods: other sufficiently random electrical input signals applied to an ADC (including the intrinsic electrical noise and sampling noise) can produce statistically random bits, when digital processing is employed. Using the postprocessed least significant bits from an ADC to generate random numbers is feasible, but more costly and less practical than the ASE-based system described here, which is comprised entirely of telecom-grade components commonly found in optical networks.

## 2.7 Conclusions

We demonstrated a 12.5 Gb/s random number generator based on threshold detection of filtered amplified spontaneous emission by a high-speed photoreceiver. The amplified spontaneous emission noise is shown to be significantly stronger than the electrical background noise, and the measured statistical distributions and noise spectra show a close agreement with theory. Unlike earlier reported optoelectronic random number generators that are limited in speed by photon counting electronics

or laser dynamics, this system is limited primarily by the speed of available photoreceivers. This random number generation method is therefore guaranteed to keep pace with ongoing advances in digital optical communication systems, as both rely on the same key optoelectronic components. The system uses telecom grade filters, fiber amplifiers, and detectors, and could easily be extended to multiple wavelength channels, each of which would generate independent random sequences in parallel. The resulting random bit sequence passes the most widely accepted statistical tests used to evaluate cryptographic random number generators.

## Chapter 3: Optoelectronic Feedback Loops

### 3.1 Overview

In this chapter, we will lay the foundation for the experiments detailed in Chapters 4 and 5. While Chapter 2 presented an experiment involving optical noise, Chapters 3-5 will focus on a different experiment, that of coupled optoelectronic feedback loops, which act individually as periodic or chaotic oscillators. This experimental system is used to study synchronization in small networks of oscillators. The particular experimental design described here involves commercially-available fiber optic and electronic components, which make these relatively inexpensive experiments simple to assemble. By using optical coupling channels that can be enabled or disabled with optical attenuators, we have constructed a small network whose coupling structure can be easily re-configured, allowing for the multiple network structures presented in Chapters 4 and 5. By including a digital signal processing (DSP) board in each feedback loop, we can change many of the parameters of the loop simply by reprogramming the DSP board. This also allows for excellent parameter matching between the loops. Overall, this is a versatile experimental system, which can be used for experimentally studying many questions of coupled dynamical systems.

## 3.2 Background

Optoelectronic feedback loops have been used by many research groups in recent years in order to study nonlinear dynamics, chaos, and synchronization. These experimental systems are excellent test-beds to verify and expand upon theory of dynamical systems, as well as to gain insight into behaviors that may be present in natural or man-made systems. The flexibility of the system parameters, the ability to produce a variety of dynamical behaviors, and the ease of modeling make this system an ideal experiment to study coupled oscillators. Although mathematical models are often used for computational studies because they have well-understood equations, they do not have the noise, mismatch, and nonidealities present in real, physical systems. Many physical systems have parameters or equations that are not easy to obtain or measure. The optoelectronic feedback loops described here act as a bridge between numerical models and complex experimental systems.

Many studies have used a laser with optical feedback in order to generate chaos or other dynamical states. Here, however, we create feedback that does not involve the laser. Rather, the laser is completely outside of the dynamical loop so that the laser generates CW light that feeds and is amplitude-modulated by the feedback loop. By removing the laser from the feedback loop, we have a system that is less-sensitive than an all-optical system is to hard-to-control physical parameters such as temperature. Additionally, we are able to use commercially available components and can more easily create multiple matched dynamical systems.

The main features of an optoelectronic feedback loop are a nonlinear element,

a time delay, a filter, and feedback. Because this system includes a time delay and nonlinearity as part of a feedback loop, it is an attractive experimental system to study, in order to gain insight into many other systems that contain a nonlinearity and time-delayed feedback. By changing the parameters in the feedback loop, these systems display a wide variety of behaviors, from fixed point to periodic oscillations to quasiperiodic oscillations to high-dimensional chaos.

The first instance of using an optoelectronic feedback loop to generate nonlinear dynamics was by Neyer and Voges in 1982 [59]. In 2005, Chembo and colleagues reported “chaotic breathers” in an optoelectronic feedback loop experiment, and they compared their results with numerical simulations from a mathematical model, which gave excellent agreement [60].

The optoelectronic feedback loops studied by Chembo, et al. have been used to study synchronization, particularly synchronization between chaotic signals. In 2005, Argyris and his collaborators proposed and implemented a method for using optoelectronic feedback loops (or all-optical feedback loops) to generate chaotic signals that could be used to encrypt data signals transmitted over an optical communication network [14]. A receiver was synchronized to the transmitter, in order to decode the transmitted message. The scheme was implemented on a fiber optic communication network in Athens, and the received signal was successfully recovered from the transmitted chaotic signal using an open-loop architecture at the receiving end.

In 2008, an experimental chaotic feedback loop was synchronized to a simulated numerical model of the same system by Cohen, Ravoori, Murphy, and Roy, in

order to study prediction of high-dimensional chaos [61]. By removing the numerical input and observing the divergence between the signal in the experiment and the simulated signal, they were able to calculate the finite-time Lyapunov exponent, which quantifies the predictability of a system. Using this scheme, they found that the numerical simulations could predict the experimental behavior for up to several times the round-trip time delay of the feedback loop.

A study published in 2010 by Murphy, et al. analyzed the conditions for which two of these optoelectronic oscillators could identically synchronize [62].

In 2009, the same group constructed two identical feedback loops that were coupled as transmitter and receiver so that their chaotic dynamics were synchronized [63]. In communications, it is possible that there are some slowly-varying changes in the coupling channel, which can disrupt the synchronization between a transmitter and receiver. Sorrentino and Ott developed a theory for adaptively changing the coupling strength in order to compensate for the perturbations in the communication channel and maintain synchrony [64–66]. Ravoori, et al. reported an experimental demonstration of an adaptive algorithm for maintaining synchronization between two optoelectronic feedback loops. In order to implement the adaptive algorithm, it was necessary to include in the feedback loop a digital signal processing (DSP) board, whereas previous studies on these feedback loops had only analog components. The use of the DSP board will be further described in Section 3.3.2.

Another experimental demonstration of adaptive synchrony between chaotic optoelectronic oscillators was published in 2010 by Cohen, et al. [67]. For this set of experiments, the system under consideration was a network of three nominally

identical, mutually coupled optoelectronic oscillators. An adaptive algorithm was implemented, using DSP boards, that successfully maintained synchrony between the three oscillators in the presence of time-varying coupling strengths. Furthermore, the scheme allowed for an estimate of an unknown variation in the coupling channel, demonstrating that this type of adaptive algorithm has potential use in a sensor application, in addition to the communication application.

### 3.3 A Single Feedback Loop

As mentioned in Section 3.1, the primary features of a single loop are a non-linearity, time delay, and self-feedback. A diagram of the experimental system is shown in fig. 3.1.

#### 3.3.1 Components

The laser that provides the optical signal into the feedback loop is a distributed feedback (DFB) laser diode (Bookham that operates at a wavelength of 1550 nm, which is within the range of standard telecommunication wavelengths, making it easy to obtain fiber optic components for this system. The laser diode is placed in an butterfly-type laser diode mount (ILX Lightwave), and is operated with a laser diode driver (LDD) and thermoelectric cooling (TEC) temperature controller module (ILX Lightwave). The output of the laser is CW light that is coupled into a single mode (SM) fiber.

The nonlinearity is created by a Mach-Zehnder modulator (MZM) (Lucent

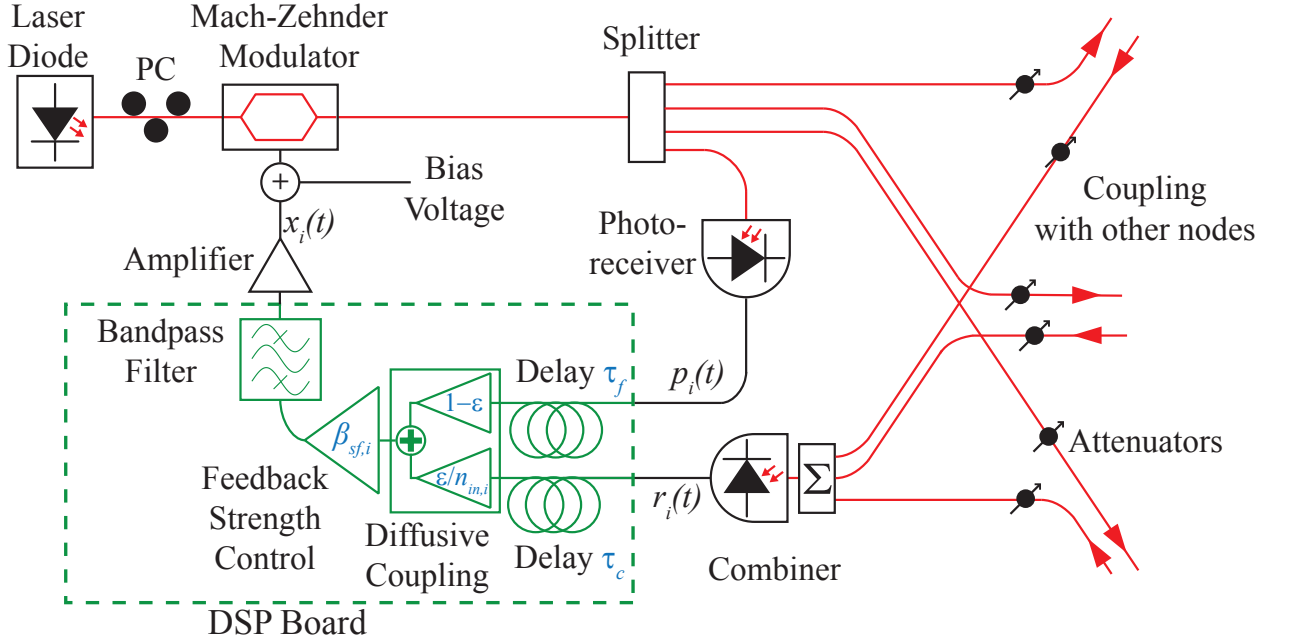


Figure 3.1: Experimental set-up of a feedback loop. The index  $i$  denotes the node number in a small network of multiple feedback loops.

2623NA) . The MZM has an optical input (power  $P_{in}$ ), an optical output (power  $P_{out}$ ), and a voltage input ( $V(t)$ ), as illustrated in fig. 3.2(a). The MZM is essentially an interferometer between two waveguides. The input light is split into two paths, which an electro-optical material whose index of refraction is dependent on the applied electric field, thus changing the effective path length of the two arms of the MZM. The electric fields applied to the two paths are in opposite directions, resulting in refractive index changes that are opposite in sign for the two paths. The two optical signals are recombined, resulting in interference between the two electromagnetic waves. The optical input to the MZM is the optical signal from the laser diode, but the MZM has a polarizer on the input, so it is necessary to control the polarization of the input to the MZM to ensure that the polarization

of the incoming light is parallel to the transmission axis of the polarizer, resulting in maximum transmission through the MZM. To control the polarization, we use a paddle-type polarization controller (PC), which consists of three paddles wound with fiber. By rotating the relative positions of the paddles, the fiber is strained, resulting in high transmission for one particular polarization state. By measuring the output power  $P_{out}$  of the MZM, keeping the input voltage signal constant, while adjusting the positions of the paddles until  $P_{out}$  is maximum, it is possible to control the polarization of the light input to the MZM so that it is parallel to the polarizer built in to the MZM. This must be done before each measurement, as thermal fluctuations and other environmental factors cause changes in the fibers.

The output optical power  $P_{out}$  is a function of the input optical power  $P_{in}$  and the input voltage signal  $V(t)$  [62]:

$$P_{out}(t) = P_{in} \cos^2(\alpha V(t) + \phi_0), \quad (3.1)$$

where  $\alpha$  is a normalization factor and  $\phi_0$  is the bias of the MZM. In practice, we refer to the normalized input to the MZM,  $x(t)$ :

$$x(t) = \alpha V(t) = \frac{\pi V(t)}{2 V_\pi}, \quad (3.2)$$

where  $V_\pi$  is the half-wave voltage of the MZM. In order to control  $\phi_0$ , a DC bias voltage signal is input to the MZM. On some models of MZMs, there are two voltage inputs, one for a DC bias signal and another for the RF input. However, on the MZMs used in the experiments presented in this thesis, there is a single voltage input port on the MZM, requiring an adder circuit or bias-tee for proper biasing.

The voltage required to take the MZM from minimum transmission to maximum transmission is referred to as  $V_\pi$  and is an important characteristic of the MZM. MZMs are typically used in optical communication applications, where a binary voltage input signal modulates an optical signal that is then transmitted over fiber optics. With a binary voltage signal, the MZM acts as a switch, transmitting no light for one voltage level, and transmitting maximum power for the other voltage value. A smaller value of  $V_\pi$  means that a smaller amplitude of the input signal is required to switch the MZM from minimum transmission to maximum transmission. The modulators used in Chapters 4 and 5 of this thesis have  $V_\pi = 3.4$  V. A typical transmission curve is shown in fig. 3.2(b).

For the low-speed applications described in Chapters 4 and 5, we designed and built an adder circuit to add a DC bias voltage to the RF signal. The circuit diagram is shown in fig. 3.3. For a higher speed version of the same system, we used an integrated bias tee module (Pasternack PE1607 or Picosecond Pulse Labs 5547-107). The bias of the MZM must be adjusted before each measurement. For the experiments in Chapters 4 and 5, the bias is set to  $\phi_0 = \pi/4$ . This is done by first adjusting the potentiometer of the bias circuit so that the output power  $P_{out}$  is maximum, by observing the photoreceiver's voltage signal  $p(t)$  on an oscilloscope. The signal  $p(t)$  is shown in fig. 3.1 and is monitored in order to adjust the optical power that is injected into the MZM. Then, the bias voltage is increased until the photoreceiver output is half of the maximum, setting the bias phase of the MZM at  $\phi_0 = \pi/4$ . For the experiments in Chapters 4 and 5, the laser power and position of the polarization controllers was adjusted so that the maximum transmission of

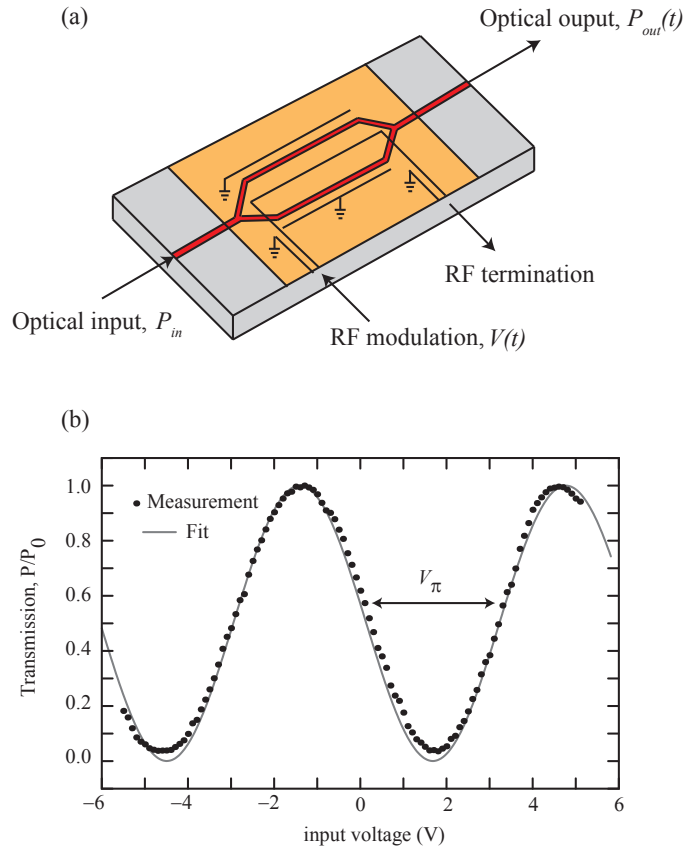


Figure 3.2: (a) Schematic of a MZM [68]. (b) Typical transmission curve of the MZM, data and fit of  $\cos^2$  [68]. The DC bias is set so that an input modulation voltage of  $V = 0$  corresponds to a bias phase of  $\phi_0 = \pi/4$ . The half-wave voltage is  $V_\pi = 3.4$  V.

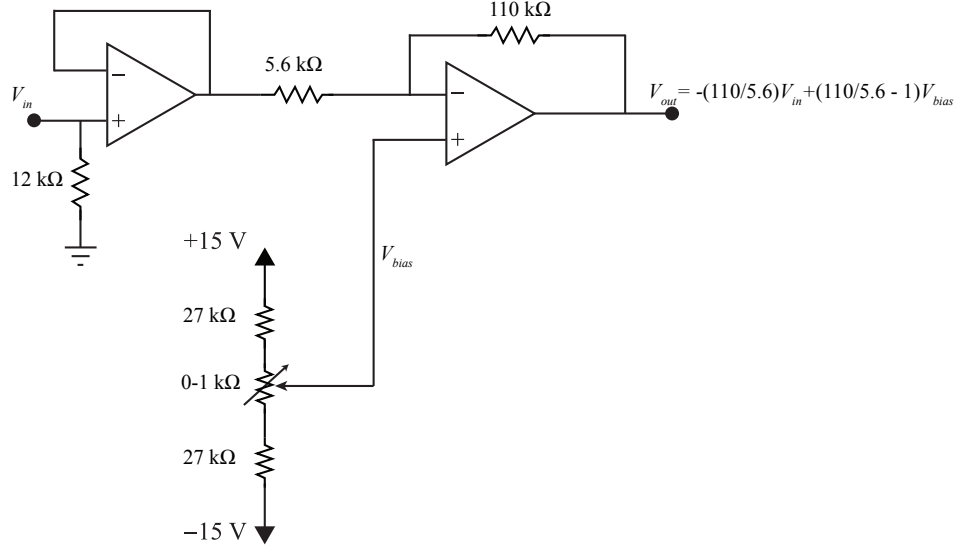


Figure 3.3: Circuit diagram of voltage amplifier and bias circuit used to bias MZM.

the MZM provided a signal of  $p = 700$  mV from the feedback photoreceiver. Then the bias voltage on the modulator was increased so that the transmission provided a signal of  $p = 350$  mV and that the MZM was operated at the negative slope, as indicated in fig. 3.2(b).

The optical output of the MZM is converted into a voltage signal by a photoreceiver circuit, which was designed and implemented on a printed circuit board (PCB), and is shown in fig. 3.4. The circuit consists of a photodiode, which converts the optical signal (in fiber) to a photocurrent, followed by a transimpedance amplifier with gain of 1000 V/A, to convert the current to a voltage signal. In the experiments presented in Chapters 4 and 5, each node has one PCB that contains three separate circuits: one photoreceiver circuit for the feedback signal, one photoreceiver circuit for the coupled signal (coupling will be discussed in a later

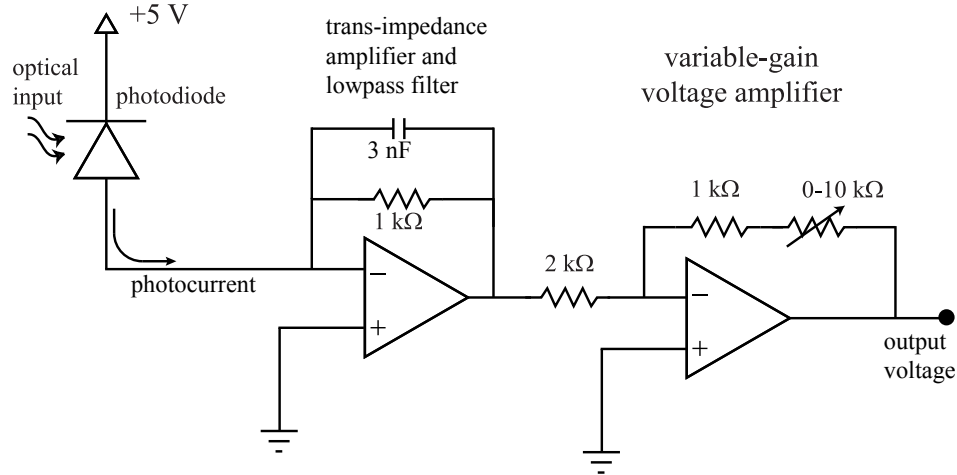


Figure 3.4: Circuit diagram of photoreceiver circuit.

section), and a bias and voltage amplifier circuit for the input of the MZM. A photo of one PCB is shown in fig. 3.5. For the high-speed version of the system, we use a high-speed photodetector, Discovery (DSCR402). The Discovery photoreceiver is attached to an aluminum heat sink and has fiber-coupled input and AC-coupled RF output.

Another important feature of a feedback loop is a filter. Some feedback systems display chaos with only a low pass filter [69], but we use a bandpass filter with cut-on frequency  $f_H$  and cut-off frequency  $f_L$ . The filter can be implemented as two filters, a high pass filter and a low pass filter.

The time delay in the feedback loop is a critical part of the system. A time delay can be implemented using lengths of fiber optic cables or electrical delay lines. In Section 3.3.2, we will describe how the delay is implemented on the DSP board.

Finally, the loop includes a voltage amplifier. In the experiments described

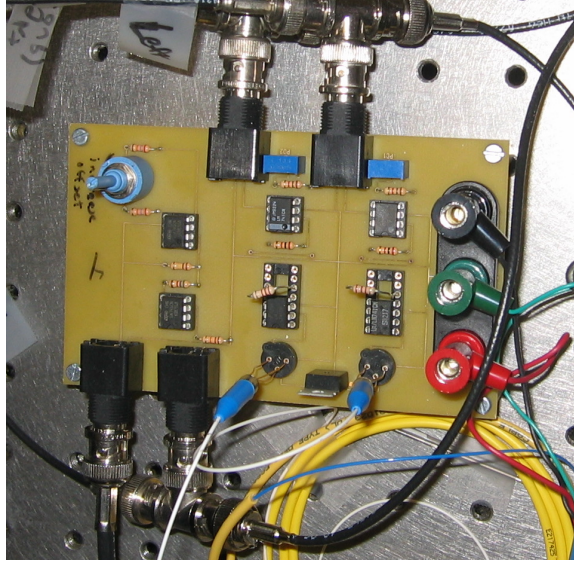


Figure 3.5: Printed circuit board containing bias and voltage amplifier circuits, along with photoreceiver circuits.

in Chapters 4 and 5, we use a voltage amplifier with a gain of  $V_{out}/V_{in} \approx -20$  immediately before the input to the MZM. This voltage amplifier is necessary in order to provide an adequate amplitude signal into the MZM. The signal out of the DSP board is limited to a few hundred mV in amplitude, so an amplifier with a gain of 20 will ensure that the voltage signal applied to the MZM has an amplitude on the order of  $V_\pi$ . The circuit diagram is shown in 3.3 as part of the biasing circuit for the MZM.

Although many of the parameters of the feedback loop can be varied, the feedback strength  $\beta$  is the primary parameter we vary in order to control the type of dynamics produced by the loop.  $\beta$  is a combined feedback strength, which lumps together multiple factors: the power of the laser light input to the MZM, the gain of the photoreceiver, loss in the optical fiber, and gain or loss due to an amplifier or

attenuator. Experimentally,  $\beta$  is typically varied by changing the laser power or by changing the gain of a variable amplifier. Because we are working with normalized units,  $x(t)$ , as defined in eq. (3.2),  $\beta$  can be defined:

$$\beta = \frac{\pi RGP_{in}}{2 V_{\pi}} \quad (3.3)$$

where  $R$  is the responsivity of the photodiode in the photodetector (units of A/W), and  $G$  is the total net gain of the system (units of V/A), which includes the gains of the transimpedance amplifier and voltage amplifiers. Because  $P_{in}$  has units of W,  $\beta$  is a unitless quantity.

### 3.3.2 DSP Implementation

In order to perform the experiments reported in [3, 62, 63, 67, 70] and in this thesis, it was necessary to include a DSP board (TMS320C6713 TSK from Spectrum Digital, which uses the TMS320C6713 DSP from Texas Instruments) to implement the coupling and other functions. In [62, 63, 67], the DSP board was used to implement the adaptive algorithm used to maintain synchrony in the presence of a time-varying coupling strength. The DSP program is written using Code Composer Studio, a programming development environment specifically for the DSP board. The programs are written in the C language, and then are loaded on to the DSP via a USB interface from the computer. Once the program is loaded and running, it continues to run autonomously as long as it is powered.

The DSP is used to implement the filtering as a digital two-pole bandpass filter. Implementing the filter digitally has the benefit of ensuring that multiple

systems comprising our network have identical filter characteristics. With analog filters, it is difficult to match the filters between two or more feedback loops, and mismatches in the filters can prevent identical synchrony. For the experiments here, we use a two-pole digital bandpass filter, with  $f_{HP} = 100$  Hz,  $f_{LP} = 2.5$  kHz, and sampling frequency  $F_s = 24$  kSamples/sec.

The delays for both the feedback and coupling are implemented on the DSP board. The voltage values are stored in a memory buffer at intervals of the sampling time  $T_s = 1/F_s$  and delayed by an integer number of sampling times. The feedback and coupling delays can be defined separately, but just as with the coupling strength, the coupling delay will be the same for all coupling links incoming to the same DSP board. At these speeds, all of the delay is a result of the DSP board. There is some fixed delay that is intrinsic to the ADC, DAC, and other processing on the DSP board. This delay can be measured using a network analyzer (NA). To do this, we break the feedback loop between DSP board and the voltage amplifier. With the proper bias of the MZM set, a small signal sine wave is sent into the voltage amplifier as the frequency is swept. The phase of the output of the DSP board is measured and plotted as a function of frequency. The inverse of the slope of this line is the total time delay of the system. For the experiments reported in Chapters 4 and 5, the total time delay without any added delay in the program is equivalent to 33.7 time steps, so the minimum time delay possible for the system is 34 time steps (though the DSP program requires a non-zero added time delay).

It is often desirable to turn on and off the feedback or coupling in order to start the system from random initial conditions and to observe the time traces of both the

uncoupled and coupled feedback loops. This is accomplished by soldering wires to two of the DIP switches on the DSP board (one for feedback and one for coupling), and using a function generator to periodically turn off and on the feedback and/or coupling as desired.

For the DSP boards that we are using, we are limited to audio frequencies on the order of tens of kHz. However, in place of slower DSP boards, higher speed FPGA (field programmable gate array) boards or other high-speed processing can be used to scale the system to order of magnitude higher speeds [62, 71].

### 3.3.3 Equations of Motion

An equivalent mathematical block diagram to the physical system of a single feedback loop is shown in fig. 3.6. Because all of the operations except for the nonlinearity are time-independent and linear functions, they can be interchanged without changing the mathematical meaning or equations.

#### 3.3.3.1 Continuous Time

As described by eqns. (3.1) and (3.2), the output of the MZM is proportional to  $\cos^2(x(t) + \phi_0)$ . This signal is then delayed by feedback time delay  $\tau_f$  and scaled by feedback strength  $\beta$  (defined in eq. (3.3)) and inverting amplifier, resulting in

$$y(t) = -\beta \cos^2(x(t - \tau_f) + \phi_0). \quad (3.4)$$

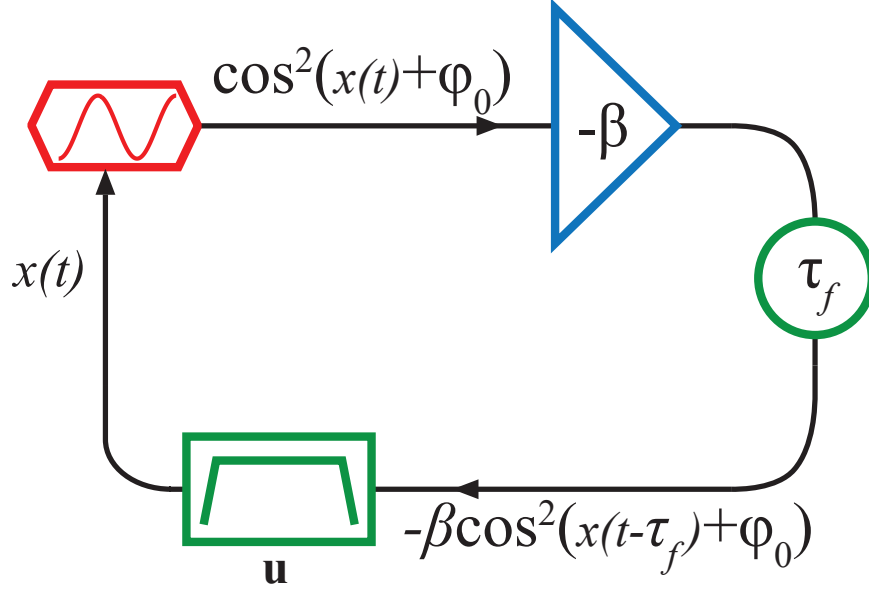


Figure 3.6: Block diagram of a single feedback loop.

This signal is the input to the filter, which is a two-pole linear bandpass filter. In the time domain, the output to the filter  $x(t)$  can be described by

$$\dot{\mathbf{u}} = \mathbf{E}\mathbf{u}(t) + \mathbf{F}y(t) \quad (3.5)$$

$$x(t) = \mathbf{G}\mathbf{u}(t) + \mathbf{H}y(t) \quad (3.6)$$

where  $\mathbf{u}(t)$  is the internal state vector of the filter [62]. The matrices  $\mathbf{E}$ ,  $\mathbf{F}$ ,  $\mathbf{G}$ , and  $\mathbf{H}$  describe the filter:

$$\mathbf{E} = \begin{bmatrix} -(\omega_L + \omega_H) & -\omega_L \\ \omega_H & 0 \end{bmatrix}, \quad \mathbf{F} = \begin{bmatrix} -\omega_L \\ 0 \end{bmatrix}, \quad \mathbf{G} = [1 \quad 0], \quad \text{and} \quad \mathbf{H} = 0, \quad (3.7)$$

where  $\omega_H = 2\pi f_H$  and  $\omega_L = 2\pi f_L$  are the angular frequencies corresponding to the high-pass cut-on and low pass cut-off frequencies, respectively.

Combining these equations gives the equation of motion as a delay-differential

equation of the state-space vector:

$$\dot{\mathbf{u}} = \mathbf{E}\mathbf{u}(t) + \mathbf{F}\beta \cos^2[\mathbf{G}\mathbf{u}(t - \tau_f) + \phi_0] \quad (3.8)$$

### 3.3.3.2 Discrete Time

Although the development of the model above is for a continuous time system, the use of the DSP board means that our experiment actually has a component that operates in discrete time. Because the filter is implemented on the DSP board, it is a discrete time filter with sampling time  $T_s$ . For a filter input  $y[n]$ , output  $x[n]$ , and state-space vector  $\mathbf{u}[n]$ , where  $n$  is the step number, the state-space equations for a filter can be described by

$$\mathbf{u}[n + 1] = \mathbf{E}\mathbf{u}[n] + \mathbf{F}y[n] \quad (3.9)$$

$$x[n] = \mathbf{G}\mathbf{u}[n] + \mathbf{H}y[n], \quad (3.10)$$

which is analogous to the continuous time equations of eqs. (3.5) and (3.6), but with different matrices,  $\mathbf{E}$ ,  $\mathbf{F}$ ,  $\mathbf{G}$ , and  $\mathbf{H}$ , as defined in [62].

For a feedback delay of  $k_f$  steps, the discrete-time version of eq. (3.4) is

$$y[n] = \beta \cos^2(x[n - k_f] + \phi_0). \quad (3.11)$$

For modeling the system, we use the discrete-time description and implement the equations as a discrete-time iterated map. In the model, the filter is a second-order discrete-time implementation of a Butterworth bandpass filter.

### 3.3.4 Dynamics

Work reported in [61,62,68,71] describes the wide variety of dynamical behaviors that can be generated from these optoelectronic feedback loops. By increasing the feedback strength  $\beta$ , a single feedback loop can display fixed point, periodic, quasi-periodic, or chaotic solutions. Figure 3.7, from [68], shows time traces of three different types of dynamics. As  $\beta$  is increased from right to left, the dynamics are periodic, quasiperiodic, and then chaotic. The time traces from an experiment correspond well to the time traces from simulation, as shown in fig. 3.7. Figure 3.8, from [68], gives a more complete picture of the dynamics generated by this system. The grayscale indicates the occurrence of that particular amplitude value (indicated on the y-axis) as the feedback strength  $\beta$  is swept along the x-axis. As  $\beta$  is increased, the dynamics increase in complexity until there is broad-band chaos, indicated by a featureless distribution, without any dominant values. For the bifurcation diagrams, simulation and experiment agree qualitatively. Similar transitions between types of dynamics occur in experiment and simulation, but the particular values of  $\beta$  may not be the same, due to mismatches and non-idealities in the experimental system.

## 3.4 Coupled Feedback Loops

As seen by the variety of dynamical behaviors that can result simply by changing the feedback strength, it is clear that a single feedback loop is a very interesting object of study. Furthermore, by coupling two or more dynamical systems together, many fascinating phenomena can be observed beyond the dynamical behavior of

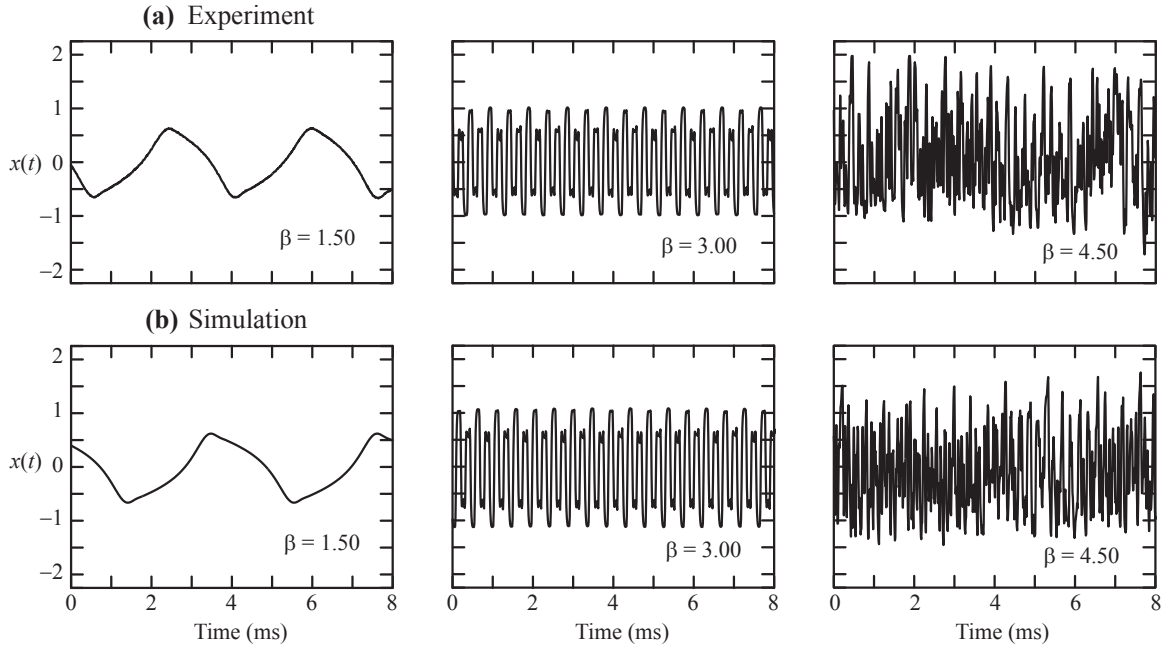


Figure 3.7: Time traces for different dynamics [68].

a single system [72]. This is particularly true for the case of chaotic systems, as experimental observations of synchronization of chaos are quite remarkable.

In order to study synchronization patterns in a small network of oscillators, we have an experiment of four of these feedback loops that are coupled together. We have the capability to study an all-to-all coupled network, as shown in fig. 3.9, or to remove links and study network structures with fewer connections.

The feedback loops presented here are coupled optically. The optical output of the MZM is split using a 1x4 optical splitter (Fiber Instrument Sales) into four equal optical signals. One of the four splitter outputs is the feedback signal, and the other three splitter outputs are the coupling signals to the other three nodes. Optical attenuators are used to control the optical power in the coupling links. For

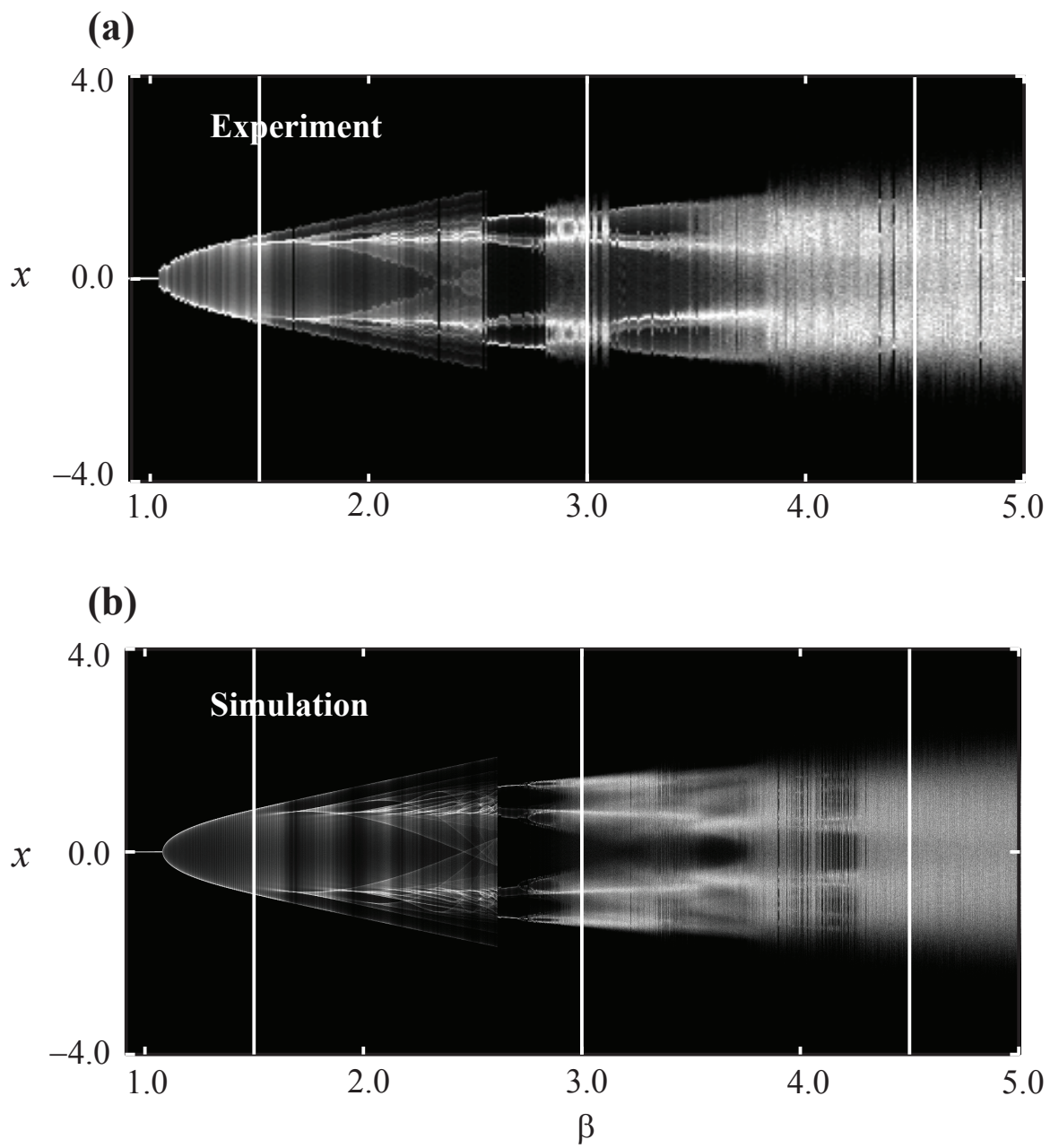
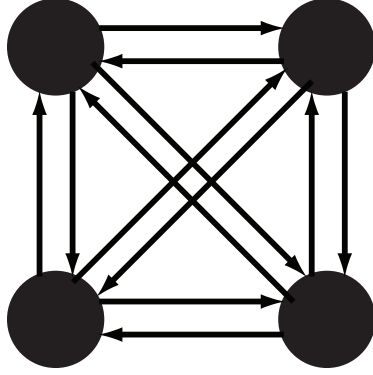


Figure 3.8: Bifurcation diagram of a single feedback loop [68].



$$\mathbf{K} = \frac{1}{3} \begin{pmatrix} 0 & 1 & 1 & 1 \\ 1 & 0 & 1 & 1 \\ 1 & 1 & 0 & 1 \\ 1 & 1 & 1 & 0 \end{pmatrix}$$

Figure 3.9: All-to-all network structure for four feedback loops. This is the maximally-connected network for four oscillators, but links may be removed to create many different network structures.

eight of the twelve coupling channels, the optical power is controlled using a digital optical attenuator (8-channel attenuator by Oz Optics), which is controlled via a LabView program. The remaining four channels are controlled with manual screw-type attenuators. In principle, these attenuators can be used to set the coupling strengths to any positive values we would like. However, in these experiments, we use the attenuators simply to add or remove the coupling links. For the links that we wish to be present for a particular network structure, we adjust the attenuation so that the signals are all equal when the feedback and dynamics are disabled. To check this, we observe the voltage signal produced by the photoreceiver circuit of the coupling signals and balance these voltage signals,  $r$ . Because there are slight variations in the gains of the photoreceiver circuits, the level of optical power will vary slightly for each link in order to compensate.

As mentioned in Section 3.3.1, there are two photoreceivers for each feedback loop. The first photoreceiver is only for the feedback signal, and the second is for

the coupled signals. To form a single coupling signal, the three signals coupled from the other nodes are fed into a 3x1 optical combiner (Fiberdyne Single Window Splitter/Coupler), and the output of the combiner is the optical signal measured by the second photoreceiver. The optical signals from different nodes add incoherently (i.e.  $P_{total}(t) = P_1(t) + P_2(t) + \dots$ ) because  $(\frac{c}{\lambda_1} - \frac{c}{\lambda_2}) \gg$  the bandwidth of the photoreceiver. When balancing the optical powers of feedback and coupling, as well as biasing the MZM, the feedback loops were opened after the photoreceivers.

Although we do not use an adaptive coupling algorithm like that mentioned in sec. 3.2, the DSP board can be used to implement the coupling scheme. The DSP board can have two inputs and two outputs. One of the two inputs is the voltage signal from the feedback photoreceiver, and the other input is the voltage signal from the coupling photoreceiver. In this way, the DSP can distinguish and separately process the feedback signal and the combined coupling signal. However, because the coupling signal is combined signal from the other three nodes, it is important to note the restriction that the DSP board cannot distinguish between a coupling signal from one node and from a signal from a different node. If we wish to make changes to the coupling strengths so that signals going into a single node have different feedback strengths, we must implement it off of the DSP board.

Different coupling schemes can be used to couple two or more feedback loops, as described in [62]. The scheme used here is called *diffusive coupling*. In this coupling scheme, we define a global coupling strength,  $0 < \varepsilon < 1$  that defines the relative weights of the coupled signal into the node and the feedback signal. The feedback signal is scaled by a factor of  $(1 - \varepsilon)$ , which is implemented on the DSP

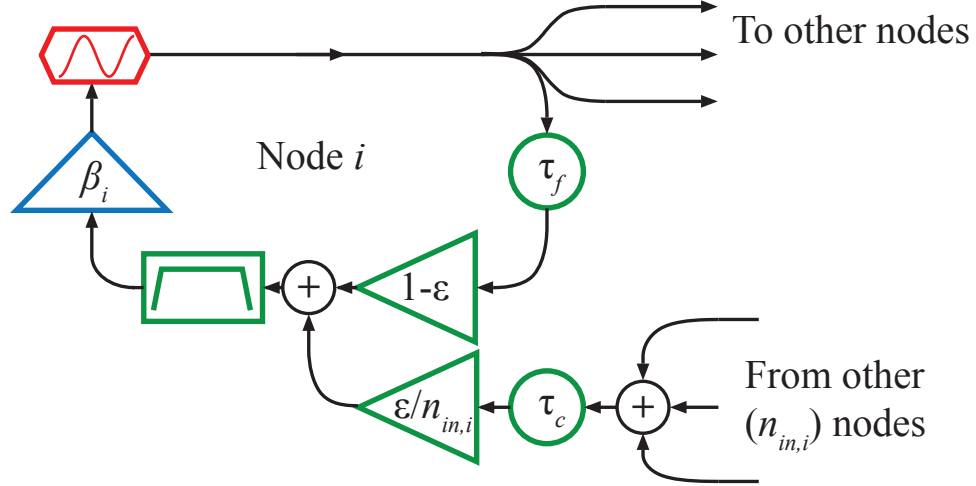


Figure 3.10: Block diagram for coupled feedback loops.

board. For diffusive coupling, the total coupling signal must have a weight of  $\varepsilon$ , which means that if there are more than one coupling links coming into a node, each signal must be scaled by a factor of  $\bar{\varepsilon} = \varepsilon/n_{in}$ , where  $n_{in}$  is the number of links coming into that particular node, as the  $n_{in}$  coupling signals are summed. On the DSP board, because the input to the board sees the  $n_{in}$  signals combined into a single input, the single input signal is weighted by  $\bar{\varepsilon}$ . The result of this coupling scheme is that when identical systems are coupled this way, the equations admit a solution for identical synchrony between the systems, and the equations of motion for the synchronized oscillators are exactly the same as the equations for a single feedback loop without coupling. A block diagram of a single node with  $n_{in}$  input signals is shown in fig. 3.10.

In order to properly balance the coupling strengths in the experiment, the first step is to adjust the laser powers and MZM biases for each of the nodes, as described

in sec. 3.3.1, with feedback disabled, so that  $p_1 = p_2 = p_3 = p_4 = 350$  mV ( $p_i$  and  $r_i$  are defined in fig. 3.1). Then, one laser at a time is turned on, and the received signals from the other nodes are monitored and balanced. So if laser 1 is the only laser turned on, we adjust the attenuators (and variable gain of the photoreceivers and/or the laser powers, if necessary, assuming the MZM bias is  $\phi_0 = \pi/4$ ) until  $r_2 = r_3 = r_4 = p_1 = 350$  mV. After this process has been repeated separately for each laser, the coupling strengths are all equal, unless the coupling is changed on the DSP boards. If we wish to remove a link, we increase the attenuation of that individual link until no optical signal is transmitted.

When multiple oscillators are coupled in a small network, it is typical to define a coupling matrix,  $\mathbf{K}$ , where  $K_{ij}$  defines the coupling strength from node  $j$  to node  $i$ . In the experiments discussed in Chapters 4 and 5, we will restrict ourselves to coupling matrixes where the row-sum is uniform for all rows of  $\mathbf{K}$ . When we define  $\mathbf{K}$  in this way, we can write equations for the coupled systems as:

$$\dot{\mathbf{u}}_i(t) = \mathbf{E}\mathbf{u}_i(t) - \mathbf{F}\beta_i \cos^2(x_i(t - \tau_f) + \phi_0), \quad (3.12)$$

$$x_i(t) = \mathbf{G}\{\mathbf{u}_i(t) + \varepsilon \sum_j K_{ij}[\mathbf{u}_j(t - \tau_c + \tau_f) - \mathbf{u}_i(t)]\}. \quad (3.13)$$

In these equations, we keep the the filter (defined by matrices  $\mathbf{E}$ ,  $\mathbf{F}$ , and  $\mathbf{G}$ , and  $\mathbf{H} = 0$  from eq. (3.7)) identical for each node, as well as identical time delays for each node, though we do allow for a different coupling delay from the feedback delay, i.e.  $\tau_c \neq \tau_f$  is allowed. We also hold the total coupling strength  $\varepsilon$  and the bias phase  $\phi_0$  constant for all nodes, though these equations could be written more generally to allow for different values of  $\varepsilon$  and  $\phi_0$  for each node. We do allow for a different

feedback strength  $\beta$  for each node.

When coupled, these optoelectronic oscillators can produce synchronized, yet still chaotic, dynamics, as reported in [61–63, 67, 70] and discussed in Section 3.1. In these cases, the synchronization is identical and isochronal. In the next two chapters of this dissertation, we will discuss synchronization patterns between chaotic and periodic oscillators that include, but are not limited to, isochronal synchrony, in which two or more oscillators have the same amplitude dynamics in time. Additionally, we will see examples of group synchrony and cluster synchrony, where multiple oscillators are coupled together, but they form clusters or groups of isochronally synchronized oscillators, but oscillators from different groups do not isochronally synchronize. We will also see lag synchrony, where oscillators may be synchronized in amplitude or phase, but there is a time delay between two oscillators.

## Chapter 4: Group and Cluster Synchrony in an Experiment of Four Delay-coupled Optoelectronic Feedback Loops

*This chapter is based on work from the following publications: Experimental Observations of Group Synchrony in a System of Chaotic Optoelectronic Oscillators, C. R. S. Williams, T. E. Murphy, R. Roy, F. Sorrentino, T. Dahms, E. Schöll, Phys. Rev. Lett. 110, 064104 (2013), ©2013 by the American Physical Society; Group Synchrony in an Experimental System of Delay-coupled Optoelectronic Oscillators, C. R. S. Williams, T. E. Murphy, R. Roy, F. Sorrentino, T. Dahms, E. Schöll, Conference Proceedings of 2012 International Symposium on Nonlinear Theory and its Applications (NOLTA2012), 70-73 (2012).*

### 4.1 Overview

Optoelectronic oscillators with time-delayed feedback have been found to show a multitude of different dynamical behaviors ranging from steady-state to chaotic dynamics depending on parameter [62, 70, 73–76]. In this chapter we experimentally demonstrate group synchrony, with two groups that display significantly different dynamics when uncoupled. Remarkably, the synchronized oscillators in one group are not directly coupled to each other; they are coupled only to those of the other

group. In *group synchronization* the local dynamics in synchronized clusters can be different from the dynamics in the other cluster(s), which extends the possibility of synchronization behavior to networks formed of heterogeneous dynamical systems, as they appear in a variety of applications. *Cluster synchrony* is a special case of group synchrony, in which all of the nodes have identical equations and parameters, but they are not all identically synchronized, rather, a node will be identically synchronized only to certain other nodes.

## 4.2 Background

The last years have seen a vast increase in the interest in coupled dynamical systems, ranging from a few coupled elements to complex networks [77, 78]. Besides the focus on network structure and topology, the research area of synchronization in networks has grown rapidly [26, 79]. The groundbreaking work on the *master stability function* (MSF) by Pecora and Carroll has bridged the gap between topology and dynamics by allowing predictions about synchronization based solely on the nodes' dynamics and the eigenvalue spectrum of the coupling matrix [80].

While the MSF theory was originally developed for identical, isochronous synchronization, more complex patterns of synchronization are observed in, e.g., neural systems, genetic regulation, or optical systems [81–90]. These patterns include, for example, sublattice synchronization in coupled loops of identical oscillators with heterogeneous delays [91], pairwise synchronization of pairs of identical nodes coupled through a common channel [92], and more general group synchronization [2]. More-

over, these synchronous patterns can be observed even when there is no intra-group coupling. Sorrentino and Ott have generalized the MSF approach to group synchronization [2], and recent work by Dahms *et al.* considers time-delayed coupling of an arbitrary number of groups [93].

### 4.3 Experimental Set-up

To experimentally investigate these phenomena, we constructed four optoelectronic feedback loops, which act as the four nodes of the network. We consider several coupling schemes. In the first one, the nodes are coupled together in the configuration shown in Fig. 4.1(a) in order to form two groups. There are no direct coupling links between two nodes in the same group. However, a node is coupled bidirectionally to both of the nodes in the other group. In this experiment, the coupling strength,  $\varepsilon$ , and coupling delay,  $\tau$ , are the same for all coupling links. However, the parameters of the nodes differ depending on which group the nodes are in. Both of the nodes in group A are identical, and both of the nodes in group B are identical, but the nodes in group A are not identical to those in group B. In Fig. 4.1(a), the coupling links are shown in black (arrows in each direction indicate bidirectional coupling), and the self-feedback of the nodes is indicated by the colored lines and arrows.

A schematic of a single node is shown in Fig. 4.1(b), where red lines indicate optical fibers, and black or green lines indicate electronic paths. In each node, light from a diode laser passes through a Mach-Zehnder modulator (MZM), whose output

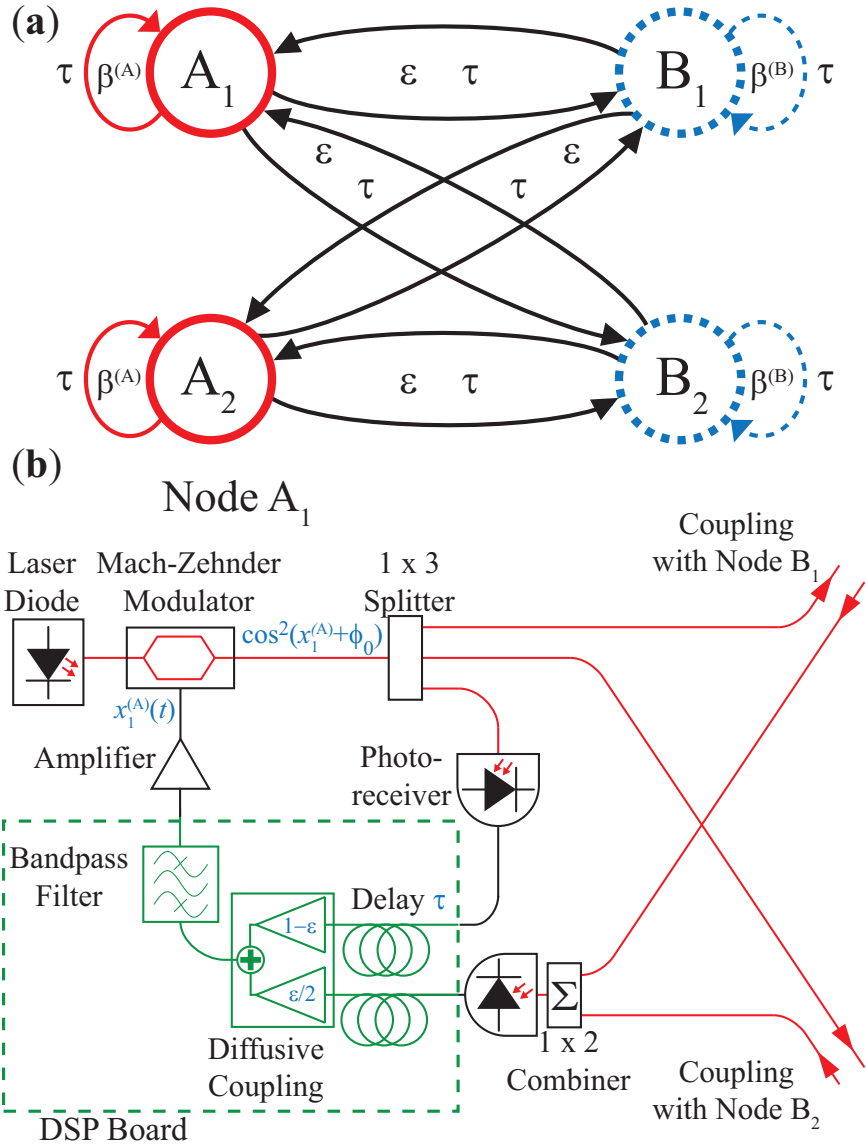


Figure 4.1: (a) Schematic of four nodes separated into two groups, A (red, solid) and B (blue, dashed). (b) Experimental setup of a single node, showing coupling to the other nodes according to the configuration in (a).

light intensity is  $\cos^2(x + \phi_0)$  for an input voltage signal  $x$ . There is a controllable bias phase of the MZM, which we set to be  $\phi_0 = \frac{\pi}{4}$ . The optical signal is split into three equal signals: one is the feedback signal, and the other two are the coupling to the two nodes in the opposite group. A photoreceiver converts the feedback optical signal to an electrical signal, which is one of the two inputs to the digital signal processing (DSP) board. The incoming optical signals from the two nodes of the other group are combined optically before a second photoreceiver converts the composite coupled signal to an electronic signal, which is the second input of the DSP board. The DSP board implements the feedback and coupling time delays, which are the same for this experiment ( $\tau = 1.4$  ms), and a diffusive coupling scheme. The feedback signal is scaled by a factor of  $(1 - \varepsilon)$ , while each incoming signal to a node is scaled by a factor of  $\varepsilon/n_{\text{in}}$ , for the global coupling strength,  $\varepsilon$ , and the number of links incoming to a node,  $n_{\text{in}}$ . For the configuration shown in Fig. 4.1(a),  $n_{\text{in}} = 2$  for all nodes, but in general,  $n_{\text{in}}$  can be different for each node. The feedback and coupled signals are summed on the DSP board.

The DSP board also implements a digital filter, which is a two-pole bandpass filter with cutoff frequencies at 100 Hz and 2.5 kHz and a sampling rate of 24 kSamples/s, and also scales the combined signal by a factor, which controls the feedback strength, which we denote  $\beta$ . The output of the DSP board is amplified with a voltage amplifier, whose output drives the MZM. Although  $\beta$  is a combination of gains of the photoreceiver, amplifier, and other components, the DSP board is the only place where the gain is changed.

For this experiment, all parameters except for  $\beta$  are identical in all four nodes.

We keep  $\beta$  identical among the members of each group but allow a different  $\beta$  for each group, denoted by  $\beta^{(A)}$  and  $\beta^{(B)}$ . Previous studies have revealed the wide variety of behaviors that are possible for this type of system, depending on the value of  $\beta$  [62]. For this study, we have used a range of  $\beta$  from 0 to 10, with the experiments focusing on cases of  $\beta > 3$ , for which the system displays chaos (with some periodic windows) when the nodes are not coupled.

For each run of the experiment, the nodes are started from random initial conditions. This system has a time delay, so the initial condition will be a function of time over an interval. Thus, we allow the experiment to run with only random electrical activity at the input to the DSP in the absence of coupling and feedback for 1 second to provide the initial states for the nodes. After recording an initial condition, we enable feedback for 4 seconds, which is long enough for transients to disappear. At the end of this period, we enable coupling. Data are taken after transients have died out.

#### 4.4 Mathematical Model

The system of coupled feedback loops can be well-described by a mathematical model with a system of time delay differential equations for the voltages input to the MZMs  $x_i^{(m)} \in \mathbb{R}$  and the vectors describing the states of the filters  $\mathbf{u}_i^{(m)} \in \mathbb{R}^2$  [62]:

$$\dot{\mathbf{u}}_i^{(m)}(t) = \mathbf{E}\mathbf{u}_i^{(m)}(t) - \mathbf{F}\beta^{(m)} \cos^2[x_i^{(m)}(t - \tau) + \phi_0], \quad (4.1)$$

$$x_i^{(m)}(t) = \mathbf{G}\{\mathbf{u}_i^{(m)}(t) + \varepsilon \sum_j K_{ij}^{(m)} \mathbf{u}_j^{(m')}(t) - \mathbf{u}_i^{(m)}(t)\}, \quad (4.2)$$

where  $m$  and  $m' \neq m$  denote the groups A or B, and  $i$  indicates the node within a group.

$$\mathbf{E} = \begin{pmatrix} -(\omega_H + \omega_L) & -\omega_L \\ \omega_H & 0 \end{pmatrix}, \mathbf{F} = \begin{pmatrix} \omega_L \\ 0 \end{pmatrix}, \mathbf{G} = \begin{pmatrix} 1 & 0 \end{pmatrix} \quad (4.3)$$

are constant matrices that describe the filter. The filter parameters are chosen as  $\omega_L = 2\pi \cdot 2.5$  kHz and  $\omega_H = 2\pi \cdot 0.1$  kHz. For a bipartite network with no intra-group coupling, we define the inter-group coupling matrices  $\mathbf{K}^{(m)} = \{K_{ij}^{(m)}\}$ :

$$\mathbf{K} = \begin{pmatrix} 0 & \mathbf{K}^{(A)} \\ \mathbf{K}^{(B)} & 0 \end{pmatrix}, \quad (4.4)$$

where  $\mathbf{K}$  is the overall coupling matrix for the entire network. For the configuration shown in Fig. 4.1(a),  $i, j = 1, 2$ , and

$$\mathbf{K}^{(A)} = \mathbf{K}^{(B)} = \frac{1}{2} \begin{pmatrix} 1 & 1 \\ 1 & 1 \end{pmatrix} \quad (4.5)$$

so that

$$\mathbf{K} = \begin{pmatrix} 0 & \mathbf{K}^{(A)} \\ \mathbf{K}^{(B)} & 0 \end{pmatrix} = \frac{1}{2} \begin{pmatrix} 0 & 0 & 1 & 1 \\ 0 & 0 & 1 & 1 \\ 1 & 1 & 0 & 0 \\ 1 & 1 & 0 & 0 \end{pmatrix}. \quad (4.6)$$

Equations (4.1) and (4.2) can describe the dynamics of the uncoupled nodes if we set the coupling strength  $\varepsilon = 0$ , as the second term in Eq. (4.2) represents the diffusive coupling scheme.

Numerical simulations use a discrete-time implementation of these differential equations, as described in Ref. [62]. The simulations of uncoupled and coupled

systems are in excellent agreement with the experimental results for the variety of dynamical behaviors that can be observed.

## 4.5 Stability of Group Synchrony

We will now investigate the existence and stability of the group synchronous solution, i.e., we will derive analytical conditions determining whether such a solution (in which the two nodes of each group are identically and isochronously synchronized, but there is no identical synchrony between nodes of different groups) exists for given values of  $\beta^{(A)}$  and  $\beta^{(B)}$ , and if it does, if that solution is stable. We use the approach described in [2, 93]. The condition for the existence of the group synchronous solution for a particular coupling configuration is that

$$\sum_j K_{ij}^{(m)} = c^{(m)}; \quad m = \{A, B\}, \quad (4.7)$$

i.e., that the row sum of the matrices  $\mathbf{K}^{(m)}$  is uniform within each group. For the work reported here, we fix  $c^{(A)} = c^{(B)} = 1$ .

The group synchronized state for group  $m$  is governed by

$$\dot{\mathbf{u}}_s^{(m)}(t) = \mathbf{E}\mathbf{u}_s^{(m)}(t) - \mathbf{F}\beta^{(m)} \cos^2[x_s^{(m)}(t - \tau) + \phi_0], \quad (4.8)$$

$$x_s^{(m)}(t) = \mathbf{G}\{\mathbf{u}_s^{(m)}(t) + \varepsilon[\mathbf{u}_s^{(m')} (t) - \mathbf{u}_s^{(m)}(t)]\}. \quad (4.9)$$

Linearizing Eqs. (4.1) and (4.2) about the synchronous solution  $\mathbf{u}_s^{(m)}$  ( $m = A, B$ ), we obtain the master stability equations:

$$\begin{aligned} \delta\dot{\mathbf{u}}^{(m)}(t) = & \mathbf{E}\delta\mathbf{u}^{(m)}(t) - \mathbf{F}\beta^{(m)} \sin[2x_s^{(m)}(t - \tau) + 2\phi_0] \\ & \times \mathbf{G}[(1 - \varepsilon)\delta\mathbf{u}^{(m)}(t - \tau) + \varepsilon\gamma\mathbf{u}^{(m')}(t - \tau)]. \end{aligned} \quad (4.10)$$

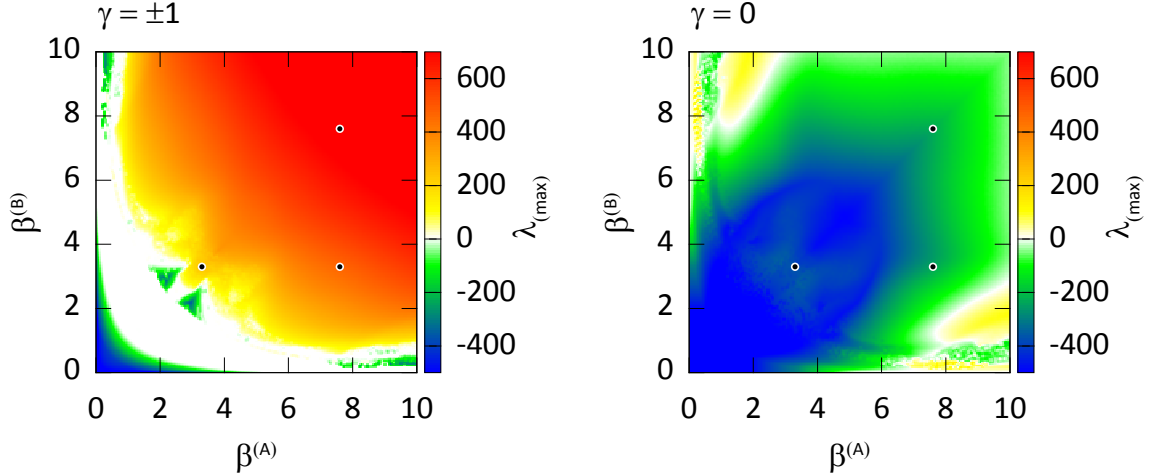


Figure 4.2: Maximum Lyapunov exponent  $\lambda_{\max}$  as a function of  $\beta^{(A)}$  and  $\beta^{(B)}$ : (a) in the longitudinal directions  $\gamma = \pm 1$ , (b) in the transverse direction  $\gamma = 0$ . White areas correspond to  $\lambda_{\max} = 0$ . Dots indicates values of  $\beta^{(A)}$  and  $\beta^{(B)}$  used in this experiment.

In Eq. (4.10),  $\gamma$  is a parameter that is chosen from the eigenvalue spectrum of  $\mathbf{K}$ .  $\gamma$  may be any of the eigenvalues of  $\mathbf{K}$ , but depending on the choice of  $\gamma$ , the Lyapunov exponent will give information about the stability of the solution in the longitudinal direction relative to the synchronous manifold, or in the direction transverse to the manifold. The largest Lyapunov exponent as a function of this parameter  $\gamma$  is called the Master Stability Function (MSF). For the configurations presented here, the nonzero eigenvalues of  $\mathbf{K}$  are 1 and -1, and any remaining eigenvalues are zeros. Therefore, the stability results will be identical for any two-group network whose nodes are described by Eqs. (4.1) and (4.2) and whose coupling matrix is in the form of (4.4), satisfies (4.7), and has identical rows for either  $\mathbf{K}^{(A)}$  or  $\mathbf{K}^{(B)}$  (for a proof, see section 4.8).

The eigenvalues  $\gamma = -1$  and  $\gamma = 1$  in the master stability equation (4.10) cor-

respond to perturbations parallel to the synchronization manifold. The corresponding value of the MSF determines the dynamical behavior inside the synchronization manifold and is shown in Fig. 4.2(a) in dependence on the parameters  $\beta^{(A)}$  and  $\beta^{(B)}$ . Negative, zero, and positive values of the MSF for  $\gamma = -1, 1$  denote fixed-point, periodic, and chaotic dynamics, respectively. Due to the inversion symmetry of the MSF for two-group synchronization [2, 93], the MSF values are identical for  $\gamma = -1$  and  $\gamma = 1$ .

Transverse stability of the synchronization manifold is determined by using the eigenvalue  $\gamma = 0$  in Eq. (4.10). Figure 4.2(b) shows the largest Lyapunov exponent in the transverse direction, which is negative for almost the entire range of  $\beta^{(A)}$  and  $\beta^{(B)}$  that is shown, indicating that we expect the group synchronous solution to be stable for most parameters.

## 4.6 Experimental Observations of Cluster Synchrony

To observe cluster synchrony, we require  $\beta^{(A)} = \beta^{(B)}$ . The coupling structure is shown in Fig. 4.1. We maintain the distinction between group A and group B by the coupling structure, so that there is no coupling between nodes of different groups. For cluster synchrony, even though the nodes are identical in equations and parameters, they will not identically synchronize. Rather, the nodes will synchronize in clusters, with identical synchrony between all the nodes in one cluster or group. In this case, the nodes  $A_1$  and  $A_2$  synchronize into one cluster, and the nodes  $B_1$  and  $B_2$  synchronize into the other cluster (see Fig. 4.1). Thus, the two nodes in

each cluster will identically synchronize, despite having no direct coupling between them.

To predict the stability of the cluster synchrony state for four identical oscillators with this coupling configuration, we look at the MSF plots of Fig. 4.2 on the plot diagonals, where  $\beta^{(A)} = \beta^{(B)}$ . Because cluster synchrony is a special case of group synchrony, when  $\lambda_{(max)} < 0$  in the transverse direction for  $\beta^{(A)} = \beta^{(B)}$ , cluster synchrony will be the stable solution. Two cases where we expect stable cluster synchrony are shown by dots on Fig. 4.2. For  $\beta^{(A)} = \beta^{(B)} = 3.3$  and for  $\beta^{(A)} = \beta^{(B)} = 7.6$ ,  $\lambda_{(max)} > 0$  in the longitudinal direction, indicating chaotic behavior, and  $\lambda_{(max)} < 0$  in the transverse direction, indicating stable cluster synchrony.

For  $\beta^{(A)} = \beta^{(B)} = 3.3$ , simulated and experimental time traces are shown in Fig. 4.3. For this value of  $\beta$ , all four nodes identically synchronize. Because identical synchrony is actually a special case of cluster synchrony, in which both clusters identically synchronize to each other, this is not unexpected.

For  $\beta^{(A)} = \beta^{(B)} = 7.6$ , simulated and experimental time traces are shown in Fig. 4.4. For this value of  $\beta$ , the four-node system displays cluster synchrony. The two nodes of group A are identically synchronized, and the two nodes of group B are identically synchronized, but the two groups are not identically synchronized, despite having identical parameters.

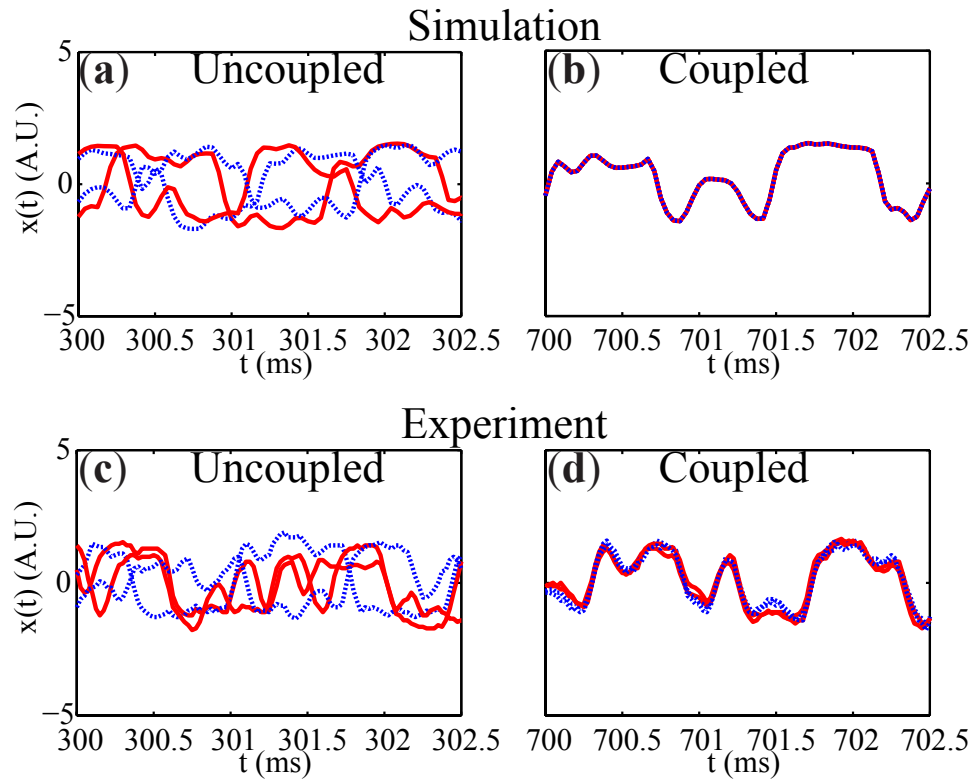


Figure 4.3: Time traces from simulation (upper) and experiment (lower) for  $\beta^{(A)} = \beta^{(B)} = 3.3$ . For these values, the coupled system (right) displays identical synchrony, a special case of cluster synchrony. The red (solid) traces correspond to the nodes in group A, and the blue (dashed) traces correspond to the nodes in group B, as shown in Fig. 4.1.

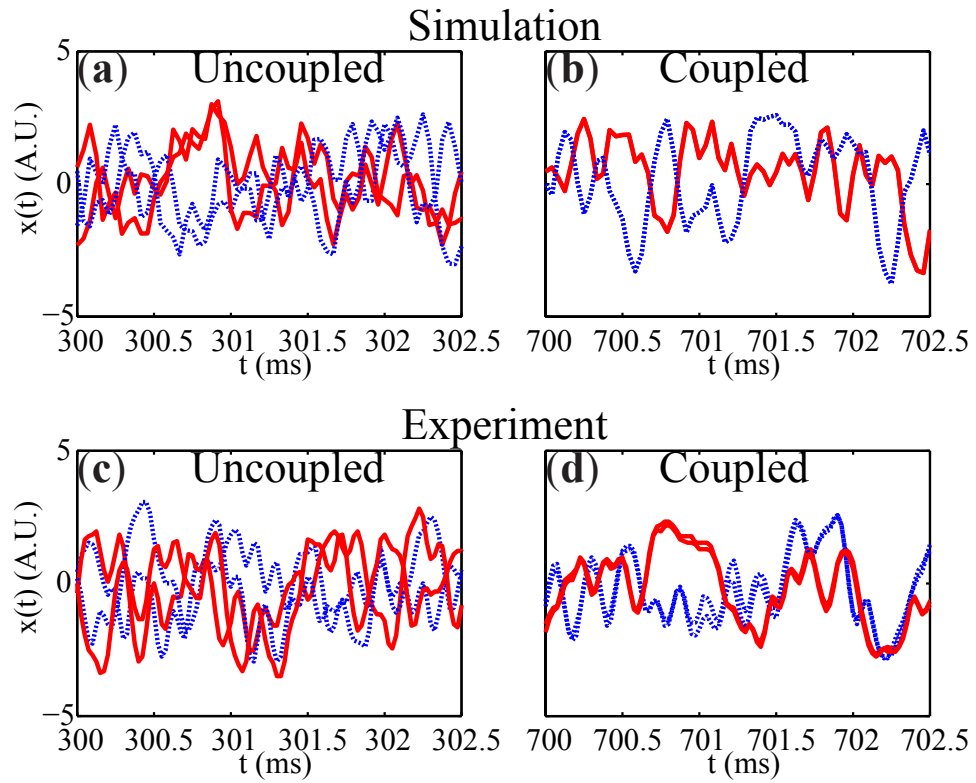


Figure 4.4: Time traces from simulation (upper) and experiment (lower) for  $\beta^{(A)} = \beta^{(B)} = 7.6$ . For these values, the coupled system (right) displays cluster synchrony, a special case of group synchrony. The red (solid) traces correspond to the nodes in group A, and the blue (dashed) traces correspond to the nodes in group B, as shown in Fig. 4.1.

## 4.7 Experimental Observations of Group Synchrony

To observe group synchrony in this system, we select dissimilar values of  $\beta^{(A)}$  and  $\beta^{(B)}$ , as shown by the black dots in Fig. 4.2. The global coupling strength is chosen as  $\varepsilon = 0.8$ . The experimental values for  $\beta^{(A)}$  and  $\beta^{(B)}$  were adjusted using the DSP board. The values of  $\beta^{(A)}$  and  $\beta^{(B)}$  used in simulation were established by varying the values close to the experimental values to find nearby values which match best the dynamical behavior of the experiments for uncoupled nodes, obtained from the shape of the reconstructed attractor in phase space (e.g., in terms of the attractors, Fig. 4.9). Since the values determined experimentally as  $\beta^{(A)} = 7.6$  and  $\beta^{(B)} = 3.3$  are subject to measurement uncertainties, it is not surprising that we find slightly different values in simulation, i.e.,  $\beta^{(A)} = 7.66$  and  $\beta^{(B)} = 3.28$ . The comparison of uncoupled and coupled time traces in experiment and simulation is shown in Fig. 4.5.

As can be seen in Fig. 4.5(a), the uncoupled nodes are completely unsynchronized. In both the experiment and simulation, the dynamics of the nodes in group B have a significantly smaller amplitude than those in group A, with qualitatively similar dynamics between simulation and experiment.

The differences between the uncoupled dynamics of the two groups can be further seen in Fig. 4.9(a), which shows the attractors of the experimental time traces of one node in group A and one node in group B. The attractors are generated with three-dimensional time-delay-embedding, with an embedding time of 0.05 ms. The 5 ms of experimental data used to generate the embeddings includes the 2.5 ms

of data that is shown in Fig. 4.9(a). In the uncoupled case, the amplitude of the attractor for group A (left, red) is much larger than that of group B (right, blue), and although we can see some structure in the attractor for group A, the attractor for group B has a much more open structure, reminiscent of quasi-periodicity.

Figure 4.7 shows experimental and simulated time traces of the coupled system. The simulated traces in Fig. 4.7(a) show the behavior of *any* two-group system displaying stable group synchrony according to Eqs. (4.8) and (4.9), with the parameters we have used here. Figure 4.7(b) shows experimental results for a system coupled according to Fig. 4.1(a). These time traces show that there is identical, isochronal synchrony between  $x_1^{(A)}$  and  $x_2^{(A)}$ , and between  $x_1^{(B)}$  and  $x_2^{(B)}$ , but not identical synchrony between the groups. Thus, this is an example of group synchrony. We also performed experiments on two asymmetric four-node configurations. These configurations were created by removing links from the original structure of Fig. 4.1(a), while preserving the constant row sum and eigenvalues (1, -1, 0, and 0) of  $\mathbf{K}$ , keeping all other parameters the same. Their topologies and dynamics are shown in Figs. 4.7(c) and 4.7(d). Because these schemes are also described by Fig. 4.2, they also display group synchrony. In the experimental time traces, there are slight differences between the two traces of one group, due to the intrinsic experimental noise and mismatch we expect in any real system. An example of a larger network that displays the same behavior is shown in Fig. 4.8.

The correlations between the two nodes in each group are shown in Fig. 4.9(c) for the selection of data that was used to construct the attractors in Fig. 4.9(b), which includes the data displayed in the time traces of Fig. 4.5(b). These correlations

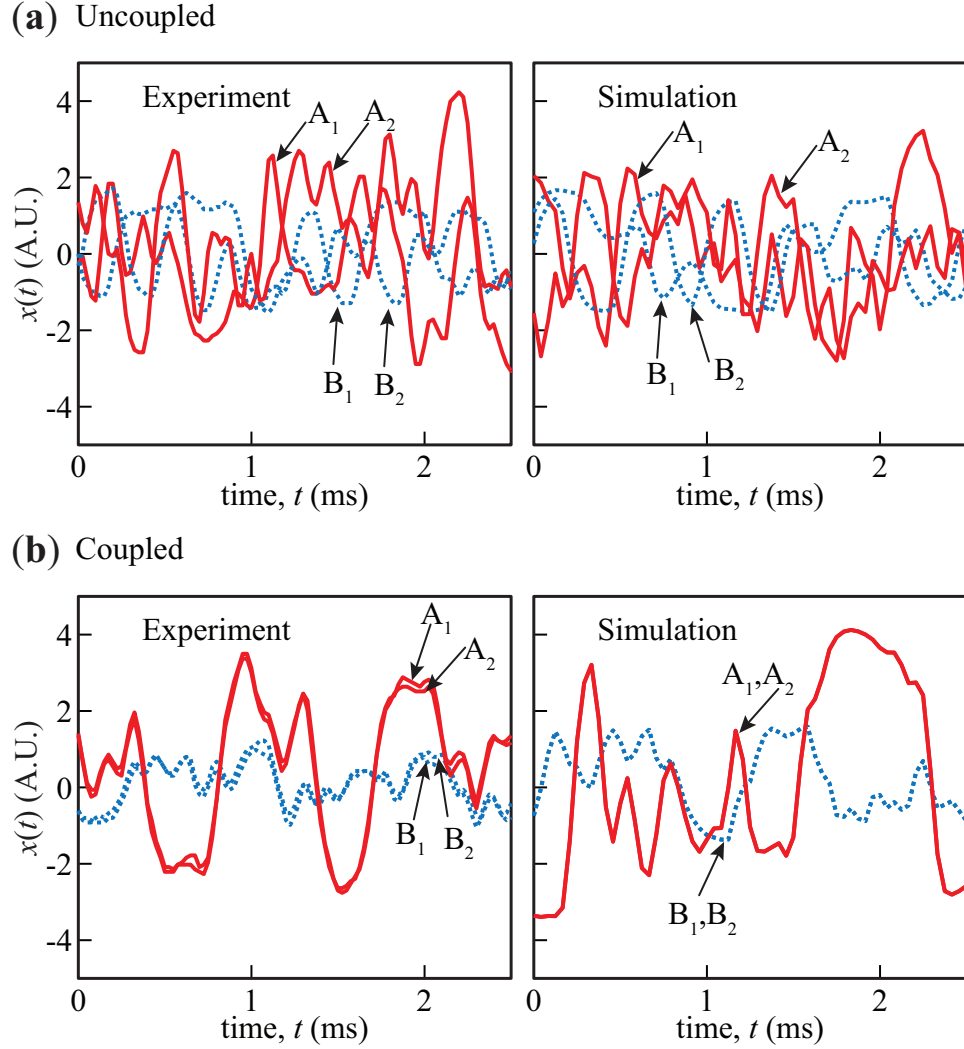


Figure 4.5: Comparison of time traces from experiment (left column) and simulation (right column). Nodes in group A (B) are indicated by the red and solid (blue and dashed) lines. (a) Nodes are uncoupled, and the uncoupled nodes are completely unsynchronized. (b) Nodes are coupled according to the configuration in Fig. 4.1(a). There is identical, isochronal synchrony between  $x_1^{(A)}$  and  $x_2^{(A)}$ , and between  $x_1^{(B)}$  and  $x_2^{(B)}$ , but not identical synchrony between the groups, so this is an example of group synchrony. In the simulation, the two traces in one group are exactly synchronized and are indistinguishable, as we expect from a simulation without noise or mismatch. In experiment, slight differences between synchronized traces arise from experimental noise and mismatch in the real experimental system. In both the experiment and simulation, the dynamics of the nodes in group B have a significantly smaller amplitude than those in group A, with qualitatively similar dynamics between simulation and experiment.

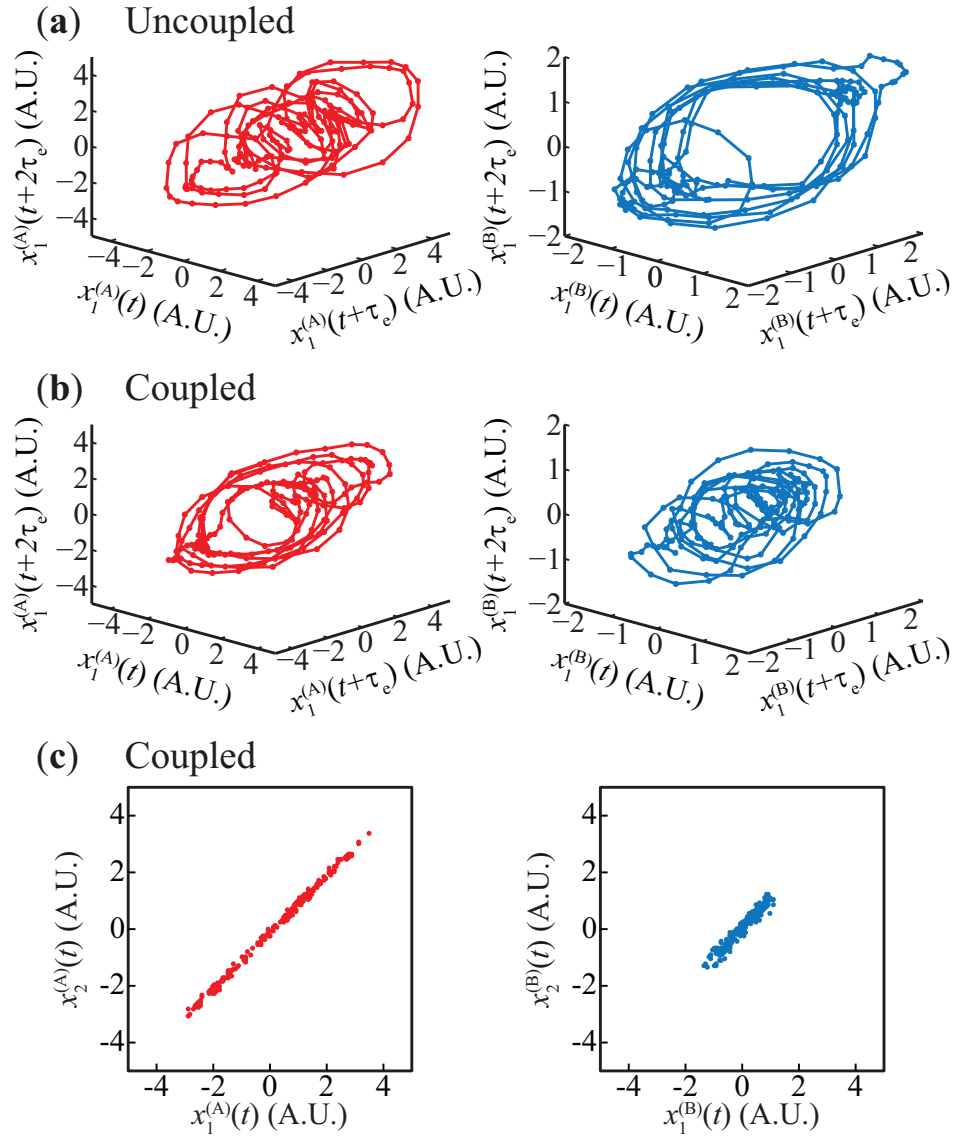


Figure 4.6: (a) and (b) Attractors reconstructed from 5 ms of experimental data, including that shown in Fig. 4.5, for the uncoupled and coupled dynamics, respectively. The embedding delay,  $\tau_e$ , is 0.05 ms. (c) Correlations between the nodes in each group. Group A data is shown in the left column (red) and group B data in the right column (blue).

show good identical and isochronal synchrony within each group.

The attractors of the two groups when they are coupled, shown in Fig. 4.6(b), are quite different from each other. However, we note some differences in the attractors of the coupled case (Fig. 4.6(b)) from the uncoupled case (Fig. 4.6(a)). The coupled attractor for group A (left, red) has decreased in size compared to the uncoupled case, and the center of the attractor has opened up, indicating that the dynamics are possibly less chaotic or have a more quasiperiodic component. The coupled attractor for group B (right, blue) has also decreased slightly in amplitude, but the coupled attractor is less open than the uncoupled attractor.

To further examine the nature of the synchrony of this system, we calculate the correlation functions of the experimental time traces, as shown in Fig. 4.9 for the topology shown in Fig. 4.1(a). For two variables  $y(t)$  and  $z(t)$ , which each have a mean of zero, we define the correlation function  $C$  as a function of time lag  $\Delta t$  [94]:

$$C(\Delta t) = \frac{\langle y(t)z(t + \Delta t) \rangle}{\sqrt{\langle y^2(t) \rangle \langle z^2(t) \rangle}}. \quad (4.11)$$

Figure 4.9(a) shows the autocorrelation functions for one node in each group when the nodes are uncoupled. The autocorrelation of  $x_1^{(A)}$  shows only a peak at zero time lag, which indicates chaotic dynamics, while the autocorrelation of  $x_1^{(B)}$  shows periodic dynamics, with correlation peaks at intervals of the time delay  $\tau = 1.4$  ms. In Fig. 4.9(b), we show the cross-correlation functions of  $x_1^{(A)}$  with  $x_2^{(A)}$ , and of  $x_1^{(B)}$  with  $x_2^{(B)}$  for the coupled system, which confirms identical, isochronal chaotic synchronization between the two nodes in a single group. Figure 4.9(c) shows the cross-correlation functions between two nodes in different groups, without and with

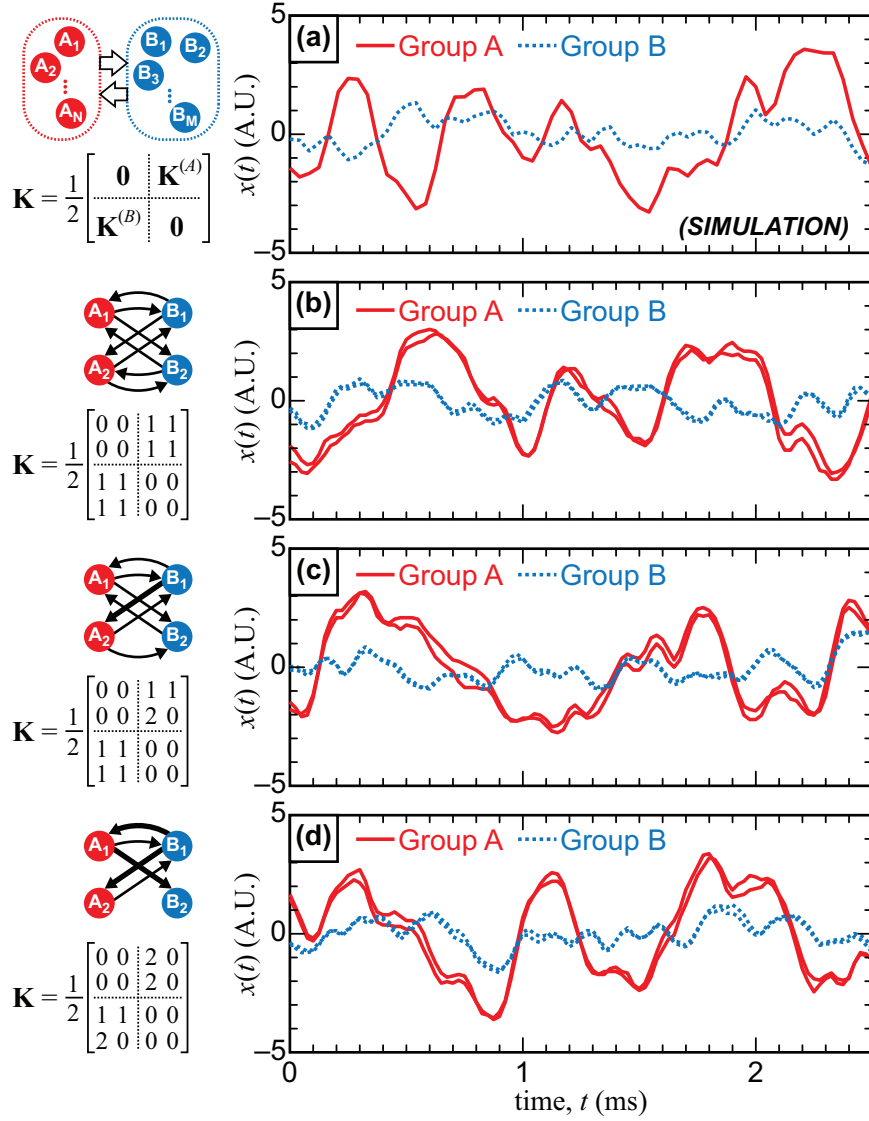


Figure 4.7: (a) Simulated motion in the synchronization manifold, obtained by numerically solving Eqs. (4.8) and (4.9), showing the predicted group-synchronous state. (b),(c),(d) Experimentally measured time traces from three different network configurations (indicated by the coupling scheme and the coupling matrices  $\mathbf{K}$ ) that achieve group synchrony. All three networks have the same eigenspectra, but the configuration in (b) is symmetric while those in (c) and (d) are not.

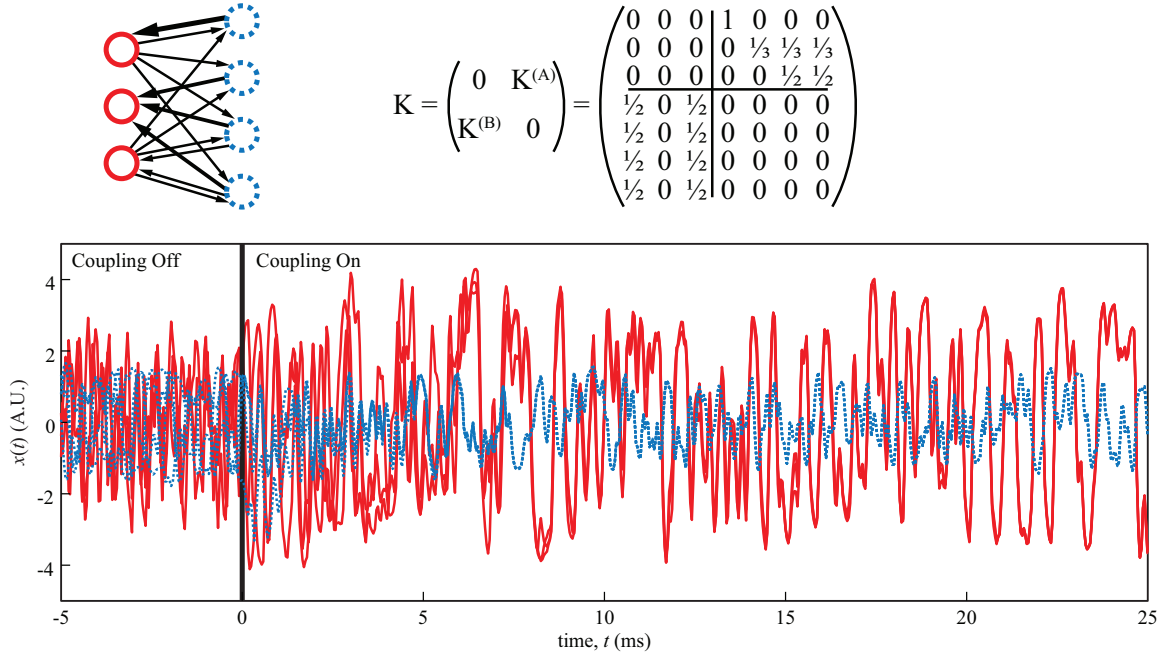


Figure 4.8: Simulation of a seven node network displaying group synchrony. The coupling scheme and the associated coupling matrix are shown above the simulated time traces. The parameters are the same as those presented in the letter. Coupling is enabled at time  $t = 0$ , and the nodes become group synchronized so that all three red, solid lines of Group A are identically synchronized, and all four blue, dashed traces of Group B are identically synchronized. Note that the coupling matrix for the specific network configuration shown here satisfies Eq. (4.12b). Hence, the coupling matrix has eigenvalues -1, 1, and degenerate zeros. The stability of the group synchronous solution of this system is described by Fig. 4.2(b). The dynamics of the seven node, group synchronized system, are predicted by Fig. 4.2(a), as illustrated by Fig. 4.7(a).

coupling. The uncoupled case has no correlation, as we expect, but the coupled case has a high correlation peak at a lag of  $\Delta t = -1.4$  ms. From this, we can see that there is time-lagged phase synchrony between the two groups, with the dynamics of group B leading the dynamics of group A by the system delay,  $\tau$ . However, the amplitudes of fluctuations of the two groups are still different after coupling, so there is no complete synchronization, and we have an interesting situation of the simultaneous coexistence of intragroup isochronal identical synchrony and time-lagged phase synchrony between the groups.

## 4.8 Extension of Group Synchrony Results to Different Coupling Configurations

Figures 4.7(b), (c), and (d) show that stable group synchrony is experimentally observed for three different coupling configurations. However, our stability analysis and the numerical computations in Fig. 4.2 apply to all of these coupling schemes and, more generally, to a whole class of networks, characterized by an arbitrary number of nodes in both the groups  $A$  and  $B$  [95].

We define  $N_A$  and  $N_B$  the number of nodes in group  $A$  and  $B$ , respectively. Then the couplings are fully described by the  $N_A \times N_B$  coupling matrix  $\mathbf{K}^{(A)}$ , whose entries  $\{K_{ij}^{(A)}\}$  represent the intensity of the direct interaction from system  $j$  in group  $B$  to  $i$  in group  $A$  and the  $N_B \times N_A$  matrix  $\mathbf{K}^{(B)}$ , whose entries  $\{K_{ij}^{(B)}\}$  represent the intensity of the direct interaction from system  $i$  in group  $A$  to  $j$  in group  $B$ .

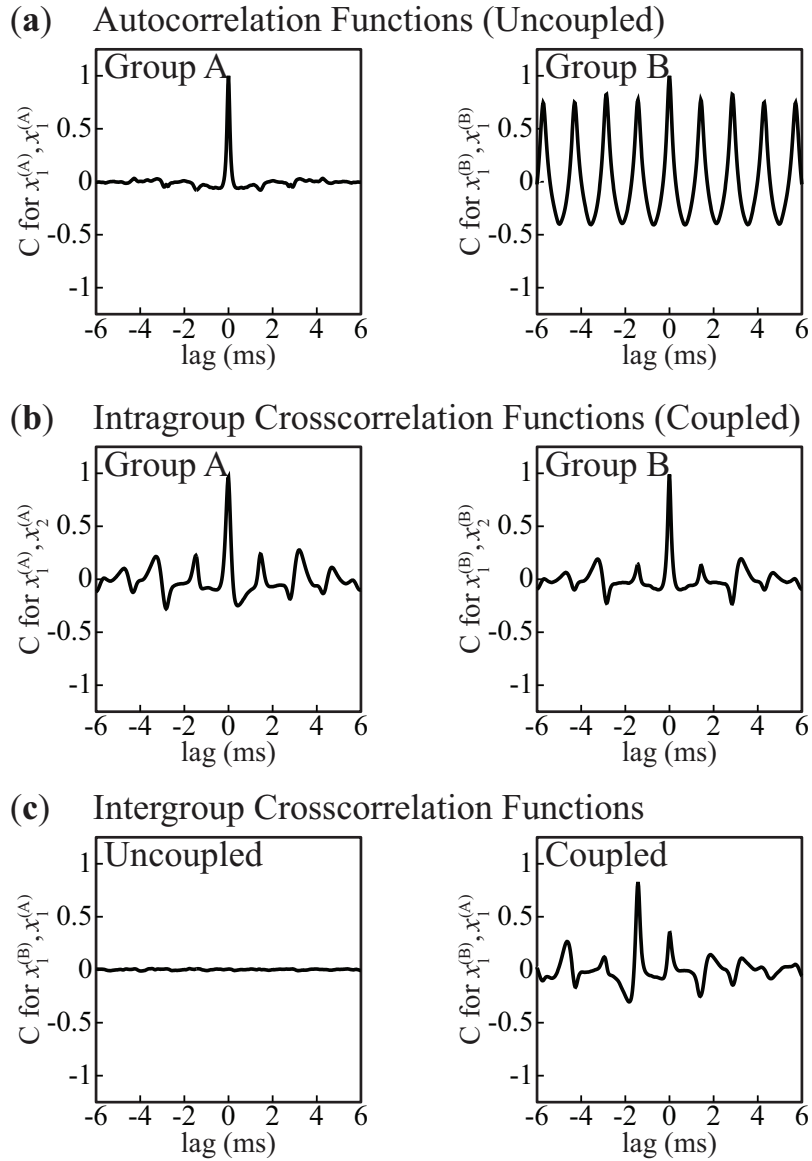


Figure 4.9: Correlation functions of 3.9 s of experimental data. (a) Autocorrelation functions for the dynamics of group A (left) and group B (right), with no coupling in the system. (b) Cross-correlation functions between the two nodes in group A (left) and group B (right), for coupled nodes. (c) Cross-correlation functions between one node in group A and one node in group B for the uncoupled system (left) and coupled system (right).

These matrices  $\mathbf{K}^{(A)}$  and  $\mathbf{K}^{(B)}$  can be combined with eq. (4.4) to give the full coupling matrix. We assume that each row of  $\mathbf{K}$  sums to one (i.e.  $c^{(A)} = c^{(B)} = 1$  from Eq. (4.7)), and one of the following conditions is held:

$$\mathbf{K}^{(A)} = \begin{pmatrix} a \\ a \\ \dots \\ a \end{pmatrix}, \quad (4.12a)$$

$$\mathbf{K}^{(B)} = \begin{pmatrix} b \\ b \\ \dots \\ b \end{pmatrix}, \quad (4.12b)$$

where  $a$  ( $b$ ) is any  $N_B$ -dimensional row-vector ( $N_A$ -dimensional row-vector) with its entries summing to one. As long as one of these conditions is held, the eigenvalues of the matrix  $K$  are

$$\Lambda = [0, 0, \dots, 0] \cup [-1, 1], \quad (4.13)$$

where here  $[0, 0, \dots, 0]$  denotes  $|N_A + N_B - 2|$  zeros. As derived in [95], the group synchronous solution for any network that satisfies either Eqs. (4.12a) or (4.12b) is described by the plot in Fig. 4.2(b).

## 4.9 Conclusions

In conclusion, we have examined a four-node system of nonlinear optoelectronic oscillators in the case where there are two groups of nodes with dissimilar

parameters. Our experiments display the phenomenon of group synchronization, and we analyze the stability of the group synchronized solutions for chaotic dynamical states. It is remarkable that, although the coupling is entirely between the different groups and not within the groups, identical isochronal synchronization within each group is induced by this coupling, while the two groups are not mutually amplitude synchronized, as predicted by our stability analysis using the generalized master stability function [2, 93]. Thus the nodes of group B act as a kind of dynamical relay [96] for the nodes of group A, and vice versa. These results have been experimentally demonstrated with three coupling configurations, and conditions for observing group synchrony in other networks have been discussed.

Our observations go beyond previous work on sublattice and cluster synchrony, where the experiments focused on optical phase synchronization for coupled lasers without self-feedback [84, 85]. Group synchronization in larger networks is a significant challenge for future experimental investigation.

## Chapter 5: Varying Coupling Delay to Produce Different Synchronization States

*This chapter is based on work from the following paper: Synchronization States and Multistability in a Ring of Periodic Oscillators: Experimentally Variable Coupling Delays, C. R. S. Williams, F. Sorrentino, T. E. Murphy, and R. Roy, Manuscript submitted to Chaos (2013).*

### 5.1 Overview

We experimentally study the complex dynamics of a unidirectionally coupled ring of four identical optoelectronic oscillators. The coupling between these systems is time-delayed in the experiment and can be varied over a wide range of delays. We observe that as the coupling delay is varied, the system may show different synchronization states, including complete isochronal synchrony, cluster synchrony, and two splay-phase states. We analyze the stability of these solutions through a master stability function approach, which we show can be effectively applied to all the different states observed in the experiment. Our analysis supports the experimentally observed multistability in the system.

Synchronization between delay-coupled oscillators has many applications in

biological and technological contexts. In the specific configuration of periodic oscillators connected in a unidirectional ring, changing the coupling time delays can lead to different synchronization relationships between the oscillators. In this paper we present an experiment of four oscillators coupled in a unidirectional ring, with coupling delays that can be changed to observe different synchronization states.

## 5.2 Introduction

Synchronization between coupled oscillators is of interest to numerous areas of research. In particular, understanding the phase relationship between synchronized oscillators could have applications to coupled neurons in the brain, where synchronization can play a role in neurological disorders. Prasad and his colleagues observed a phase-flip bifurcation, or a transition from in-phase synchrony to out-of-phase synchrony as the coupling delay between two oscillators is increased, both in simulations and in an electronic circuit [97]. Adhikari and his collaborators observed similar transitions for neuron models, including larger numbers of coupled nodes [4]. There are other examples in nature and applications in technology where the role of synchronization patterns between clock signals is important. For example, specific rhythmic patterns of neural activity generated by groups of neurons which go by the name of *central pattern generators* are known to regulate complex coordinated tasks such as locomotion and respiration [98–100]. In particular, a unidirectional ring of four coupled oscillators can act as a central pattern generator to produce different gait types in quadrupeds [5].

Previous work has focused on rings of unidirectionally coupled Stuart-Landau oscillators [101–103], both in the absence and in the presence of delays. Choe *et al.* have theoretically considered and numerically simulated systems of delay coupled oscillators, and have shown the ability to control the presence of different synchronization states as the coupling delay is changed [104]. Other papers have focused on unidirectional rings of coupled chaotic oscillators and found that due to the ring structure, chaos may be suppressed in favor of periodic solutions [105–108]. Experimental circuital realizations of unidirectional rings of coupled Lorenz systems were studied in [106, 109]. However in Refs. [106, 109], coupling delays were not considered.

Here, we present an experiment of coupled optoelectronic oscillators configured so that the coupling delays can be easily varied. By changing the coupling delays, we observe different synchronization states. The network topology, shown in Fig. 5.1(a), is composed of four oscillators, each with its own feedback delay  $\tau_f$ . This feedback creates dynamics in each oscillator, even when they are uncoupled from the other nodes. The four oscillators are delay-coupled together in a unidirectional ring. Each coupling link has delay  $\tau_c$ , and here we restrict ourselves to the case where  $\tau_c \geq \tau_f$ . For different values of  $\tau_c$ , we observe different behaviors of this system, and for some parameter values, we see different behaviors that are dependent on initial conditions, or a multistability of two or more behaviors. We can use a master stability function (MSF) analysis [80] to evaluate the stability of the observed behaviors.

### 5.3 Experiment

The experimental setup of a single optoelectronic oscillator is shown in Fig. 5.1(b). In Fig. 5.1(b) the red lines indicate an optical signal, and the black lines indicate an electronic signal. The coupling delay  $\tau_c$  is varied by discrete steps by programming the digital signal processing (DSP) board, and  $\tau_f$  remains fixed. For each measurement, the system always starts with both the feedback and coupling disabled, so that only noise is present. Then feedback is enabled, followed by the coupling.

The system is well-modeled by a system of coupled time-delay differential equations [62]:

$$\dot{\mathbf{u}}_i(t) = \mathbf{E}\mathbf{u}_i(t) - \mathbf{F}\beta \cos^2(x_i(t - \tau_f) + \phi_0), \quad (5.1)$$

$$x_i(t) = \mathbf{G}\{\mathbf{u}_i(t) + \varepsilon \sum_j K_{ij}[\mathbf{u}_j(t - \tau_c + \tau_f) - \mathbf{u}_i(t)]\}, \quad (5.2)$$

for oscillators  $i = 1, \dots, N$ , where  $x_i \in \mathbb{R}$  are the voltages input to the MZMs and  $\mathbf{u}_i \in \mathbb{R}^2$  are the vectors describing the states of the filters. For our ring of four nodes,  $N = 4$ . The filter is described by constant matrices

$$\mathbf{E} = \begin{pmatrix} -(\omega_H + \omega_L) & -\omega_L \\ \omega_H & 0 \end{pmatrix}, \mathbf{F} = \begin{pmatrix} \omega_L \\ 0 \end{pmatrix}, \text{ and } \mathbf{G} = (1 \ 0), \quad (5.3)$$

and the filter parameters are chosen as  $\omega_L = 2\pi \times 2.5$  kHz and  $\omega_H = 2\pi \times 0.1$  kHz.

The adjacency matrix for a unidirectional ring is given by

$$\mathbf{K} = \begin{pmatrix} 0 & 0 & 0 & 1 \\ 1 & 0 & 0 & 0 \\ 0 & 1 & 0 & 0 \\ 0 & 0 & 1 & 0 \end{pmatrix}. \quad (5.4)$$

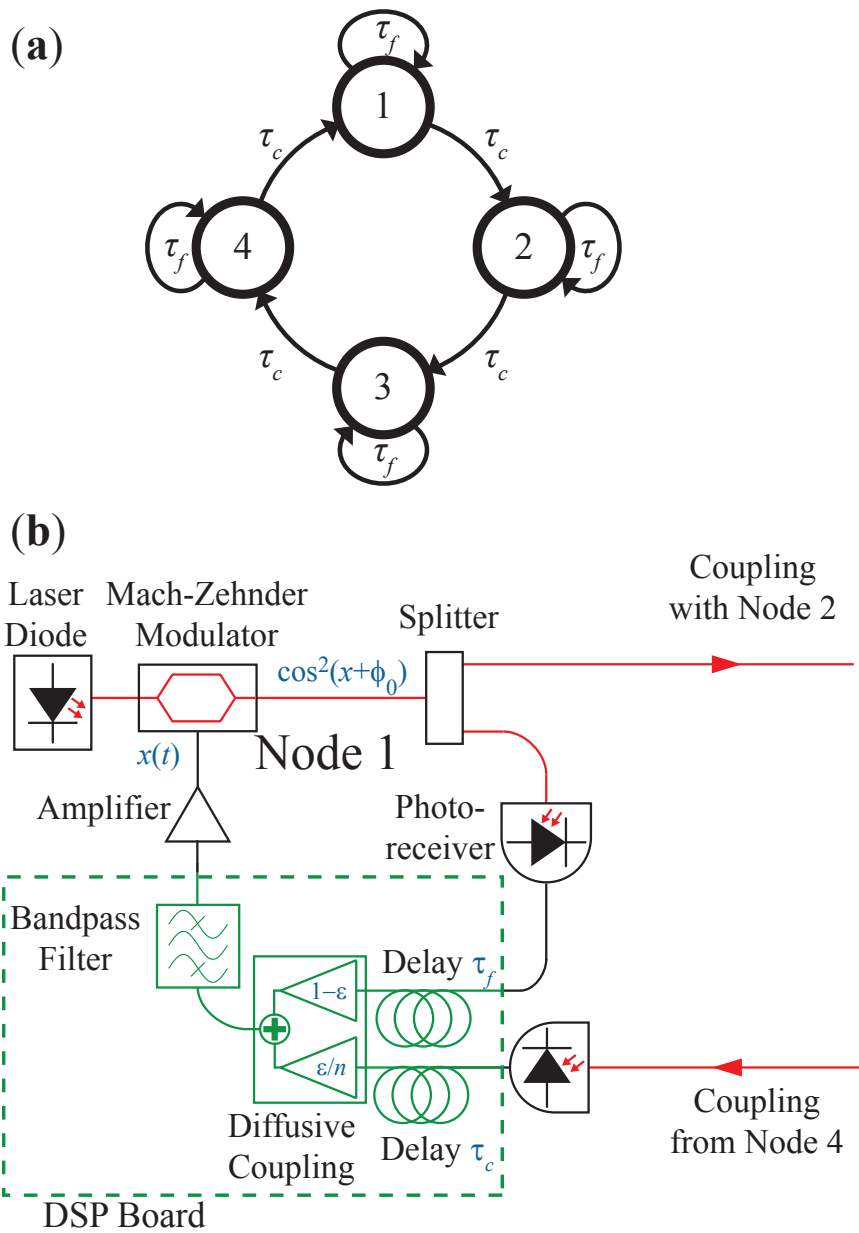


Figure 5.1: (a) Schematic of four nodes connected in a unidirectional ring. (b) Experimental setup for a single node, an optoelectronic, non-linear oscillator, with time-delayed feedback.

The coupling strength is  $\varepsilon = 0.2$ , the modulator bias is  $\phi_0 = \pi/4$ , and the feedback strength is  $\beta = 1.21$ . The feedback delay is fixed at  $\tau_f = 1.4$  ms. All parameters are identical for the four nodes. The feedback strength ( $\beta$ ) and feedback delay ( $\tau_f$ ) were chosen so that, when uncoupled ( $\varepsilon = 0$ ), each node in the network would oscillate periodically.

We vary the value of  $\tau_c$  and observe the relative phases between the oscillators. As the coupling delay increases from  $\tau_c = \tau_f$ , we observe in each measurement one of four distinct synchronization states between the four coupled oscillators, as shown in Fig. 5.2. We can categorize these states by the relative phase  $\delta_k$  between successive oscillators. These states can also be described as *isochronal synchrony* (state  $S_0$ ,  $\delta_0 = 0$ ), *splay-phase synchrony*, (state  $S_1$  or state  $S_3$ ,  $\delta_1 = \pi/2$  or  $\delta_3 = 3\pi/2$ ) and *cluster synchrony* (state  $S_2$ ,  $\delta_2 = \pi$ ), which have been described and observed in this and other systems [2, 3, 93, 104]. At some values of the coupling delays, bistability is observed between pairs of these synchronization states. For longer coupling delays, we also see multistability between three or all four of these states. Note that in the case of multistability, the phase relationship is determined by the initial conditions, and once the four-node system has established a particular phase relationship after a transient period, the relative phases are maintained. While the time traces shown in Fig. 5.2 are for the coupled oscillators, they all resemble the time evolution of an uncoupled (isolated) system.

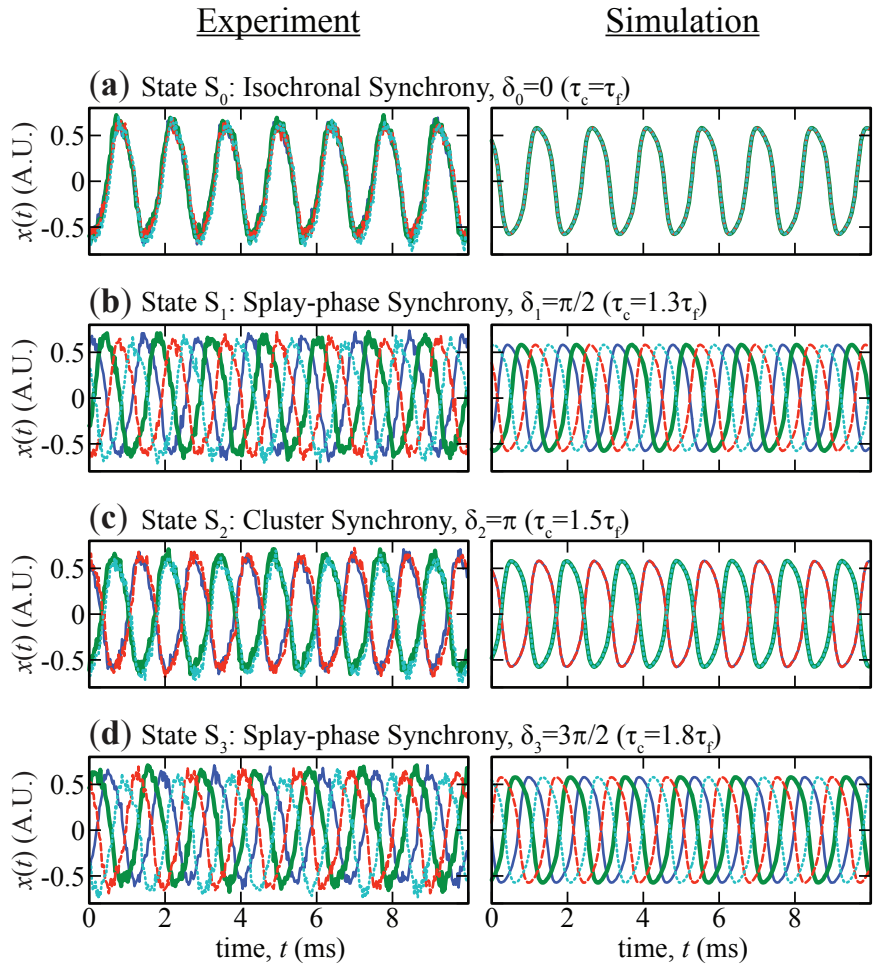


Figure 5.2: Representative time traces for four different values of the coupling delay, each displaying a different phase relationship between the four nodes, as denoted by  $\delta_k$ , the phase shift between successive oscillators in state  $S_k$ . Experimental traces are on the left, simulations on the right.

## 5.4 Stability Predictions

Representative time traces for four different values of the coupling delay, each displaying a different phase relationship between the four nodes, as denoted by  $\delta_k$ , the phase shift between successive oscillators in state  $S_k$ . Experimental traces are on the left, simulations on the right.

## 5.5 Results and Discussion

For each coupling delay  $1.4 \text{ ms} < \tau_c < 3 \text{ ms}$ , we performed 10 independent experiments and 2000 simulations, each starting from random initial conditions and observed how frequently each synchronization state occurred. The results are shown in Fig. 5.4. As the time delay  $\tau_c$  is increased, the observed phase lag  $\delta$  between successive oscillators increases in a step-like manner, separated by regions of bistability in which the system could fall into one of two possible stable synchronization patterns. For the coupling delay range shown in this figure, only one or two different phase relationships were observed for each value of the coupling delay, with good agreement between experiment and simulation. For the values of  $\tau_c$  for which a particular phase relationship synchronization state has a negative MSF, we see the corresponding synchronization state displayed in simulation and experiment. If, for a particular value of  $\tau_c$ , more than one phase relationship is stable, we see the corresponding two or three synchronization states in simulation and experiment. The particular state that is present depends on the initial conditions.

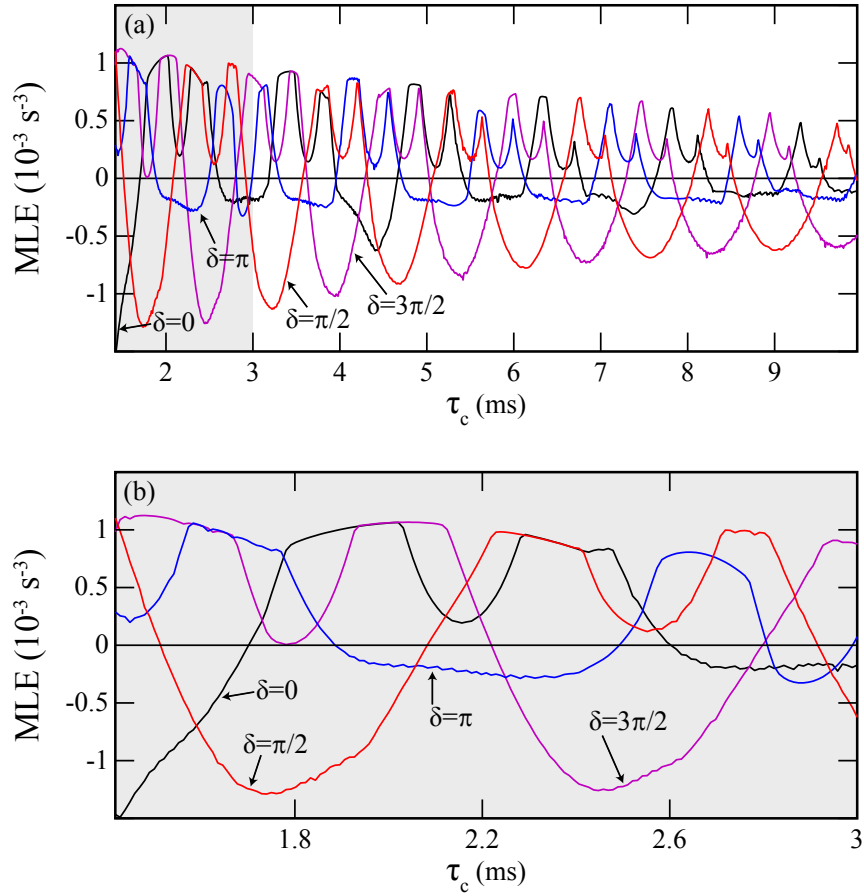


Figure 5.3: Master stability function of four different synchronization states:  $\delta_0 = 0$  (isochronal synchrony),  $\delta_1 = \pi/2$  or  $\delta_3 = 3\pi/2$  (splay phase synchrony), and  $\delta_2 = \pi$  (cluster synchrony). A negative MLE indicates the stability of a particular phase relationship. (a) MSF as a function of coupling delay  $\tau_c$  calculated over a wide range of delays. (b) Enlargement of (a) for narrow range of  $\tau_c$ .

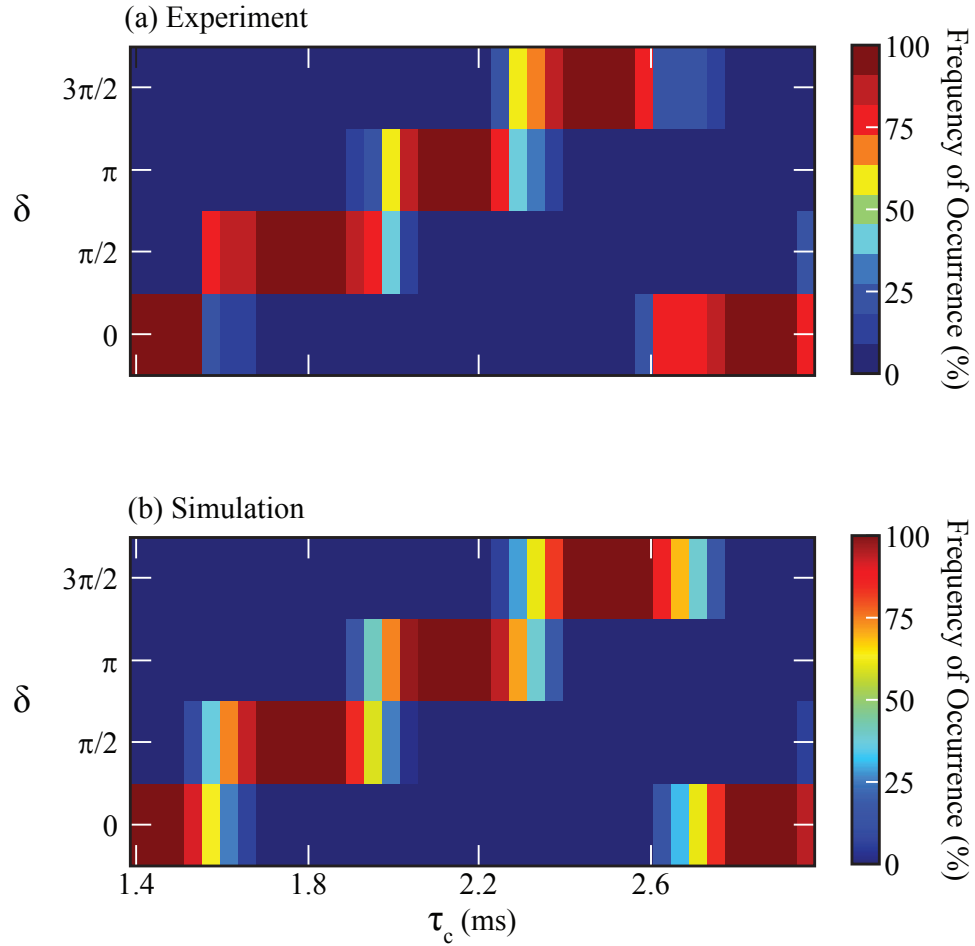


Figure 5.4: The phase relationships present as a function of coupling delay. For each coupling delay, the percentage of different random initial conditions resulting in a particular phase relationship is shown by the color scale. The top plot is the experimental results, with 10 different initial conditions for each delay. The bottom figure is simulations results, with 2000 different initial conditions for each delay.

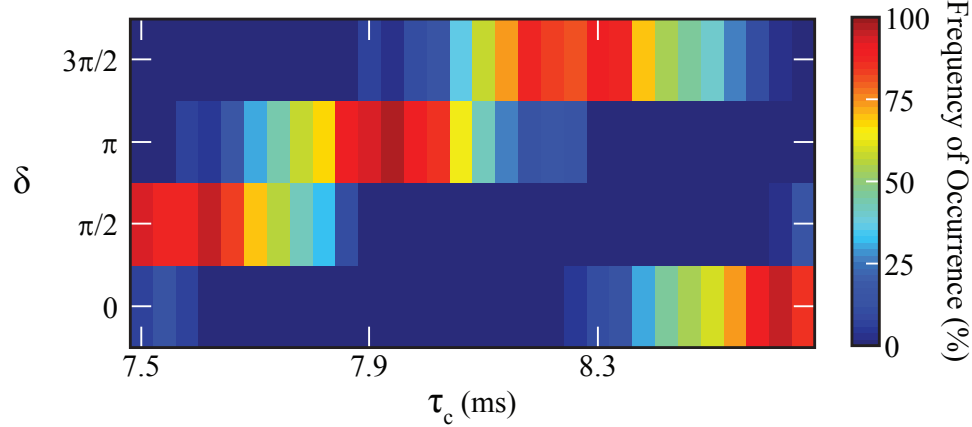


Figure 5.5: Multistability between synchronization states for long coupling delays, as observed for 50 different initial conditions in simulations. For each coupling delay, the percentage of different random initial conditions resulting in a particular phase relationship is shown by the color scale.

For longer coupling delays, near  $\tau_c = 8$  ms, the results from simulations are shown in Fig. 5.5, where there can be three different relationships shown, as we expect from the MSF calculations shown in Fig. 5.3(a). In the experiment, we also observe multistability between three synchronization states for larger values of  $\tau_c$ .

A comparison of Figs. 5.3(b) and 5.4 show good agreement between simulation, experiment, and calculated stability. The observations of particular phase relationships in experiment and simulation correspond well to the regions where the MSF predicts stability for those different phase relationships. For  $\tau_c$  slightly less than 3 ms, the stability calculation predicts that the cluster synchrony solution ( $\delta = \pi$ ) is stable, but this behavior is not observed in the experiment nor simulation. This is because the MSF calculation refers to local stability about a given state and does not guarantee that a solution can be easily reached from random initial conditions.

It is possible that given precise initial conditions, the system could be placed in a basin of attraction for this synchronous state, but cannot be seen from the random initial conditions we use.

We have observed a transition from in-phase, isochronal synchrony to splay-phase synchrony as we change the coupling delay to values larger than the internal delay. We have further observed three additional transitions - splay-phase→cluster, cluster→ splay-phase, splay-phase→isochronal - as the coupling delay is increased to twice the feedback delay, and the transitions appear to be cyclic as the coupling delay is further increased. The transitions are not sharp; for intermediate ranges of coupling delays, bistability is sometimes observed. This phenomenon was also observed in simulations of a unidirectional ring of coupled Stuart-Landau oscillators [104].

While multiple patterns of synchronization can occur in a unidirectional ring with symmetric coupling, real systems may have asymmetric or inhomogeneous delays between elements. The propagation time for a signal in the nervous system, for example, can be different for each link. Two recent papers investigate the synchronization patterns that occur in a unidirectional ring of oscillators or modeled neurons, both for homogeneous delays and for inhomogeneous delays [110,111]. By changing the coupling delays so that they are not all equal, a variety of synchronization states can be created, and the state is determined by the values of the coupling delays.

While our investigation focused on the case of four equal coupling delays, we also experimentally and numerically investigated the case where the coupling delays

are not identical, i.e.  $\tau_c^{(i)}$  is the coupling delay of the signal coming into node  $i$ , and  $\tau_c^{(1)}$ ,  $\tau_c^{(2)}$ ,  $\tau_c^{(3)}$ , and  $\tau_c^{(4)}$  can be varied independently. In this investigation, we focused on the case where the average coupling delay  $\bar{\tau}_c = (1/4) \sum_i \tau_c^{(i)}$  corresponds to the value of  $\tau_c$  for which isochronal synchrony is stable in the case of four equal coupling delays. If that is the case, we can write the solutions as time-shifted copies of each other, with time shifts that correspond to the differences of the coupling delays.

We considered two scenarios of asymmetric coupling delays. In the first, the total round trip time (or equivalently, the average coupling delay) was held constant, while one of the coupling delays was decreased, and another was increased. In the other case, three of the coupling delays were held fixed, while the fourth was varied. In both cases, we could predict the phase relationship between the dynamics of the four nodes by considering the geometry of the coupling delays and using simple algebraic equations.

## 5.6 Conclusion

In conclusion, we have presented an experiment of four optoelectronic oscillators coupled in a unidirectional ring, in which the coupling delays can be varied. We have observed four different synchronization states as the coupling delay is varied, including isochronal synchrony, cluster synchrony, and splay phase synchrony. We have compared our experimental results with simulations and numerical stability computations using a master stability function approach.

## Chapter 6: Conclusions and Future Work

In summary, we have studied two different experimental systems: an optical system to generate random numbers, and an optoelectronic network of four feedback loops used to study synchronization between dynamical systems.

In the first, we have constructed a fiber optic system that generates a sequence of random bits at a bit rate of 12.5 Gbit/s. This is the first physical RNG whose source for a random signal is quantum mechanical noise from amplified spontaneous emission in a fiber amplifier. The optical signal is detected using threshold detection to generate a binary sequence, and a time-delayed XOR is performed on the binary sequence in order to reduce correlations to an acceptable level. The quality of the resultant bit sequence is verified by passing the NIST and Diehard test suites, which are the standard industry evaluations for cryptographically secure random bit sequences.

The area of random number generation, particularly physical RNGs, continues to be an area research with interesting questions and new developments. One recent advance in optical noise-based RNGs was reported by Li, *et al.*, who generated two parallel, independent streams of random bits from a single optical source, a superluminescent LED, increasing the overall rate of bit generation to 20 Gb/s [112].

While the work presented in Chapter 2 and reported in [112] is based only on a quantum-mechanical noise source, much recent work in the field has focused on chaotic lasers or laser systems with feedback [113–116], including the development of on-chip laser-based RNG devices [117]. In these systems, the chaotic nature of the system relies on the presence of quantum-mechanical optical noise, which is amplified by or mixed with chaotic dynamics, in order to generate non-deterministic random bit sequences. In 2012, Mikami, et al. described a method for understanding the entropy of a bit sequence generated from a chaotic laser with noise [113]. Secure key distribution is an important application of RNGs, particularly optical methods, and in 2012, Yoshimura, et al. demonstrated a method of secure key distribution, enabled by driving two semiconductor lasers into synchrony by injecting them with a common, random optical signal [116]. Another recent study reports a method of generating random bits by combining a source of spontaneous emission noise with a bistable ring laser [118]. The relationship between the chaotic dynamics and the quantum-mechanical noise and the generation of random bits is still a topic to be explored. Particularly, is there a way to understand the contribution of the quantum mechanical noise in the system to the randomness of the signal, compared to the contribution of the chaotic or deterministic dynamics? An experimental system that could generate both limits of purely quantum mechanical noise and highly deterministic chaos, while adjusting the amount of noise or determinism, would provide an opportunity to analyze the relationship between the two types of dynamics, and their uses for RNG.

The second experimental system is a small network of four time-delay coupled

oscillators. Each oscillator is an optoelectronic feedback loop consisting of commercially available fiber optic and electronic components. A single loop can generate a range of dynamics, including periodic and chaotic, depending on the parameters of the system. When coupled, the dynamics of the feedback loops can synchronize into a variety of patterns. We have reported the first experimental observations of group synchrony between chaotic oscillators, in which the oscillators in the network are grouped by different parameters. When coupled together, the oscillators in the same group identically synchronize, even when they are not connected to one another. We have also presented a new experimental realization of periodic oscillators coupled in a unidirectional ring, varying the coupling delay. As the coupling delay is changed, the oscillators display different synchronization states: isochronal, splay-phase, and cluster synchrony. We have modeled this experimental system, and compare the numerical and experimental results with theoretical predictions for synchrony, which are in good agreement.

This experimental system of four optoelectronic oscillators has great potential for future research. By using programmable circuitry (DSP or FPGA boards), nearly all of the parameters can be varied independently and the network connectivity structure can be easily changed, allowing for tremendous flexibility in the experiments that can be performed. The ring configuration in particular is one that has many interesting questions to be answered. While some initial study of asymmetric coupling delays has been performed elsewhere analytically and numerically [110, 111], and initially experimentally, as reported here in Chapter 5, a more thorough experimental study of asymmetric time delays would be a straightforward

next step. Another interesting extension of the unidirectional ring configuration would be to study a unidirectional ring of oscillators that are tuned to have chaotic dynamics.

## Bibliography

- [1] Caitlin R. S. Williams, Julia C. Salevan, Xiaowen Li, Rajarshi Roy, and Thomas E. Murphy. Fast physical random number generator using amplified spontaneous emission. *Opt. Express*, 18(23):23584–23597, Nov 2010.
- [2] Francesco Sorrentino and Edward Ott. Network synchronization of groups. *Phys. Rev. E*, 76:056114, Nov 2007.
- [3] Caitlin R. S. Williams, Thomas E. Murphy, Rajarshi Roy, Francesco Sorrentino, Thomas Dahms, and Ekehard Schöll. Experimental observations of group synchrony in a system of chaotic optoelectronic oscillators. *Phys. Rev. Lett.*, 110:064104, Feb 2013.
- [4] Bhim Mani Adhikari, Awadhesh Prasad, and Mukeshwar Dhamala. Time-delay-induced phase-transition to synchrony in coupled bursting neurons. *Chaos: An Interdisciplinary Journal of Nonlinear Science*, 21(2):023116, 2011.
- [5] J.J. Collins and S.A. Richmond. Hard-wired central pattern generators for quadrupedal locomotion. *Biological Cybernetics*, 71(5):375–385, 1994.
- [6] Caitlin R. S. Williams, Francesco Sorrentino, Thomas E. Murphy, and Rajarshi Roy. Synchronization states and multistability in a ring of periodic oscillators: Experimentally variable coupling delays. Manuscript submitted to *Chaos*, 2013.
- [7] Edward N. Lorenz. Deterministic nonperiodic flow. *J. Atmos. Sci.*, 20:130–141, 1963.
- [8] Catherine Kyrtsov and Walter C. Labys. Evidence for chaotic dependence between US inflation and commodity prices. *Journal of Macroeconomics*, 28(1):256 – 266, 2006.
- [9] Rui Dilo and Tiago Domingos. Periodic and quasi-periodic behavior in resource-dependent age structured population models. *Bulletin of Mathematical Biology*, 63(2):207–230, 2001.

- [10] L. Glass and M.C. MacKey. *From Clocks to Chaos: The Rhythms of Life*. Princeton Paperbacks. Princeton University Press, 1988.
- [11] K. R. Sreenivasan and C. Meneveau. The fractal facets of turbulence. *Journal of Fluid Mechanics*, 173:357–386, Dec 1986.
- [12] F. T. Arecchi, R. Meucci, G. Puccioni, and J. Tredicce. Experimental evidence of subharmonic bifurcations, multistability, and turbulence in a  $q$ -switched gas laser. *Phys. Rev. Lett.*, 49:1217–1220, Oct 1982.
- [13] Reuben H. Simoyi, Alan Wolf, and Harry L. Swinney. One-dimensional dynamics in a multicomponent chemical reaction. *Phys. Rev. Lett.*, 49:245–248, Jul 1982.
- [14] Apostolos Argyris, Dimitris Syvridis, Laurent Larger, Valerio Annovazzi-Lodi, Pere Colet, Ingo Fischer, Jordi García-Ojalvo, Claudio R. Mirasso, Luis Pesquera, and K. Alan Shore. Chaos-based communications at high bit rates using commercial fibre-optic links. *Nature*, 438:343–346, Nov 2005.
- [15] Gregory D. VanWiggeren and Rajarshi Roy. Communication with chaotic lasers. *Science*, 279(5354):1198–1200, 1998.
- [16] T. L. Carroll. A nonlinear dynamics method for signal identification. *Chaos: An Interdisciplinary Journal of Nonlinear Science*, 17(2):023109, 2007.
- [17] Atsushi Uchida, Kazuya Amano, Masaki Inoue, Kunihiro Hirano, Sunao Naito, Hiroyuki Someya, Isao Oowada, Takayuki Kurashige, Masaru Shiki, Shigeru Yoshimori, Kazuyuki Yoshimura, and Peter Davis. Fast physical random bit generation with chaotic semiconductor lasers. *Nature Photon.*, 2:728–732, 2008.
- [18] I. Reidler, Y. Aviad, M. Rosenbluh, and I. Kanter. Ultrahigh-Speed Random Number Generation Based on a Chaotic Semiconductor Laser. *Phys. Rev. Lett.*, 103:024102, 2009.
- [19] Apostolos Argyris, Stavros Deligiannidis, Evangelos Pikasis, Adonis Bogris, and Dimitris Syvridis. Implementation of 140 Gb/s true random bit generator based on a chaotic photonic integrated circuit. *Opt. Express*, 18(18):18763–18768, 2010.
- [20] Ido Kanter, Yaara Aviad, Igor Reidler, Elad Cohen, and Michael Rosenbluh. An optical ultrafast random bit generator. *Nature Photon.*, 4:58–61, 2010.
- [21] Kunihiro Hirano, Taiki Yamazaki, Shinichiro Morikatsu, Haruka Okumura, Hiroki Aida, Atsushi Uchida, Shigeru Yoshimori, Kazuyuki Yoshimura, Takahisa Harayama, and Peter Davis. Fast random bit generation with bandwidth-enhanced chaos in semiconductor lasers. *Opt. Express*, 18(6):5512–5524, 2010.

- [22] T. Birch. *The history of The Royal Society of London for improving of natural knowledge, in which the most considerable of those papers communicated to the Society, which have hitherto not been published, are inserted in their proper order, as a supplement to the Philosophical Transactions*, volume 2. 1756.
- [23] Matthew Bennett, Michael F. Schatz, Heidi Rockwood, and Kurt Wiesenfeld. Huygens’s clocks. *Proceedings of the Royal Society of London. Series A: Mathematical, Physical and Engineering Sciences*, 458(2019):563–579, 2002.
- [24] Hirokazu Fujisaka and Tomoji Yamada. Stability theory of synchronized motion in coupled-oscillator systems. *Progress of Theoretical Physics*, 69(1):32–47, 1983.
- [25] Y. Tang, A. Mees, and L.O. Chua. Synchronization and chaos. *IEEE Trans. Circuits Syst.*, 30(9):620–626, 1983.
- [26] L. M. Pecora and T. L. Carroll. Synchronization in chaotic systems. *Phys. Rev. Lett.*, 64:821–824, 1990.
- [27] V.S. Afraimovich, N.N. Verichev, and M.I. Rabinovich. Stochastic synchronization of oscillation in dissipative systems. *Radiophysics and Quantum Electronics*, 29(9):795–803, 1986.
- [28] Henning U. Voss. Dynamic long-term anticipation of chaotic states. *Phys. Rev. Lett.*, 87:014102, Jun 2001.
- [29] W. Timothy Holman, J. Alvin Connelly, and Ahmad B. Dowlatabadi. An Integrated Analog/Digital Random Noise Source. *IEEE Trans. Circuits Syst. I*, 44(6):521–528, 1997.
- [30] P. Xu, Y.L. Wong, T.K. Horiuchi, and P.A. Abshire. Compact floating-gate true random number generator. *Electron. Lett.*, 42(23):1346–1347, 2006.
- [31] Thomas Jennewein, Ulrich Achleitner, Gregor Weihs, Harald Weinfurter, and Anton Zeilinger. A fast and compact quantum random number generator. *Rev. Sci. Instrum.*, 71(4):1675–1680, 2000.
- [32] J. F. Dynes, Z. L. Yuan, A. W. Sharpe, and A. J. Shields. A high speed, postprocessing free, quantum random number generator. *Appl. Phys. Lett.*, 93:031109, 2008.
- [33] Alan M. Ferrenberg, D. P. Landau, and Y. Joanna Wong. Monte Carlo simulations: Hidden errors from “good” random number generators. *Phys. Rev. Lett.*, 69(23):3382–3384, 1992.
- [34] Masatugu Isida and Hiroji Ikeda. Random number generator. *Ann. Inst. Stat. Math.*, 8(1):119–126, 1956.

- [35] J. Walker. HotBits: Genuine random numbers, generated by radioactive decay. Online: <http://www.fourmilab.ch/hotbits/>.
- [36] C.S. Petrie and J.A. Connelly. A noise-based IC random number generator for applications in cryptography. *IEEE Trans. Circuits Syst. I*, 47(5):615–621, 2000.
- [37] Benjamin Jun and Paul Kocher. The Intel Random Number Generator. Cryptography Research Inc., white paper prepared for Inter Corp., 1999.
- [38] Marco Bucci, Lucia Germani, Raimondo Luzzi, Alessandro Trifiletti, and Mario Varanuovo. A High-Speed Oscillator-Based Truly Random Number Source for Cryptographic Applications on a Smart Card IC. *IEEE Trans. Comput.*, 52:403–409, 2003.
- [39] G.M. Bernstein and M.A. Lieberman. Secure random number generation using chaotic circuits. *IEEE Trans. Circuits Syst.*, 37(9):1157–1164, 1990.
- [40] Toni Stojanovski and Ljupčo Kocarev. Chaos-Based Random Number Generators – Part I: Analysis. *IEEE Trans. Circuits Syst. I*, 48(3):281–288, 2001.
- [41] T. Stojanovski, J. Pihl, and Ljupčo Kocarev. Chaos-Based Random Number Generators – Part II: Practical Realization. *IEEE Trans. Circuits Syst. I*, 48(3):382–385, 2001.
- [42] M. Haahr. Random.org: True Random Number Service. Online: <http://www.random.org/>.
- [43] C. Gabriel, C. Wittmann, D. Sych, R. Dong, W. Mauerer, U. L. Andersen, C. Marquardt, and G. Leuchs. A generator for unique quantum random numbers based on vacuum states. *Nature Photon.*, 4:711–715, 2010.
- [44] L. C. Noll and S. Cooper. What is LavaRnd? Online: <http://www.lavarnd.org/>.
- [45] Bing Qi, Y.-M. Chi, H.-K. Lo, and L. Qian. High-speed quantum random number generation by measuring phase noise of a single-mode laser. *Opt. Lett.*, 35(3):312–314, 2010.
- [46] Hong Guo, Wenzhuo Tang, Yu Liu, and Wei Wei. Truly random number generation based on measurement of phase noise of a laser. *Phys. Rev. E*, 81(5):051137, 2010.
- [47] N. A. Olsson. Lightwave Systems With Optical Amplifiers. *J. Lightwave Technol.*, 7(7):1071–1082, 1989.
- [48] R. C. Steele, G. R. Walker, and N. G. Walker. Sensitivity of Optically Preamplified Receivers with Optical Filtering. *IEEE Photon. Technol. Lett.*, 3(6):545–547, 1991.

- [49] M. S. Leeson. Performance Analysis of Direct Detection Spectrally Sliced Receivers Using Fabry-Perot Filters. *J. Lightwave Technol.*, 18(1):13–25, 2000.
- [50] J. W. Goodman. *Statistical Optics*. Wiley, 1985. p. 246.
- [51] P. A. Humblet and M. Azizoglu. On the Bit Error Rate of Lightwave Systems with Optical Amplifiers. *J. Lightwave Technol.*, 9(11):1576–1582, 1991.
- [52] A. J. Keating and D. D. Sampson. Reduction of Excess Intensity Noise in Spectrum-Sliced Incoherent Light for WDM Applications. *J. Lightwave Technol.*, 15(1):53–61, 1997.
- [53] J.-S. Lee. Signal-to-Noise Ratio of Spectrum-Sliced Incoherent Light Sources Including Optical Modulation Effects. *J. Lightwave Technol.*, 14(10):2197–2201, 1996.
- [54] D. Knuth. *The Art of Computer Programming, Volume 2: Seminumerical Algorithms (3rd ed.)*. Addison-Wesley, 1996. pp. 64–65.
- [55] Andrew Rukhin, Juan Soto, James Nechvatal, Miles Smid, Elaine Barker, Stefan Leigh, Mark Levenson, Mark Vangel, David Banks, Alan Heckert, James Dray, and San Vo. *A Statistical Test Suite for Random and Pseudorandom Number Generators for Cryptographic Applications (NIST Special Publication 800-22, Revision 1a)*. National Institute of Standards and Technology, 2010.
- [56] G. Marsaglia. DIEHARD: A battery of tests of randomness. Online: <http://www.stat.fsu.edu/pub/diehard/>, 1996.
- [57] S. Pironio, A. Acín, S. Massar, A. Boyer de la Giroday, D. N. Matsukevich, P. Maunz, S. Olmschenk, D. Hayes, L. Luo, T. A. Manning, and C. Monroe. Random numbers certified by Bell’s theorem. *Nature*, 464:1021–1024, 2010.
- [58] R. H. Walden. Analog-to-digital converter survey and analysis. *IEEE J. Sel. Areas Commun.*, 17(4):539–550, 1999.
- [59] A. Neyer and Edgar Voges. Dynamics of electrooptic bistable devices with delayed feedback. *IEEE J. Quantum Electron.*, 18(12):2009–2015, 1982.
- [60] Y. Chembo Kouomou, Pere Colet, Laurent Larger, and Nicolas Gastaud. Chaotic breathers in delayed electro-optical systems. *Phys. Rev. Lett.*, 95:203903, Nov 2005.
- [61] Adam B. Cohen, Bhargava Ravoori, Thomas E. Murphy, and Rajarshi Roy. Using synchronization for prediction of high-dimensional chaotic dynamics. *Phys. Rev. Lett.*, 101:154102, Oct 2008.
- [62] Thomas E. Murphy, Adam B. Cohen, Bhargava Ravoori, Karl R. B. Schmitt, Anurag V. Setty, Francesco Sorrentino, Caitlin R. S. Williams, Edward Ott, and Rajarshi Roy. Complex dynamics and synchronization of delayed-feedback nonlinear oscillators. *Phil. Trans. R. Soc. A*, 368(1911):343–366, 2010.

- [63] Bhargava Ravoori, Adam B. Cohen, Anurag V. Setty, Francesco Sorrentino, Thomas E. Murphy, Edward Ott, and Rajarshi Roy. Adaptive synchronization of coupled chaotic oscillators. *Phys. Rev. E*, 80:056205, Nov 2009.
- [64] Francesco Sorrentino and Edward Ott. Adaptive synchronization of dynamics on evolving complex networks. *Phys. Rev. Lett.*, 100:114101, Mar 2008.
- [65] Francesco Sorrentino and Edward Ott. Using synchronism of chaos for adaptive learning of time-evolving network topology. *Phys. Rev. E*, 79:016201, Jan 2009.
- [66] Francesco Sorrentino and Edward Ott. Using synchronization of chaos to identify the dynamics of unknown systems. *Chaos: An Interdisciplinary Journal of Nonlinear Science*, 19(3):033108, 2009.
- [67] Adam B. Cohen, Bhargava Ravoori, Francesco Sorrentino, Thomas E. Murphy, Edward Ott, and Rajarshi Roy. Dynamic synchronization of a time-evolving optical network of chaotic oscillators. *Chaos: An Interdisciplinary Journal of Nonlinear Science*, 20(4):043142, 2010.
- [68] Bhargava Ravoori. *Synchronization of Chaotic Optoelectronic Oscillators: Adaptive Techniques and the Design of Optimal Networks*. PhD thesis, University of Maryland, August 2011.
- [69] Min-Young Kim, Christopher Sramek, Atsushi Uchida, and Rajarshi Roy. Synchronization of unidirectionally coupled Mackey-Glass analog circuits with frequency bandwidth limitations. *Phys. Rev. E*, 74:016211, Jul 2006.
- [70] Bhargava Ravoori, Adam B. Cohen, Jie Sun, Adilson E. Motter, Thomas E. Murphy, and Rajarshi Roy. Robustness of optimal synchronization in real networks. *Phys. Rev. Lett.*, 107:034102, Jul 2011.
- [71] Adam B. Cohen. *Synchronization and Prediction of Chaotic Dynamics on Networks of Optoelectronic Oscillators*. PhD thesis, University of Maryland, August 2011.
- [72] M. Newman. *Networks: An Introduction*. OUP Oxford, 2010.
- [73] Y. Chembo Kouomou, Pere Colet, Laurent Larger, and Nicolas Gastaud. Chaotic breathers in delayed electro-optical systems. *Phys. Rev. Lett.*, 95:203903, Nov 2005.
- [74] M. Peil, M Jacquot, Y. K. Chembo, L. Larger, and T. Erneux. Routes to chaos and multiple time scale dynamics in broadband bandpass nonlinear delay electro-optic oscillators. *Phys. Rev. E*, 79:026208, 2009.
- [75] Kristine E. Callan, Lucas Illing, Zheng Gao, Daniel J. Gauthier, and Eckehard Schöll. Broadband chaos generated by an optoelectronic oscillator. *Phys. Rev. Lett.*, 104:113901, Mar 2010.

- [76] D. P. Rosin, K. E. Callan, D. J. Gauthier, and E. Schöll. Pulse-train solutions and excitability in an optoelectronic oscillator. *Europhys. Lett.*, 96(3):34001, 2011.
- [77] Réka Albert and Albert-László Barabási. Statistical mechanics of complex networks. *Rev. Mod. Phys.*, 74:47–97, Jan 2002.
- [78] S. Boccaletti, V. Latora, Y. Moreno, M. Chavez, and D.-U. Hwang. Complex networks: Structure and dynamics. *Phys. Reports*, 424(4-5):175–308, 2006.
- [79] Arkady S. Pikovsky, Michael G. Rosenblum, and J. Kurths. *Synchronization, A Universal Concept in Nonlinear Sciences*. Cambridge University Press, Cambridge, 2001.
- [80] L. M. Pecora and T. L. Carroll. Master stability functions for synchronized coupled systems. *Phys. Rev. Lett.*, 80(10):2109–2112, March 1998.
- [81] J. M. Buldu, M. C. Torrent, and J. García-Ojalvo. Synchronization in semiconductor laser rings. *J. Lightwave Techn.*, 25(6):1549–1554, June 2007.
- [82] C. M. González, C. Masoller, M. C. Torrent, and J. García-Ojalvo. Synchronization via clustering in a small delay-coupled laser network. *Europhys. Lett.*, 79(6):64003, 2007.
- [83] Johannes Kestler, Wolfgang Kinzel, and Ido Kanter. Sublattice synchronization of chaotic networks with delayed couplings. *Phys. Rev. E*, 76:035202, Sep 2007.
- [84] Y. Aviad, I. Reidler, M. Zigzag, M. Rosenbluh, and I. Kanter. Synchronization in small networks of time-delay coupled chaotic diode lasers. *Opt. Express*, 20(4):4352–4359, Feb 2012.
- [85] Micha Nixon, Moti Friedman, Eitan Ronen, Asher A. Friesem, Nir Davidson, and Ido Kanter. Synchronized cluster formation in coupled laser networks. *Phys. Rev. Lett.*, 106:223901, Jun 2011.
- [86] A Amann, A Pokrovskiy, S Osborne, and S O’Brien. Complex networks based on discrete-mode lasers. *J. Phys. Conf. Series*, 138(1):012001, 2008.
- [87] Simone Pigolotti, Sandeep Krishna, and M. H. Jensen. Oscillation patterns in negative feedback loops. *Proc. Natl. Acad. Sci.*, 104(16):6533–6537, 2007.
- [88] M. H. Jensen, Sandeep Krishna, and Simone Pigolotti. Repressor lattice: Feedback, commensurability, and dynamical frustration. *Phys. Rev. Lett.*, 103:118101, September 2009.
- [89] Chol-Ung Choe, Thomas Dahms, Philipp Hövel, and Eckehard Schöll. Controlling synchrony by delay coupling in networks: From in-phase to splay and cluster states. *Phys. Rev. E*, 81:025205, Feb 2010.

- [90] I. Kanter, E. Kopelowitz, R. Vardi, M. Zigzag, W. Kinzel, M. Abeles, and D. Cohen. Nonlocal mechanism for cluster synchronization in neural circuits. *Europhys. Lett.*, 93(6):66001, 2011.
- [91] I. Kanter, M. Zigzag, A. Englert, F. Geissler, and W. Kinzel. Synchronization of unidirectional time delay chaotic networks and the greatest common divisor. *Europhys. Lett.*, 93(6):60003, 2011.
- [92] Johannes Kestler, Evi Kopelowitz, Ido Kanter, and Wolfgang Kinzel. Patterns of chaos synchronization. *Phys. Rev. E*, 77:046209, Apr 2008.
- [93] Thomas Dahms, Judith Lehnert, and Eckehard Schöll. Cluster and group synchronization in delay-coupled networks. *Phys. Rev. E*, 86:016202, Jul 2012.
- [94] Josep Mulet, Claudio Mirasso, Tilmann Heil, and Ingo Fischer. Synchronization scenario of two distant mutually coupled semiconductor lasers. *J. Opt. B*, 6(1):97, 2004.
- [95] Caitlin R. S. Williams, Thomas E. Murphy, Rajarshi Roy, Francesco Sorrentino, Thomas Dahms, and Eckehard Schöll. Experimental observations of group synchrony in a system of chaotic optoelectronic oscillators, supplemental material. *Phys. Rev. Lett.*, 110:064104, Feb 2013.
- [96] Ingo Fischer, R. Vicente, J. M. Buldú, M. Peil, Claudio R. Mirasso, M. C. Torrent, and J. García-Ojalvo. Zero-lag long-range synchronization via dynamical relaying. *Phys. Rev. Lett.*, 97:123902, 2006.
- [97] Awadhesh Prasad, Syamal Kumar Dana, Rajat Karnatak, Jurgen Kurths, Bernd Blasius, and Ramakrishna Ramaswamy. Universal occurrence of the phase-flip bifurcation in time-delay coupled systems. *Chaos: An Interdisciplinary Journal of Nonlinear Science*, 18(2):023111, 2008.
- [98] J.D. Murray. *Mathematical Biology: I. An Introduction*. Interdisciplinary Applied Mathematics. Springer, 2002.
- [99] Avis H. Cohen, Philip J. Holmes, and Richard H. Rand. The nature of the coupling between segmental oscillators of the lamprey spinal generator for locomotion: A mathematical model. *Journal of Mathematical Biology*, 13(3):345–369, 1982.
- [100] C. von Euler. On the central pattern generator for the basic breathing rhythmicity. *Journal of Applied Physiology*, 55(6):1647–1659, 1983.
- [101] Serhiy Yanchuk and Matthias Wolfrum. Destabilization patterns in chains of coupled oscillators. *Physical Review E*, 77(2):026212, 2008.
- [102] P. Perlikowski, S. Yanchuk, O. V. Popovych, and P. A. Tass. Periodic patterns in a ring of delay-coupled oscillators. *Physical Review E*, 82(3):036208, 2010.

- [103] Oleksandr V. Popovych, Serhiy Yanchuk, and Peter A. Tass. Delay-and coupling-induced firing patterns in oscillatory neural loops. *Physical review letters*, 107(22):228102, 2011.
- [104] Chol-Ung Choe, Thomas Dahms, Philipp Hövel, and Eckehard Schöll. Controlling synchrony by delay coupling in networks: From in-phase to splay and cluster states. *Phys. Rev. E*, 81:025205, Feb 2010.
- [105] M. A. Matías, J. Güémez, V. Pérez-Munuzuri, I. P. Marino, M. N. Lorenzo, and V. Pérez-Villar. Size instabilities in rings of chaotic synchronized systems. *EPL (Europhysics Letters)*, 37(6):379, 1997.
- [106] M. A. Matias, V. Pérez-Muñuzuri, M. N. Lorenzo, I. P. Marino, and V Pérez-Villar. Observation of a fast rotating wave in rings of coupled chaotic oscillators. *Physical review letters*, 78(2):219, 1997.
- [107] M. A. Matías and J. Güémez. Transient periodic rotating waves and fast propagation of synchronization in linear arrays of chaotic systems. *Physical review letters*, 81(19):4124, 1998.
- [108] X. L. Deng and H. B. Huang. Spatial periodic synchronization of chaos in coupled ring and linear arrays of chaotic systems. *Physical Review E*, 65(5):055202, 2002.
- [109] E. Sánchez and M. A. Matías. Experimental observation of a periodic rotating wave in rings of unidirectionally coupled analog Lorenz oscillators. *Physical Review E*, 57(5):6184–6186, 1998.
- [110] Oleksandr V. Popovych, Serhiy Yanchuk, and Peter A. Tass. Delay- and coupling-induced firing patterns in oscillatory neural loops. *Phys. Rev. Lett.*, 107:228102, Nov 2011.
- [111] Serhiy Yanchuk, Przemyslaw Perlikowski, Oleksandr V. Popovych, and Peter A. Tass. Variability of spatio-temporal patterns in non-homogeneous rings of spiking neurons. *Chaos: An Interdisciplinary Journal of Nonlinear Science*, 21(4):047511, 2011.
- [112] Xiaowen Li, Adam B. Cohen, Thomas E. Murphy, and Rajarshi Roy. Scalable parallel physical random number generator based on a superluminescent LED. *Opt. Lett.*, 36(6):1020–1022, Mar 2011.
- [113] Takuya Mikami, Kazutaka Kanno, Kota Aoyama, Atsushi Uchida, Tohru Ikeguchi, Takahisa Harayama, Satoshi Sunada, Ken-ichi Arai, Kazuyuki Yoshimura, and Peter Davis. Estimation of entropy rate in a fast physical random-bit generator using a chaotic semiconductor laser with intrinsic noise. *Phys. Rev. E*, 85:016211, Jan 2012.

- [114] Jianzhong Zhang, Yuncai Wang, Ming Liu, Lugang Xue, Pu Li, Anbang Wang, and Mingjiang Zhang. A robust random number generator based on differential comparison of chaotic laser signals. *Opt. Express*, 20(7):7496–7506, Mar 2012.
- [115] Pu Li, Yun-Cai Wang, An-Bang Wang, Ling-Zhen Yang, Ming-Jiang Zhang, and Jian-Zhong Zhang. Direct generation of all-optical random numbers from optical pulse amplitude chaos. *Opt. Express*, 20(4):4297–4308, Feb 2012.
- [116] Kazuyuki Yoshimura, Jun Muramatsu, Peter Davis, Takahisa Harayama, Haruka Okumura, Shinichiro Morikatsu, Hiroki Aida, and Atsushi Uchida. Secure key distribution using correlated randomness in lasers driven by common random light. *Phys. Rev. Lett.*, 108:070602, Feb 2012.
- [117] Takahisa Harayama, Satoshi Sunada, Kazuyuki Yoshimura, Peter Davis, Ken Tsuzuki, and Atsushi Uchida. Fast nondeterministic random-bit generation using on-chip chaos lasers. *Phys. Rev. A*, 83:031803, Mar 2011.
- [118] Satoshi Sunada, Takahisa Harayama, Kenichi Arai, Kazuyuki Yoshimura, Ken Tsuzuki, Atsushi Uchida, and Peter Davis. Random optical pulse generation with bistable semiconductor ring lasers. *Opt. Express*, 19(8):7439–7450, Apr 2011.